Laser-Based High Heat Flux Testing for Power Exhaust in Fusion Devices

Nick Schwartz

Somerville College

University of Oxford

A thesis submitted for the degree of

Master of Science by Research

Trinity 2020

Acknowledgements

I would like to thank my sponsors, the Marshall Aid Commemoration Commission, for their financial support during my time as a Marshall Scholar.

Throughout my experience at the Oxford Thermofluids Institute, I have received guidance and wisdom from many people. I would especially like to thank my supervisor, Professor Peter Ireland. He was a great guide through the process, consistently encouraging me. I am very grateful for his passion and incredible wit.

Additionally, I'd like to thank the technical members of staff who assisted in my project. Dave O'Dell was instrumental in the iterative design and machining process. Phil Bower was a great joy to work with and always made time to help with my electrical hardware problems.

Moreover, I'd like to thank the two people who helped me most with this project. Jack Nicholas has an incredible passion for fusion and clean energy, and I am certain that he will continue to be someone that many many engineers, myself included, aspire to be more like. Zach Jackson was always willing to put aside what he was working on and help me achieve things I did not think were possible.

To Cristie, my long-distance and long-time girlfriend, I am so proud of all that we have accomplished together over this past year. I am truly glad to be back 'across the pond' where I am closer to you.

And lastly, to my parents, Rafi and Jacque, this work was not what I thought it would be. COVID-19 meant that I couldn't accomplish what I had set out to do, but nothing could beat spending an entire summer with both of you. As always you've shown me love and encouragement through your actions and I am forever grateful.

Contents

Abstract

One of the critical challenges in realizing fusion energy is the survival and cooling of the Plasma Facing Components (PFCs) in the extreme environment (>1000 ℃ and constant neutron bombardment). In the DEMOnstration Power Plant (DEMO), the divertor must endure steady state loads of 10 $\frac{\mathrm{MW}}{\mathrm{m}^2}$ and transient thermal cycling up to 20 $\frac{\mathrm{MW}}{\mathrm{m}^2}$. Novel target designs are needed to cope with this thermal load.

An optics system was designed to replicate the thermal environment in DEMO. A new facility, coined the Oxford Laser Heating Facility (OLAHF), has been established for laser-based heating tests. A Compound Parabolic Concentrator (CPC) was designed to focus the power from four laser modules to greater than 5 $\frac{\mathrm{MW}}{\mathrm{m}^2}$ onto a target that absorbs 98.9% of the incident light. Numerical, thermomechanical studies on the steady-state performance confirmed that the deformation of the CPC does not exceed 0.4 mm and that the maximum temperature of the glass is less than 30 ℃.

A novel divertor target, termed the Spiral Plate Module (SPM), was designed to meet the fusion-relevant requirements. The geometry of the SPM was initially optimized by a one-dimensional model, the results of which showed a good correlation to Computational Fluid Dynamics (CFD) studies. The SPM achieved the lowest wall overheat (τ_s) and dimensionless mass flow rate (m^*) of any target design considered, and showed good hydraulic performance such that the power needed to pump the coolant is only 0.32% of the incident heat flux.

Lastly, a method was created to control the lasers and monitor the processes within OLAHF. Through a number of Labview panels, the operator can vary the laser power in time and record and store experimental data, and the program will send a warning

or shut down all systems (depending on severity) if there is a possibility of harm to the hardware or users.

List of Figures

List of Tables

Nomenclature

Acronyms

E	Emitter
O	Optic
R	Receiver/Target
CAD	Computer Aided Design
CFD	Computational Fluid Dynamics
CHF	Critical Heat Flux
CPC	Compound Parabolic Concentrator
CPS	Capillary Porous System
DAQ	Data Acquisition System
DBTT	Ductile-to-Brittle Transition Temperature
DEMO	DEMOnstration Power Plant
dpa	Displacements per atom
HHF	High Heat Flux
HPJC	High Pressure Jet Cascade
ICF	Inertial Confinement Fusion
IVT	Inner Vertical Target
JET	Joint European Torus
LM	Liquid Metal
MB	Monoblock
MCF	Magnetic Confinement Fusion
MHD	Magnetohydrodynamic

MWCNT Multi-Walled Carbon Nanotubes

NIST National Institute of Standards and Technology

OLAHF Oxford Laser Heating Facility

OTI Oxford Thermofluids Institute

OVT Outer Vertical Target

PFC Plasma Facing Component

SDC-IC Structural Design Criteria for In-vessel Components

SOL Scrape-Off Layer

SPM Spiral Plate Module

VCSEL Vertical-Cavity Surface-Emitting Laser

WPDIV Work Package Divertor

Symbols

A	Characteristic area scale [m^2]
D	Diameter [m]
H	Spectral power density [W s sr^{-1} m^{-2}]
I	Irradiance [W m^{-2}]
L	Characteristic length scale [m]
P	Pressure [Pa]
R	Thermal resistance [K W^{-1}]
R_c	Radius of curvature [m]
R_p	Reflection coefficient for p-polarized light
R_s	Reflection coefficient for s-polarized light
R_{ps}	Reflection coefficient, with combined effects of p- and s-polarization
T	Temperature [°C]
T_0	Ambient Temperature [°C]

T_{ps}	Transmission coefficient, with combined effects of p- and s-polarization
U	Étendue [m^2 sr]
Δh	Standard deviation of surface roughness [m]
$\dot{P}$	Pumping power [W]
$\dot{Q}$	Power [W]
$\dot{m}$	Mass flow rate [kg s^{-1}]
$\dot{q}$	Heat flux [W m^{-2}]
a	Longer half width of aperture [m]
a_{sp}	Spiral gain factor [m]
b	Shorter half width of aperture [m]
c_p	Specific heat capacity at constant pressure [J kg^{-1} K^{-1}]
d_{RO}	Distance from Receiver to Optic [m]
h	Convective heat transfer coefficient [W m^{-2} K^{-1}]
h_{cpc}	Height of CPC [m]
j	Radiative power density [W m^{-2}]
k	Thermal conductivity [W m^{-1} K^{-1}]
l	Length along path [m]
r	Thermal resistance per unit area [K W^{-1} m^{-2}]
r_{sp}	Radius of spiral [m]
s	Side length of hexagonal target [m]
t	Thickness [m]
v	Velocity [m s^{-1}]
w_e	Width of emission [m]
x	Dependent variable in parametric equations [m]
y	Dependent variable in parametric equations [m]

Subscripts

acc	Acceptance
avg	Average

b	Bulk
c	Curved
ce	Coolant exit
ci	Coolant inlet
cpc	Compound Parabolic Concentrator
div	Divergence
e	Emission
$fric$	Friction
i	Incidence
id	Ideal
in	In
out	Out
ps	Parallel and perpendicular polarization
r	Along the r-direction
ref	Reference
s	Solid/Straight
sp	Spiral
std	Standard deviation
t	Target
w	Wall
z	Along the z-direction

Greek

Ω	Solid angle [sr]
α	Absorption coefficient
ϵ	Emissivity
λ	Radiation wavelength [m]
μ	Dynamic viscosity [Pa s]
ρ	Density [kg m^{-3}]

θ	Angle from the normal [rad]

Dimensionless Numbers

C	Concentration ratio, $\frac{A_{in}}{A_{out}}$
De	Dean number, $Re\sqrt{\frac{D_h}{R_c}}$
Pr	Prandtl number, $\frac{c_p \mu_f}{k_f}$
Q	Fusion energy gain factor, $\frac{\dot{Q}_{in}}{\dot{Q}_{out}}$
Re	Reynolds number, $\frac{\rho_f v D_{ref}}{\mu_f}$
Re_c	Critical Reynolds number
η_P	Pumping ratio, $\frac{\dot{P}}{\dot{Q}}$
η_τ	Transmission efficiency, $\frac{\dot{Q}_{in}}{\dot{Q}_{out}}$
τ_s	Wall overheat, $\frac{\dot{m} c_p}{\dot{m}_{id} c_{id}}$
f	Darcy-Weisbach friction factor, $\frac{2D_h}{\rho_f v_b^2 L} \Delta P_{fric}$
k	Imaginary part of refractive index, extinction coefficient
m^*	Non-dimensional mass flow rate, $\frac{\dot{m} c_p}{k_s \sqrt{A}}$
n	Real part of refractive index

Chapter 1

Introduction and Motivation

1.1 Growing Energy Demands

The global energy crisis is one of humanity's most formidable problems today. In fact, 'ample, accessible, and sustainable' energy is listed as one of the Grand Challenges of this century [1]. Humans have been using more and more energy, which closely aligns with increases in industrialization, globalization (Fig. 1.1), and the increasing amount of CO_2 in the atmosphere (Fig. 1.2). Moreover, there are still many places in the world where reliable, clean energy is not accessible; 50% of the world's population consumes less than 1 kW/person, the minimum required to attain an 'adequate' quality of life [2].

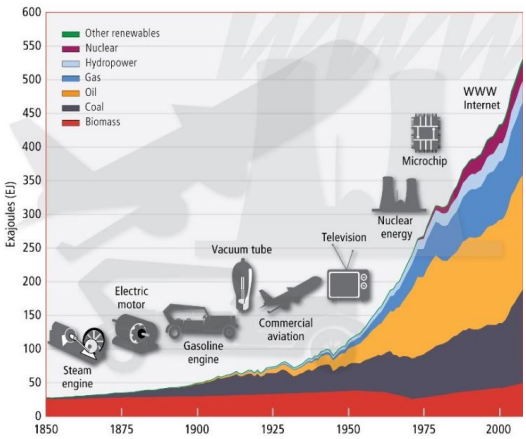

Figure 1.1. Evolution of world energy usage over time, subdivided into sources [3]. The global energy crisis is growing increasingly quickly, and most of the sources of fuel to meet the demand are not clean.

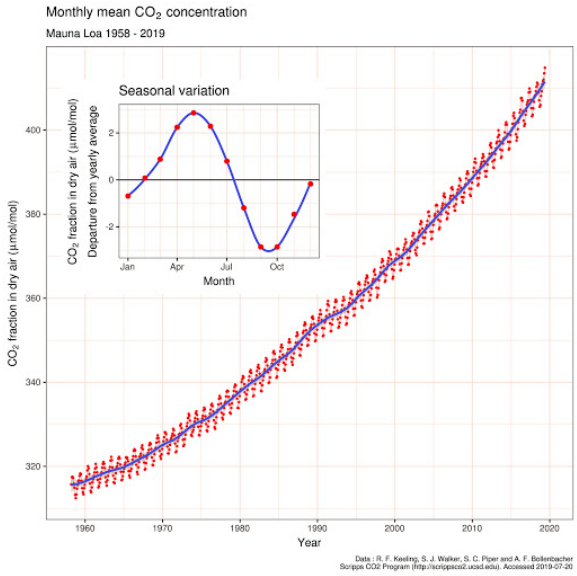

Figure 1.2. The accumulation of CO_2 in the atmosphere over time, known as the Keeling Curve [4]. This measurement is another metric of the harm that is brought about by emissions from global energy production.

The energy problem is three-fold.

1. Energy demands will continue to increase. Fossil fuels and a relatively small assortment of renewable sources (only 15%) have met the global needs thus far, but the real challenge is supplying enough energy for the future [5]. It is predicted that the energy demands may increase by as much as three times in the next 50 years [5].

2. If energy production continues in the same manner, without a halt to processes that release greenhouse gases, the end of the century may witness climate change "equal in magnitude, but opposite in sign" to the most recent Ice Age [5]. It is therefore of utmost importance that the increasing demands are met by sustainable, emission-free sources.

3. Energy use is directly connected to the quality of life [2, 6] and accessibility is a huge concern for developing countries, many of which have to import their energy sources. Renewable sources – like solar and wind –are not consistently

available, and others – like geothermal and tidal – are not available in many regions. The energy supply of the future must be accessible and cost-effective in any part of the world, at any time.

The efficiency and cost-effectiveness of renewable sources are growing, but it will be difficult to completely offset fossil fuels without the advent of revolutionary technology. Fusion energy can fill that gap.

Fusion is the phenomenon by which two positively charged ions come together to form a heavier product and energy. This nuclear process is the opposite of fission, whereby a heavy atom is split into two lighter ones.

1.2 Fusion Fundamentals

Fusion energy can provide abundant amounts of clean energy to the global population. In the reference frame of atoms, fusion is predicated on the fusing of two nuclei, releasing energy. In the reference frame of humanity, fusion energy is predicated on decades of research, engendering limitless, clean, and safe energy. The fuel for fusion energy can be found in seawater, which can provide for the world's energy needs for $\sim$6 million years [7]. Additionally, there are no emissions from the fusion process, meaning that the process does not exacerbate global warming, and the small amount of radioactive waste that is produced is not long-lived – it can be recycled or reused in 100 years [8]. Finally, there is a low risk of proliferation and no risk of meltdown. There has been success in building fusion reactors that demonstrate the scientific principles of fusion, but a net-positive energy output has yet to be achieved.

Fusion is only achieved through a state of matter known as plasma. Plasma is an ionized gas, where the electrons have been stripped from the atoms, and a quasi-neutral medium of positive and negative particles demonstrate collective behavior. Known as the 'Fourth State of Matter,' plasma makes up almost all observable matter in the universe. The kinds of plasmas that exist throughout the universe vary greatly

in terms of temperatures and densities (Fig. 1.3).

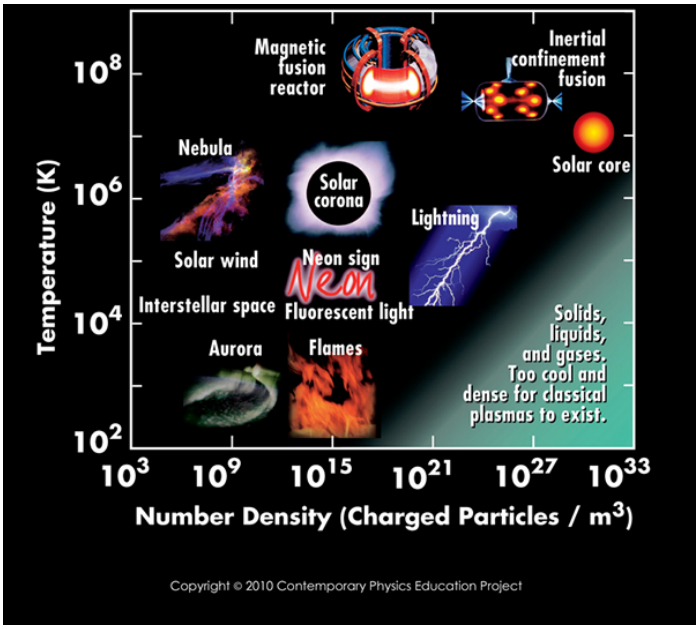

Figure 1.3. Various types of plasmas exist in the universe. Plasmas typically must be above certain temperatures and below certain densities to exist [9]. Some plasmas, like those in magnetic fusion and inertial confinement fusion, are being investigated as sources of terrestrial power.

Because the positively charged ions in a plasma repel each other, there must be some method of containment. Stars use their massive gravitational field to confine the process within their core, leading to very high densities. Attempts to achieve terrestrial fusion typically follow one of two paths: Magnetic Confinement Fusion (MCF) or Inertial Confinement Fusion (ICF). To make up for the lack of a huge gravitational field like in solar cores, magnetic confinement concepts apply magnetic fields around the plasma that prevent instabilities from growing, thus sustaining the plasma. Inertial confinement occurs at extremely small time scales and extremely high pressures, so that a fuel pellet is heated and the ions fuse before they have time to repel each other. Both types occur at higher temperatures because it is difficult to achieve the high density of a solar core.

All concepts for fusion devices hold this plasma inside a vacuum vessel. Typically, terrestrial plasmas exists at very high temperatures; plasma radiation and energized

particles that bombard the vessel surface heat it up. Heat extraction is important for two reasons: (1) it serves to protect components external to the vacuum vessel and (2) it can be used to power steam generators to create electricity. The inability to capture the energy from fusion and efficiently and safely convert it into electricity is still a problem that abates the success of fusion power plants.

This report focuses on one area of power extraction in fusion devices. A laser-based heating rig will be used to investigate various cooling (or rather, heat-extracting) frameworks for use in fusion reactors. The experimental setup consists of two major subsections.

- The laser(s), concentrator(s), and framework to ensure repeatability
- The element that is being cooled and all associated hardware

1.2.1 Tokamak Technology

Fusion energy is nature's preferred energy source. All stars, including our sun, are powered by fusion, where protons are heated to ∼15 million °C [10] in the core, producing atoms of higher atomic numbers and releasing energy. Fusion devices create a 'star on earth' inside a machine that can capture its energy [11, 12]. Although the cooling mechanisms for MCF and ICF are similar, this report focuses on heat exhaustion for MCF devices.

One type of MCF device is a tokamak, first conceptualized in the 1950s by two Soviet scientists, Igor Tamm and Andrei Sakharov. Its name is derived from the Russian phrase for a '**to**roidal **ch**amber with **ma**gnetic **c**oils,' and it is the most prolific device for fusion energy and research. There are many magnetic coils that work together to contain and shape the plasma in a tokamak (Fig. 1.4). The central transformer induces a plasma current, which creates a poloidal magnetic field. The toroidal field coils combine with this field to create a helical field that contains the plasma. Lastly, the poloidal field coils give the plasma its final shape.

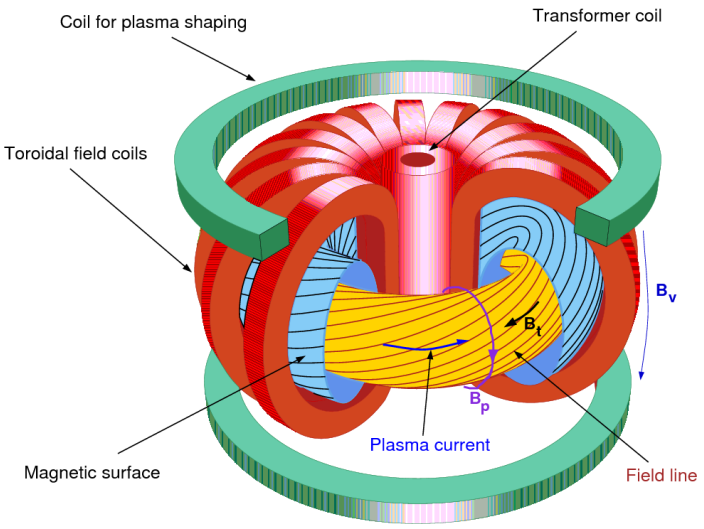

Figure 1.4. The toroidal field coils, the poloidal field produced by the plasma's current, and the central transformer superimpose to create a helical field that contains the plasma, while the poloidal field coils actually shape the plasma [13].

Most tokamaks utilize the deuterium-tritium (D-T) fuel cycle (Fig. 1.5). The deuterium supply is virtually inexhaustible and can be distilled from seawater, but tritium is rarely present in nature. Rather, it is 'bred' as a by-product of neutrons with lithium. In tokamaks, this reaction occurs at a plasma temperature of roughly 150 million °C. The energetic neutrons that are produced in the D-T fuel cycle can damage and activate materials. Other fuel cycles are being investigated for fusion that are aneutronic processes, but these require much higher temperatures (∼1 billion °C) which are often difficult to obtain, so this report focuses on D-T fusion.

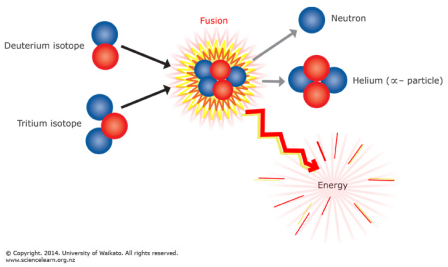

Figure 1.5. The process of deuterium-tritium (D-T) fusion, which produces a neutron, alpha-particle, and energy [14]. D-T fusion is the most widely investigated fuel cycle currently.

Tokamak operation begins with a startup phase. Typically, deuterium gas is injected into the device, and the central transformer supplies a current. Simultaneously, the gas is heated by some method (radiation or radiofrequency waves, for example), which ionizes the gas [15]. The magnetic coils then serve to contain and shape the newly formed plasma. Heat is exhausted through several systems described in Section 1.2.2.

The largest tokamak in the world is under construction in southern France under the name ITER. ITER is essentially a proof-of-concept study to show that fusion energy could be produced for the grid [16]. ITER's successor, the DEMOnstration Power Plant (DEMO), will showcase fusion's ability to provide industrial-scale electricity. DEMO (Fig. 1.6) aims to produce up to 500 MW net power [17].

Because 80% of the energy of the products of a D-T reaction is contained in energetic neutrons and not charged particles, the most efficient way of extracting energy is through heat exhaust. Therefore an efficient and safe heat exhaustion framework is necessary to bring the 500 MW functional requirement to fruition. The key to power exhaust is in the plasma facing components.

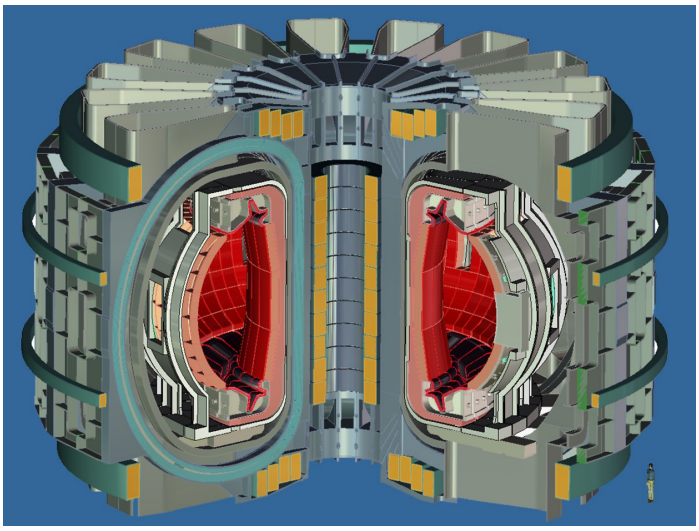

Figure 1.6. Conceptual cross-sectional view of the DEMOnstration power plant [16]. DEMO aims to bring nuclear fusion energy to the grid.

1.2.2 Plasma Facing Components

The main components of tokamaks are displayed in Fig. 1.7. The vacuum vessel houses the plasma in a steel, toroidal container. To protect the vacuum vessel, several actively cooled components are placed between its walls and the plasma. For the context of this report, only Plasma Facing Components (PFCs) are relevant due to the High Heat Flux (HHF) they must endure. The two assemblies which directly interact with the plasma are the divertor and blanket.

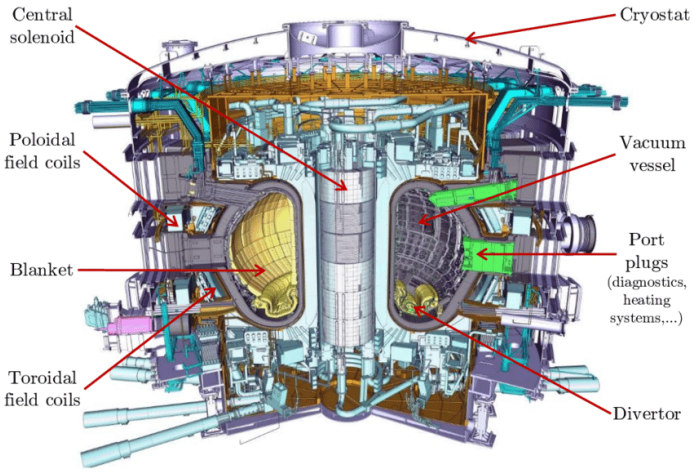

Figure 1.7. Schematic of ITER, labeled with the various subsystems [18]. The two assemblies of note with regards to this report are the divertor and the blanket. These are the plasma facing components that extract heat from the plasma.

The divertor is placed at the bottom of the vacuum vessel, where it can absorb energy from the Scrape-Off Layer (SOL) (Fig. 1.8). The SOL contains charged particles that have diffused across the last closed flux surface, i.e. the separatrix. Energy from these charged particles in the SOL and neutrons (which are not controlled by the magnetic field lines) is converted to heat when they collide with the divertor. The divertor dissipates up to 20 $\frac{\mathrm{MW}}{\mathrm{m}^2}$ for slow transient events and 10 $\frac{\mathrm{MW}}{\mathrm{m}^2}$ during steady-state operation [19].

The PFCs in the divertor are threefold – the Inner Vertical Target (IVT), Outer Vertical Target (OVT), and the Dome (Fig. 1.9). The shape of the ITER divertor

components is guided by the behavior of the plasma under steady-state conditions and off-normal events to distribute heat over the largest area possible. This minimizes the peak heat flux.

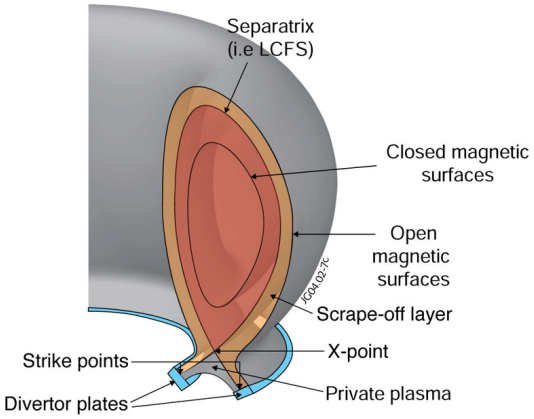

Figure 1.8. Cross-sectional schematic of plasma core in divertor-based tokomaks, including the SOL and separatrix [20]. The SOL and energetic neutrons strike the divertor, depositing high heat loads of up to 20 $\frac{\text{MW}}{\text{m}^2}$ for slow transient events and 10 $\frac{\text{MW}}{\text{m}^2}$ during steady-state operation.

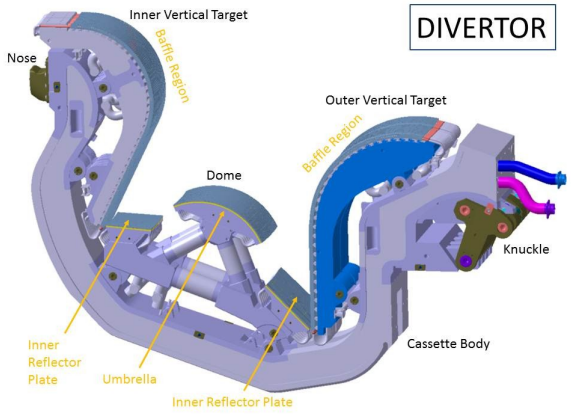

Figure 1.9. One of the ITER divertor casettes. The IVT and OVT directly intercept the SOL, shielding other components from the radiative, convective, and conductive heat load. The dome is below the X-point and does not see as high heat flux, but pumps out neutral byproducts, like helium. [21, 22]

The majority of the vacuum vessel is protected by the blanket, which is also actively cooled. The HHF on the blanket comes from radiative heat and neutron flux. ITER's blanket is designed to withstand heat fluxes up to 5 $\frac{\text{MW}}{\text{m}^2}$ [23] from radiative heat and

neutron bombardment. Because the blanket module handles lower heat fluxes than the divertor, this study focuses on problems associated with divertor PFCs. However, the framework used for testing can be applied to blanket components as well.

The design of the divertor for DEMO has been underway since 2014, with a special focus on the plasma facing divertor target. This project aims to further the testing capabilities for the target and to test novel target designs.

1.3 Problem Statement

1.3.1 Experimental Setup

Given the critical importance of the PFCs in DEMO, it is necessary to experimentally test a divertor cooling scheme that may eventually be used in the device. The Oxford Thermofluids Institute (OTI) has established the Oxford Laser Heating Facility (OLAHF) (Fig. 1.10). This facility is capable of experiments using simultaneous thermal and mechanical loads for extended or transient periods. The experimental setup can be used to test HHF components in a fusion reactor like DEMO.

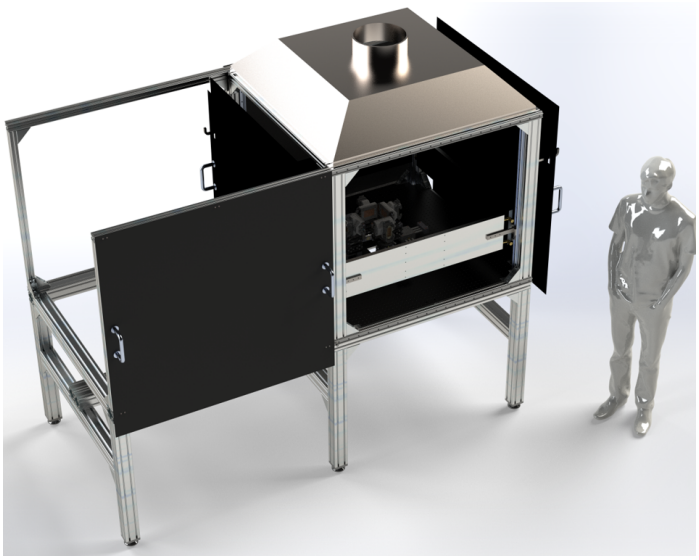

Figure 1.10. Computer Aided Design render of OLAHF experimental rig, including size comparison to human. The rig contains a number of laser modules that can be mounted to an optical table for high heat flux testing.

The frame of the test rig is constructed from Item aluminum profile and includes an optical breadboard for mounting experiments, doors for preventing laser light escaping into the room, and gas extraction if an inert gas environment is used.

The facility is equipped with four TRUMPF 2.4 kW Vertical-Cavity Surface-Emitting Laser (VCSEL) modules (Fig. 1.11) at a wavelength of 980 ± 20 nm, which have a typical irradiance of 1.15 $\frac{\mathrm{MW}}{\mathrm{m}^2}$ at the emission aperture. These Class 4 lasers are used in a variety of industry applications, including carbon fiber, solar cell, and furniture manufacturing. Here, they are useful because of their spatial and temporal resolution, and relatively high irradiance over a large area [24].

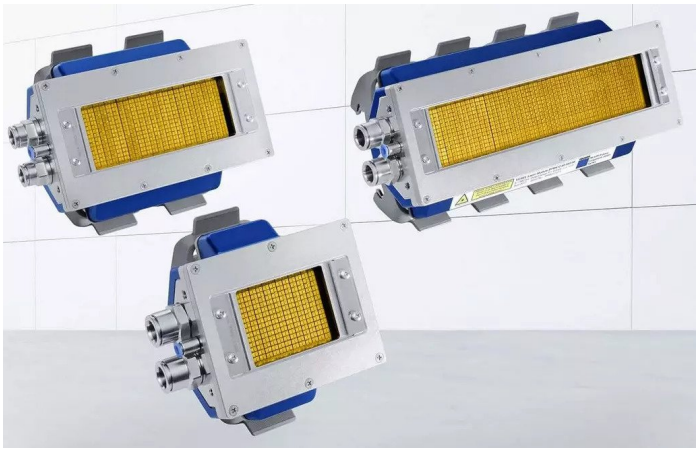

Figure 1.11. VCSEL infrared heating systems from TRUMPF, which consist of a 2.4 kW, 4.8 kW, and 9.6 kW unit from smallest to largest [25].

However, the irradiance of the laser modules alone is not enough to provide the required heat flux for testing DEMO divertor designs. Therefore, an optical concentrator must be designed such that the total laser power is delivered over a smaller area, thus increasing irradiance. This concentrator must meet the following functional requirements:

- It must fit inside the OLAHF test rig. For ease of mounting and accessibility, the lasers are pointed in the plane of the testbed, as opposed to the vertical direction. Therefore, the axial direction of the concentrator must also be

in the horizontal direction. The entire test setup must be able to fit in the 1.2×1.2×0.99 m volume of the rig.

- The target must receive >5 $\frac{\text{MW}}{\text{m}^2}$ at maximum laser power. This irradiance is on the same order of magnitude as the heat flux experienced by PFCs in the divertor.

- The target must have a frontal area of at least 10 cm^2. An area any smaller than that would be difficult to cool using off-the-shelf components. Furthermore, one modular plasma-facing unit in the current ITER-like design (to be discussed in Chapter 2) has a footprint of 62.5 mm × 23 mm, totaling ∼14 cm^2 in area [26]. It was thus decided that an area of 10 cm^2 would be sufficient to approximate the size of a modular unit in a future DEMO divertor.

- It must not fail under steady-state, maximum power operating conditions. The most critical failure mechanism is permanent thermal deformation. There are two sources of thermal energy: absorbed laser power due to a non-zero absorption coefficient and radiative heat from the target.

- It must produce as even a heat profile as possible such that the heat flux approximates the flux in DEMO

In summary, various cooling geometries and techniques for use in a DEMO divertor will be tested in a laser heating facility. Four 2.4 kW VCSEL modules will provide the heat source, focused by an optical concentrator, onto an actively-cooled target.

1.3.2 Facility Control and Monitoring

Class 4 laser safety regulations mandate that the user must not be in the room during laser operation. To enable remote operation and monitoring, a program must be designed such that the user can interface with the lasers and other sensors in the facility. This program must satisfy the following functional requirements:

- It must provide real-time monitoring of process parameters, such as tempera-

tures, flow rates, or humidities.

- If any of these aforementioned process parameters exceed a warning value, the user is be notified.
- If any of these aforementioned process parameters exceed a critical value, the user is be notified and the lasers are powered off.
- The user must be able to provide custom laser power profiles for periodic testing.
- The program records historical data for several parameters.
- The program considers possible user errors and has protocols to prevent such faults leading to system failures.

Chapter 2

Literature Review

2.1 Divertor Physics

Ernest Rutherford first produced fusion in the lab in 1934. He was able to fuse two deuterium atoms into helium and observed an "enormous effect" [27]. This experimental research went hand in hand with the initial theoretical work on reaction rates and proton-proton fusion that powers the sun. In 1950, two Soviet scientists – Andrei Sakharov and Igor Tamm – came up with the first 'magnetic bottle,' calling it a tokamak.

Work on the Joint European Torus (JET) was completed in 1983, which is currently the largest operational tokamak in the world, and it can produce 16 MW of power for a 24 MW input [28]. Although breakeven was not achieved with JET, ITER was proposed to be the first device to achieve this milestone of power in to power out ratio, Q, of greater than 1 with aims to achieve $Q = 10$. However, ITER is simply a feasibility study for fusion technology, and DEMO is the next step to bring fusion to the commercial sector [16].

The ITER divertor is the largest and most complex divertor designed to date, with decades of research optimizing the SOL configuration, divertor shape, and thermo-hydraulics. Yet, there still is ongoing research to develop better divertor technology. In fact, thermal load tests on current ITER PFCs demonstrate a process called re-

crystallization, which leads to macro-cracks due to decreased material strength and hardness [29]. This had lead researchers to believe that the steady-state operating conditions of the divertor must withstand up to 50% more heat flux than the previously mentioned 10 $\frac{\mathrm{MW}}{\mathrm{m}^2}$, to avoid this failure mode. Therefore, a divertor concept that will not fail under fatigue or high thermal stresses and outperforms the current ITER-like design is imperative for DEMO.

As described in Section 1.2, the divertor is of critical importance in tokamaks because it removes particles from the SOL and must absorb a massive convective, conductive, and radiative heat flux. Furthermore, the divertor must not eject fusion quenching impurities into the plasma. The divertor also acts as a neutron shield for the surrounding components like the vacuum vessel and superconducting magnets [30].

The IVT, OVT, and dome comprise one divertor casette, but the vertical targets receive a higher thermal load; therefore, the cooling geometries for the vertical targets and dome differ (Fig. 2.1). Because the IVT and OVT receive higher heat flux, their design is more critical. ITER's vertical targets will utilize a fully tungsten (W) Monoblock (MB) design with swirl tape (Fig. 2.2).

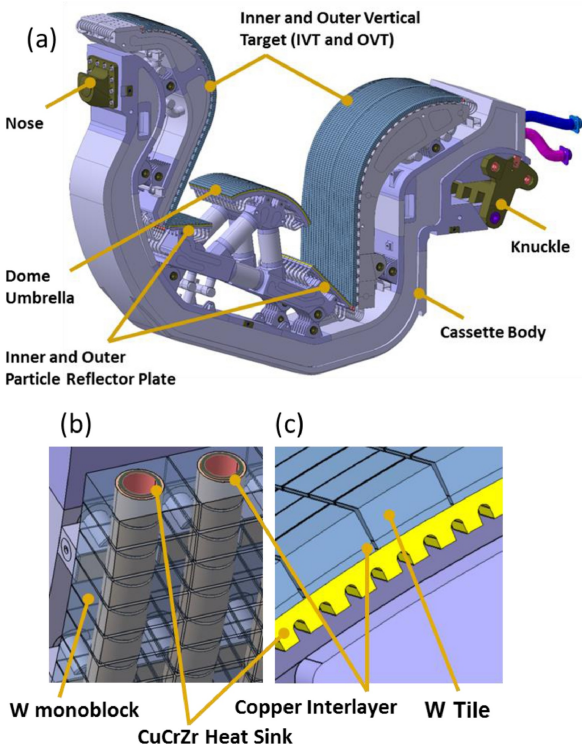

Figure 2.1. An ITER divertor casette (a) which incorporates three main PFCs. The IVT and OVT use a tungsten MB bonded to a CuCrZr tube (b) which offers better thermohydraulic performance than hypervapotrons in the dome (c) [30]. Both types of techniques are characterised in Section 2.2

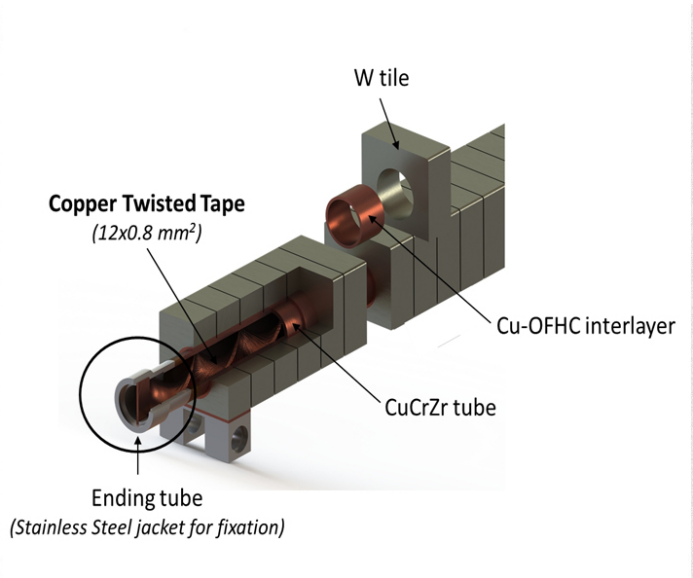

Figure 2.2. Schematic of tungsten MB with swirl tape [31]. The swirl tape increases mixing, leading to higher heat transfer coefficients without a large sacrifice in pressure drop.

Displacements per atom (dpa) is a quantification of how the neutron fluence damages the PFC material. Neutrons directly displace W atoms and lead to transmutations that produce more impurities in the material. The lifetime of the DEMO divertor is limited to two full-power years, during which it will receive an expected cumulative 13 dpa [32]. This damage decreases both the mechanical and thermal performance of materials.

The flux is not evenly distributed on the vertical targets and is highest at the strike points, where the flux from the SOL first hits the target in a band that could be as narrow as a few mm. Therefore, although the average heat flux on the divertor is below 5 $\frac{\mathrm{MW}}{\mathrm{m}^2}$ for most of the vertical targets and dome, it can be as high as 17-21 $\frac{\mathrm{MW}}{\mathrm{m}^2}$ at the strike point [32].

The Eurofusion Consortium, a body that supports and funds fusion research through the European Commission's Euratom, has defined a specific Research and Development track for the DEMO divertor. The Work Package Divertor (WPDIV) has two main focuses: 'cassette design and integration' and 'target development.' Fig. 2.3 shows a workflow chart for the separation of R&D, and this thesis falls into the 'target' subproject. The target is designed with two aims: (1) Critical Heat Flux (CHF) which leads to 'bulk coolant boiling or a dry-out should be avoided' by a factor of safety of 1.4 under the maximum heat load, which is assumed to be 20 $\frac{\mathrm{MW}}{\mathrm{m}^2}$; this means that the critical heat flux must be 1.4 times greater than the max flux, i.e. 28 $\frac{\mathrm{MW}}{\mathrm{m}^2}$. And (2) the PFC must retain 'sufficient toughness and strength even at the maximum irradiation dose' of 13 dpa [32]. These two goals oppose each other in some sense: the fluid heat flux must be far enough away from the CHF, which implies lower local channel surface temperatures. These lowered temperatures give rise to a higher thermal gradient in the target, inducing thermal strains that could lead to permanent deformation of the irradiated materials.

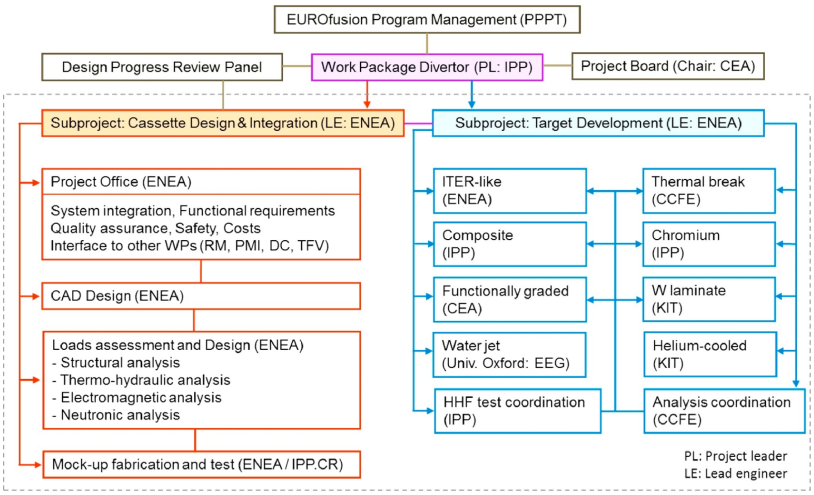

Figure 2.3. Schematic project breakdown structure of the EUROfusion work package 'Divertor' [32]. The project is broken down into two section, target development and casette design/integration. This report focuses on the target development portion of WPDIV.

2.2 Divertor Cooling

The cooling design used in the divertor will be chosen by the following criteria [33]:

- Meets operational safety requirements;
- Removes heat flux (10 $\frac{\text{MW}}{\text{m}^2}$ for steady-state operation and 20 $\frac{\text{MW}}{\text{m}^2}$ for slow transient events);
- Meets the pumping efficiency criteria that the pumping power should be less than 10% of the incident power [34];
- Is compatible with the material used in the coolant chamber walls;
- Whether or not tritium is able to be extracted from the coolant, and how efficiently this can be done;
- Thermodynamic capabilities to produce high energy conversion efficiency;
- Cost of produced electricity;
- Amount of nuclear waste per unit of energy;

A description of the baseline ITER-like target is necessary for comparison with other techniques. This reference design is a water-cooled, fully W MB design with swirl tape is one of the target concepts in WPDIV (Fig. 2.2). Crescenzi et al. performed a design optimization considering recrystallization, thermal strain, and heat exhaustion, but without swirl tape [19]. The MB design consists of a tungsten block, soft copper interlayer, and CuCrZr tube, diffusion bonded together through a process known as hot radial pressing. The main change from the original ITER mockups was a thinning of the monoblocks to avoid residual strain fatigue that led to macrocracks. Experimental results at a heat flux of 20 $\frac{\mathrm{MW}}{\mathrm{m}^2}$ did not produce defects, but further cyclical testing is needed to validate fatigue behavior.

The body of innovative work on thermal exhaust concepts for divertors is diverse in many ways. Helium, water, and Liquid Metal (LM) coolants have all been tested in a variety of configurations and geometries. Indeed, a medley of enhancement methods for increasing the heat transfer coefficient, h, have been tested, such as hypervapotrons, swirl tapes, porous flow, microfins, jet impingement, and Magneto-hydrodynamic (MHD) effects to name a few.

The following sections describe some of the current technologies and coolants under investigation. Each type of coolant has advantages and disadvantages, as outlined by Table 2.1.

Table 2.1. Outline of the various advantages and disadvantages associated with each type of coolant [35].

Coolant	Advantages	Disadvantages
Helium	No CHF, very safe Compatible with breeder blanket High operating T→high efficiency	Low heat capacity High operating pressures
Water	High h with two-phase flow High specific heat Relatively small pumping power Cheap	Possibility of CHF Lower thermal efficiency Unsuited for breeder blanket
Liquid Metal	High thermal conductivity High specific heat Low Z→less plasma impurities Compatible with breeder blanket	Electrically insulated coating MHD effects may decrease h Possibility of CHF

2.2.1 Helium-Cooled

A He-cooled divertor is of great interest because it is not susceptible to dry-out incidents. However, because of the relatively low thermal capacity and conductivity, it is necessary to use heat transfer enhancement methods. Rosenfield et al. investigated the use of porous channels to massively increase the surface area through which heat transfer occurs [36] (Fig. 2.4). They were able to achieve an h of 15,000-18,000 $\frac{\mathrm{W}}{\mathrm{m^2K}}$ with a He pressure of 2.0 MPa. Wong et al., performed similar experiments with porous He flow, but instead proposed the use of circumferential/annular channels [37] (Fig. 2.5). A circumferential flow path is significantly shorter than axial flow, meaning that the temperature gradient and local h along that path is flatter. Several others have performed studies on porous channel flow using He as a coolant [38–40]. Although it has been possible to remove up to 30 $\frac{\mathrm{MW}}{\mathrm{m^2}}$ with some of these technologies, the pressure drop is large and requires higher pumping pressures, meaning more expensive pumps.

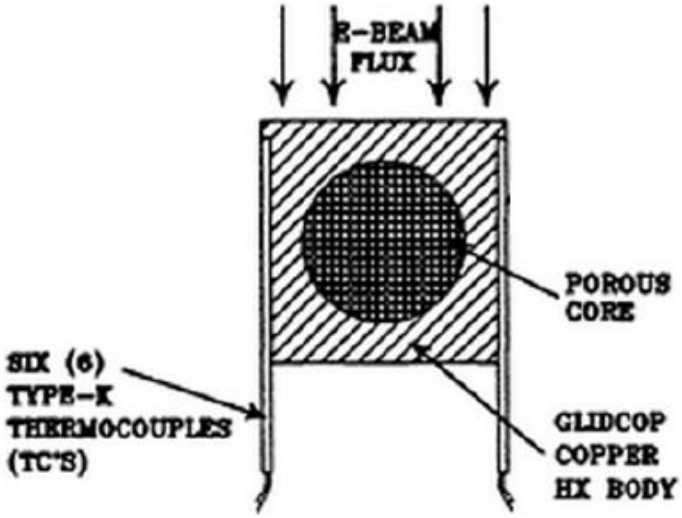

Figure 2.4. Porous cooling channel, which enhances heat transfer by increasing the solid surface area and turbulence [36]. This type of channel also has associated issues such as corrosion and large pressure drops.

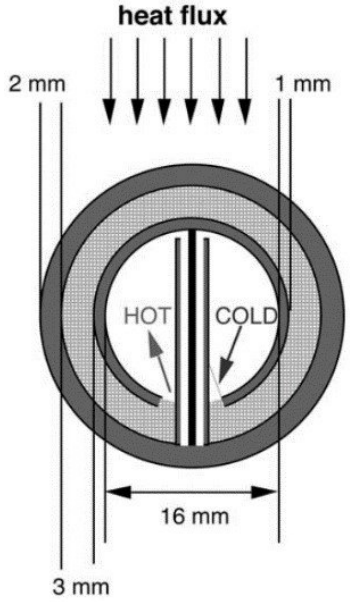

Figure 2.5. Annular channel flow decreases the flow path length, resulting in a more evenly distributed heat transfer along the length of a tube [37].

In addition to porous channels, there are other concepts for improving the heat transfer. Baxi and Wong performed an up-to-date review in 2000 on how these various enhancement methods affect the heat transfer coefficient and friction factor, f (Table 2.2).

Table 2.2. Heat transfer enhancement methods for He-cooled channels [41].

Enhancement method	h **over smooth pipe**	f **over smooth pipe**	$\frac{f}{h}$
Microfins	8	30	3.75
Porous media	5	20	4
Jet impingement	3	7	2.3
Particulate addition	10	30	3
swirl tapes	2	4	2
2D roughness	1.8	3.8	2.1
3D roughness	3	7	2.3
Swirl rod insert	2.5	5	2
Swirl rod insert with 2D roughness	3.5	7	2

Domalapally and Entler provided an overview of the various methods for He-cooled divertors, including the ones listed above, as recently as 2015 [35]. In general, modular techniques would provide better cooling over the entire divertor surface. The flow to each module is regulated to adjust for varying heat fluxes on the surface, which could be used to optimize pumping power. Additionally, the heat transfer coefficient is equivalent for each module, unlike the ITER-like MB design where the local h decreases along the length due to increased bulk fluid temperature. Techniques such as the He-cooled Modular Pin array [42] (Fig. 2.6) have resulted in a h up to 60,000 $\frac{\mathrm{W}}{\mathrm{m^2K}}$, where the pumping power is only 5% of the thermal exhaust power.

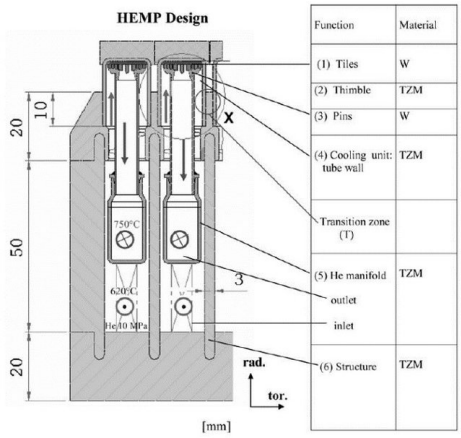

Figure 2.6. A modular concept for a DEMO divertor, He-cooled Modular Pin array produces a high h while maintaining relatively low pressure drop [42].

Jet impingement is also a useful technique for increasing the heat transfer while maintaining a relatively low pressure drop. Jet impingement occurs when a fluid jet strikes a perpendicular surface, which creates a thin, often turbulent boundary layer leading to the aforementioned high h. Jet impingement is often used in electronics [43] and turbine blade cooling [44] as an effective method for removing high heat flux. A He-cooled Modular Jet configuration was designed and tested [45], which is able to withstand at least 10 $\frac{\text{MW}}{\text{m}^2}$ (Fig. 2.7). This study also proposed the use of an integrated design that accounts for the distribution of heat flux on the surface of the divertor (Fig. 2.8). The idea is that a cheaper method of cooling (both in terms of cost and pressure drop) can be used in areas of low heat flux, while more expensive methods are to be used where the heat flux is a maximum. In this way, the cost of manufacturing and pressure drop for the divertor can be minimized.

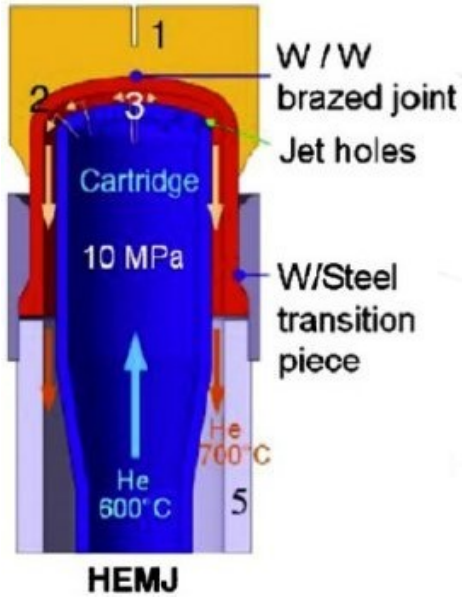

Figure 2.7. Schematic of He-cooled Modular Jet concept [46]. The jet impinges on a tungsten/steel cap forced through a number of small holes in the cartridge.

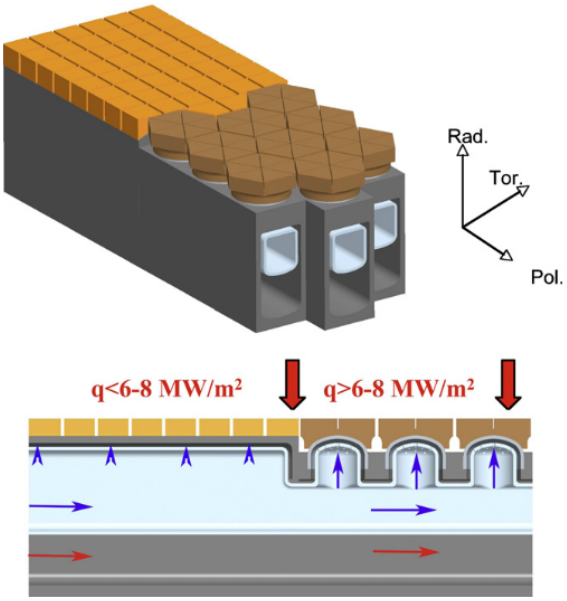

Figure 2.8. Integrated cooling concept for hydraulic optimization [46]. The castellated portion with channel flow supplies cooling in areas where the heat flux is low. In areas of high heat flux, the hexagonal tiles are used in combination with impingement methods.

2.2.2 Water-Cooled

Water-cooled divertors are of special interest because water is cheap and ubiquitous in cooling applications. However, water can vaporize and CHF can lead to dry-out instances where the heat transfer capabilities rapidly decrease, which can permanently damage the coolant channel and surrounding structures. There are a few methods for increasing the CHF in divertor applications, many of which are outlined by Domalapally and Entler [35]. These methods can all be applied to the three main configurations under investigation – flat tile, saddle tile, or monoblock (Fig. 2.9).

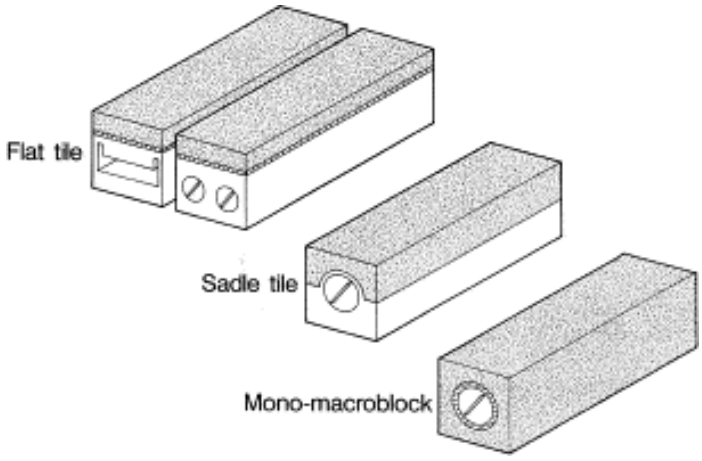

Figure 2.9. Three configurations of divertor target designs. The flat tile (a) consists of a cooling channel topped by a flat refractory material, the saddle tile (b) fits the form of the cooling channel, and the monoblock (c) covers the entire perimeter of the cooling channel [47].

One method of improving CHF is the addition of ice particles, so that the bulk fluid temperature remains constant, but the latent heat of fusion is exhausted in melting the ice. Experiments have been done which can withstand 20 $\frac{\mathrm{MW}}{\mathrm{m}^2}$ [48], but there are many safety issues associated with this method. For example, if the supply of ice terminates, there is no way to protect against CHF.

Like He-cooled concepts, porous media has also been investigated for water flow. The use of heat pipes, which accelerate coolant through capillary action, is particularly useful in fusion divertors because they are completely passive, only contain a small amount of coolant, and can remove heat at a uniform temperature [35]. Actively pumped porous flow configurations have been investigated at Sandia National Labs, where they were able to remove 100 $\frac{\mathrm{MW}}{\mathrm{m}^2}$ [49]. However, there are significant pressure drops that are often associated with water flow in a porous channel. Yet, the use of porous coatings has resulted in an up to 60% increase in the critical heat flux over smooth pipes with relatively similar pumping power [49]. Still, this concept has been largely disregarded due to the increased effect of erosion and corrosion on the coating.

Several mechanical alterations to axial flow have also been tested; these include swirl

tapes, hypervapotrons, and screw tubes. Swirl tapes, which are utilized in the baseline design for the ITER-like monoblock, increase turbulence by constantly rotating the heated boundary layer along the axis of flow. They induce high radial flow velocity, which leads to more mixing and perturbation of the boundary layer, resulting in increased heat transfer (Fig. 2.10a). Hypervapotrons consist of a series of fins that are perpendicular to the direction of flow (Fig. 2.10b). These devices can be operated in the two-phase flow regime, where the fluid between the fins boils, increasing the overall convective heat transfer. Although hypervapotrons have a better thermal performance than swirl tapes, the pressure drop is larger. Finally, screw tubes, which are essentially internally-threaded pipes, are an amalgamation of swirl tapes and hypervapotrons, utilizing the best aspects of each (Fig. 2.10c). Indeed, the heat transfer capabilities are doubled when compared to a smooth tube, but no information is given for the pressure drop over such a device.

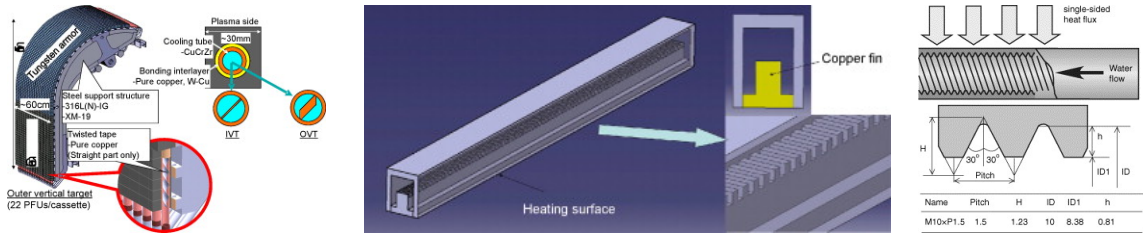

(a) **(b)** **(c)**

Figure 2.10. Heat transfer enhancement techniques for axial flow: (a) swirl tape [50], (b) hypervapotron [51], and (c) screw tube [52]. The swirl tape increases mixing by constantly disturbing the boundary layer. The hypervapotron utilizes two-phase flow between the fins, but the pressure drop is fairly large. The screw tube is a conceptual melding of the two previous designs and is an effective method of increasing heat transfer without sacrificing significant pressure drops.

Again, jet impingement is one method of increasing heat transfer without significant pressure drops. One of the downsides to jet impingement is a high local h at the stagnation point where the jet strikes the surface, but that then quickly drops off downstream. This can be alleviated by constraining the jet to a concave geometry, where the local velocity can be altered to achieve a more consistent h (Fig. 2.11), but

this does lead to a larger pressure drop.

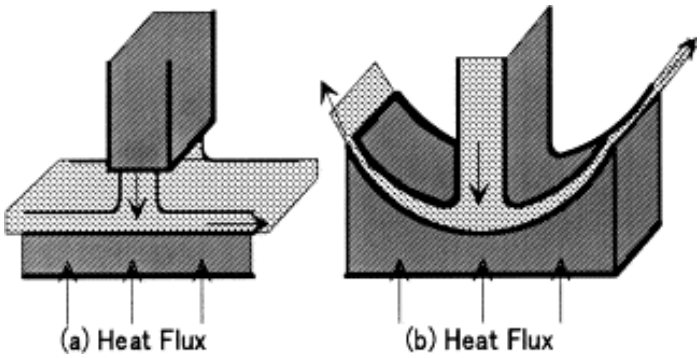

Figure 2.11. Two geometries for jet impingement. Subfigure (a) offers a lower pressure drop, but (b) offers a more even heat transfer coefficient across the heated surface [53]

More recently, work has been done at OTI by Nicholas et. al to alleviate the issues associated with jet impingement [54, 55]. The idea of a High Pressure Jet Cascade (HPJC) separates the impinging jets into discrete sections so that the fluid flow path is shorter, flattening the heat transfer profile across the heated surface. HPJC is manufactured as a modular, hexagonal, laminate structure [54] (Fig. 2.12). This cascading flow path uses a lower mass flow rate while sacrificing for a larger pressure drop. Thermally sprayed thin-films were applied to the surface to create a heat flux, and water at various flow rates was supplied at 30 °C and 150 bar.

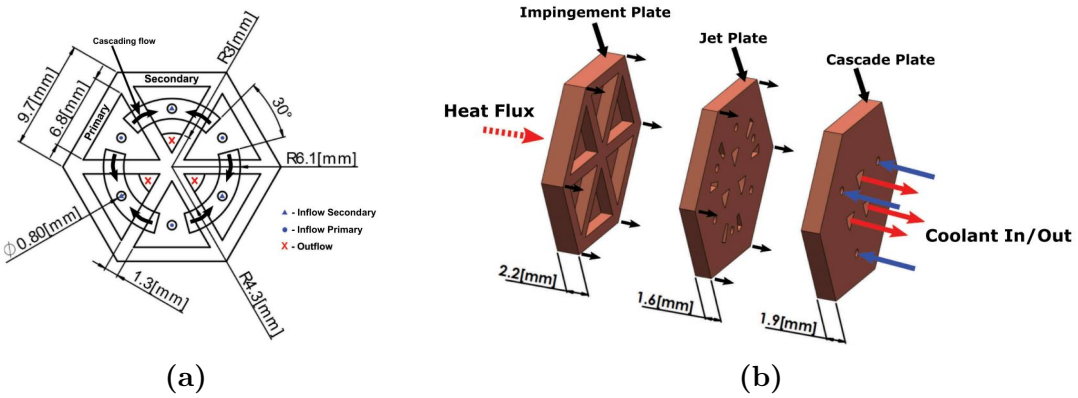

Figure 2.12. Flow path diagram (a) and schematic of an HPJC module (b) [55]. The flow is channeled through the jet plate at which point it impinges on the primary cavities. The flow leaving these primary cavities cascades to impinge on secondary cavities before going back out through the coolant exit.

The experimental data from this work was then compared to other divertor target concepts through a parameter known as *wall overheat*, τ_s (Fig. 2.13) [56]. Here, $\dot{m}$ and $\dot{m}_{id}$ are the actual and ideal mass flow rates, c_p and c_{id} are the actual and ideal specific heat capacity, and T_s, T_{ci}, and T_{ce} are the temperatures at the external surface of the channel, coolant inlet, and coolant exit (Fig. 2.13). The ideal model is defined by an infinite solid thermal conductivity, ensuring isothermal conditions, and that the exit temperature of the fluid equals the component temperature. It should be noted that τ_s is independent of heat flux ($\dot{Q}$) and solid thermal conductivity (k_s). Additionally, T_s can be chosen as the maximum or surface averaged temperature, for instance, depending on user preference.

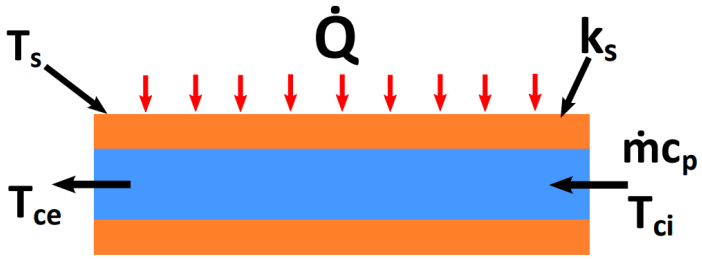

Figure 2.13. Simplified schematic used for derivation of τ_s [56]. The difference between the maximum possible heat extraction and actual heat removal is that the heat sink is treated as isothermal, and the coolant exit temperature equals the heat sink temperature.

$$\tau_s = \frac{\dot{m}c_p}{\dot{m}_{id}c_{id}} = \frac{T_s - T_{ci}}{T_{ce} - T_{ci}} = \frac{\text{maximum possible heat extraction}}{\text{actual heat removal}} \tag{2.1}$$

For a specific dimensionless mass flow (m^*), an efficient cooling system will minimize τ_s, where m^* is defined as:

$$m^* = \frac{\dot{m}c_pL}{k_sA} = \frac{\text{thermal fluid capacity flux}}{\text{solid thermal conductance}} \tag{2.2}$$

Where L and A area a reference length and area scale, respectively. Nicholas compared this figure of merit to other divertor target concepts, and HPJC has the lowest wall overheat when using peak surface temperature as the choice for T_s (Fig. 2.14).

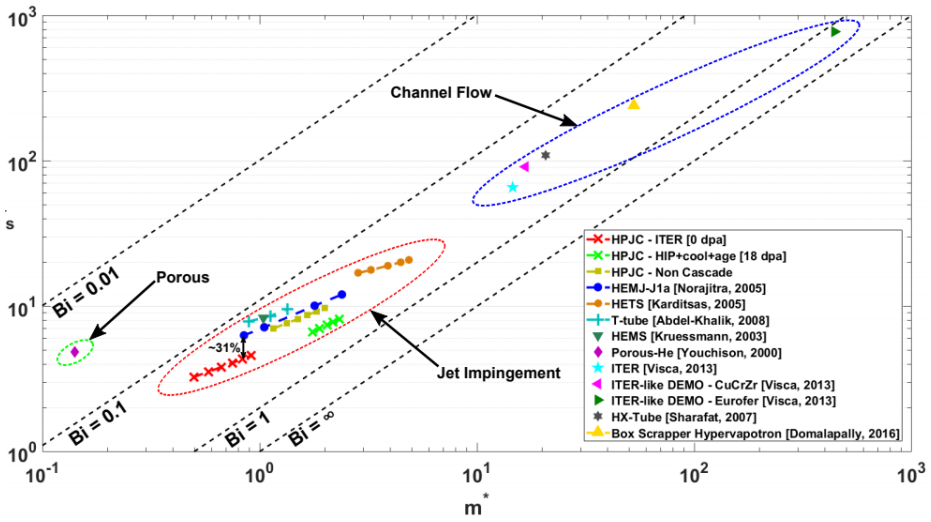

Figure 2.14. Variation of the wall overheat with non-dimensional mass flow rate for a range of past and present divertor proposals.[1]

2.2.3 Liquid Metal-Cooled

LM-based devices still present many challenges, such as handling difficulty due to reactivity with air, corrosive properties, MHD-reduced heat transfer capabilities [33]. However, there are many positives to using liquid metals:

- They have high thermal conductivity and large heat capacity, leading to high heat transfer rates and efficient power exhaust.
- Lithium-based divertors can be used to breed tritium.
- They are practically free from neutron damage and can be re-circulated for a device's lifetime. [57]
- They have a low Z, meaning that they will not contaminate the plasma as much as other kinds of armor with high Z, like tungsten.

There are a variety of material options that have been explored for LM concepts, including tin and gallium, but lithium is by far the most popular [57]. There are two main concepts for LM-based divertors. The first of which is a free-flowing concept,

[1]Paper by Nicholas et al. has yet to be published, so citation data is not available.

where LM flows over the face of the divertor and is continuously recycled. The second concept, proposed by Evtikhin et al. in 2002, is a Capillary Porous System (CPS) [58].

One of the main challenges presented by the free-flowing concept is LM splashing caused by MHD effects. Ruzic et al. took advantage of both the thermoelectric and MHD effects to reduce splashing in a passive-pumping design known as Lithium Metal Infused Trenches [59]. LM flows through trenches in which the exposed surface is hotter than the bottom of the trench, producing an electric current via the thermoelectric effect. These trenches are oriented such that the plasma's magnetic field produces a $j \times B$ force, driving the LM along the length of the trench Fig. 2.15.

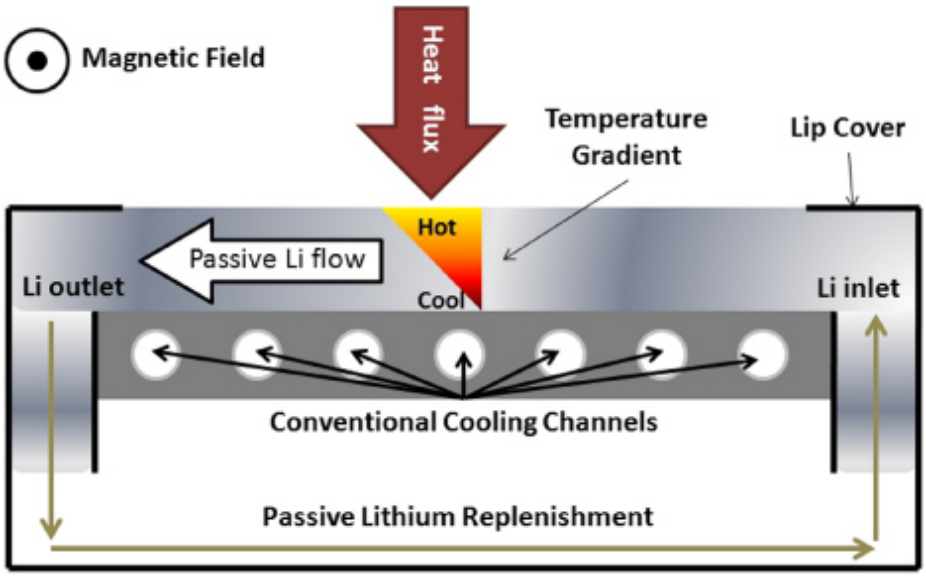

Figure 2.15. Passive cooling mechanism for lithium metal infused trenches [59]. The design takes advantage of the thermoelectric and magnetohydrodynamic effects, whereby a current is induced along the temperature gradient. The magnetic field and current passively pump the coolant. A conventional cooling mechanism extracts heat from the device.

The CPS design embeds LM in a porous structure, taking advantage of the strong capillary forces that hold it in place. As the LM is not actively being replaced, it is typically combined with a water-cooled heat exhaust [58]. The CPS reduces the risk of splash and is considered a more conservative design than free-flowing ones, but it

has problems associated with corrosion and surface wetting [57].

2.3 Compound Parabolic Concentrators

The experimental setup necessitates some kind of optical concentration device so that the spatial power density can be bolstered from $\sim 1\ \frac{\mathrm{MW}}{\mathrm{m}^2}$ to at least $5\ \frac{\mathrm{MW}}{\mathrm{m}^2}$. Any laser diverges due to its finite-length cavity. The VCSEL modules have a divergence of 10°, meaning that the irradiance reduces the farther away from the source that it travels (Fig. 2.16).

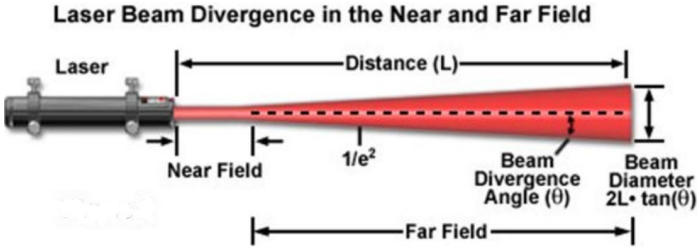

Figure 2.16. Diagram of how a laser diverges from a point source [60]. The irradiance decreases the farther the light travels from its source.

Assuming a point-source, the far-field irradiance I can be described by Eq. (2.3), where Q_e, A_e, and D_e are the power, area, and diameter of emission at a distance L_e away from the emitting source, and θ_{div} is the divergence angle of the laser source. Thus, the irradiance decreases quadratically with L_e.

$$I = \frac{\dot{Q}_e}{A_e} = \frac{4\dot{Q}_e}{\pi D_e^2} = \frac{\dot{Q}_e}{L_e^2 \tan^2 \theta_{div}} \tag{2.3}$$

Typically, some type of optical lens system is used to focus a divergent beam on a focal point, as in Fig. 2.17. However, now considering the many individual lasers that comprise the VCSEL module, this lens-based focusing is not suitable for an array of lasers that are each divergent. Therefore, some other type of *non-imaging optical* concentrator is needed.

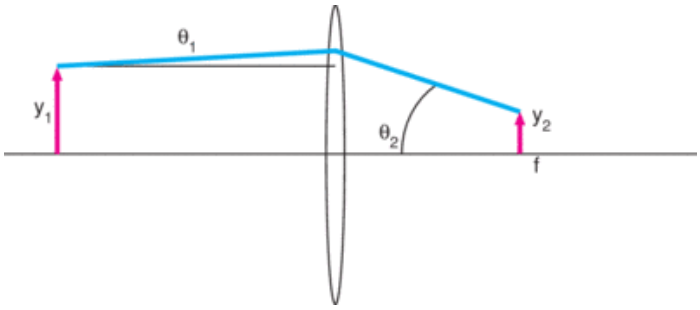

Figure 2.17. Single lens optical system that can focus a divergent beam [61]. This type of lens is common in imaging optics, but is not particularly useful for non-imaging optics which aims to produce a certain irradiance pattern.

Non-imaging optics is composed of a light source, optics, and target. The light source is redirected by the optic to produce a desired irradiance pattern on a target. As a contrast, *imaging optics* is composed of an object, optic, and image, where an optic collects the light from an object and forms it into an image; thus there is a coherence of points forming the image and points that come from the object. A theoretical description of non-imaging optics is provided in [62]. The basic idea in non-imaging optics is that an Emitter (E) radiates light onto an Optic (O), which deflects the light into an appropriate distribution on a Receiver/Target (R) (Fig. 2.18).

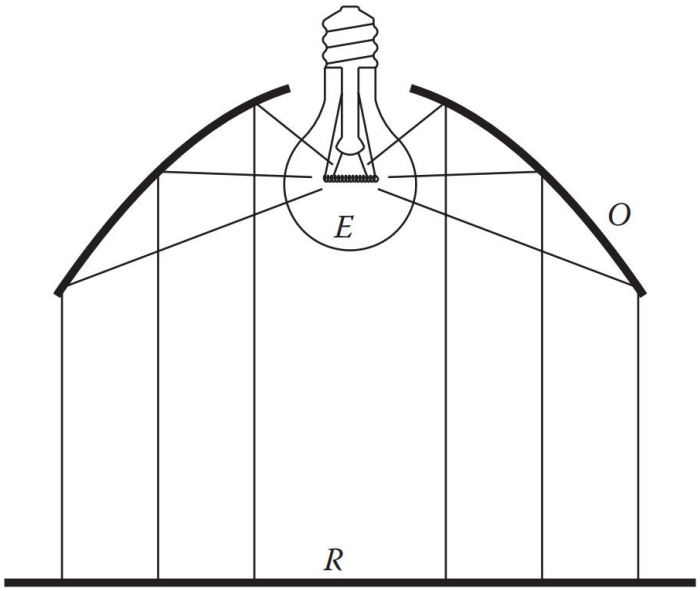

Figure 2.18. Three components of non-imaging optics (emitter, optic, and receiver) produce a specified irradiance pattern on the receiver [62].

If no power is lost during this process, a characteristic called *étendue*, which can be thought of as a trade-off between the angle and area with which a light source passes through an aperture, is conserved according to Eq. (2.4) (Fig. 2.19).

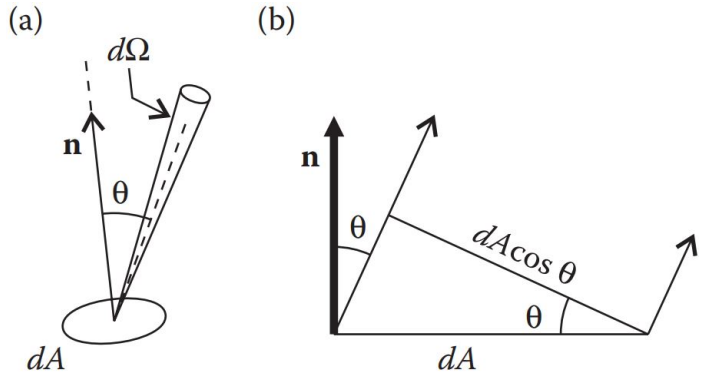

Figure 2.19. Illustration in 3D (a) and 2D (b) of the important characteristics that relate to the conservation of étendue. Étendue, which can be thought of as how 'spread out' light is over an area dA and angles θ and $d\Omega$, is conserved as long as the total power is kept constant.

$$dU = n^2 dA \cos\theta d\Omega \tag{2.4}$$

Where dU is the étendue in units of m^2 sr, n is the refractive index of the medium through which the light passes, dA is the area crossed by the light with normal $\mathbf{n}$, θ is the angle of the flux from the normal, and $d\Omega$ is the solid angle which contains the flux. To create an optic that concentrates all of the light from E onto R, there is a balance between the area of the aperture and the divergence angle, as illustrated by Fig. 2.20. It is often preferable to minimize dA to minimize the cost of material, and this can be achieved by the edge-ray principle. The optimal design is one where all of the flux is captured on R with the smallest possible dA, such that the rays at the edges of E are transmitted to the edges of R.

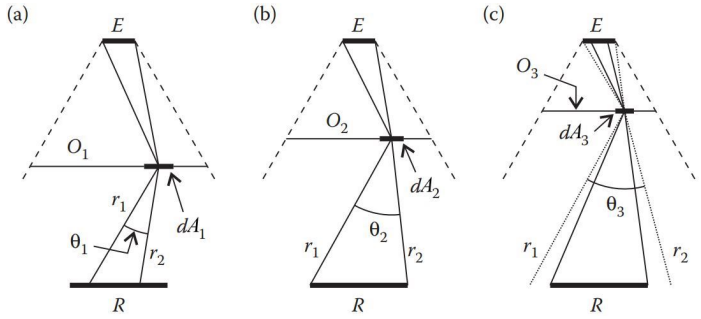

Figure 2.20. (a) The large area of dA_1 allows light from E to fall on R. (b) The optimal solution for which the edge-rays from E intersect the edge of R. (c) Some of the light from E does not strike R because the optic dA_3 is too small [62]

The Compound Parabolic Concentrator (CPC) is a non-imaging optical device that minimizes the size of the output aperture for a given input aperture. Therefore, concentration and thus output irradiance are maximized for a given light source. In 2D space, the CPC is composed of two rotated parabolas (mirrors of each other) such that the focus of one parabola is the exit point of the other (Fig. 2.21). The conservation of étendue and the edge-ray principle are necessary to come to this design.

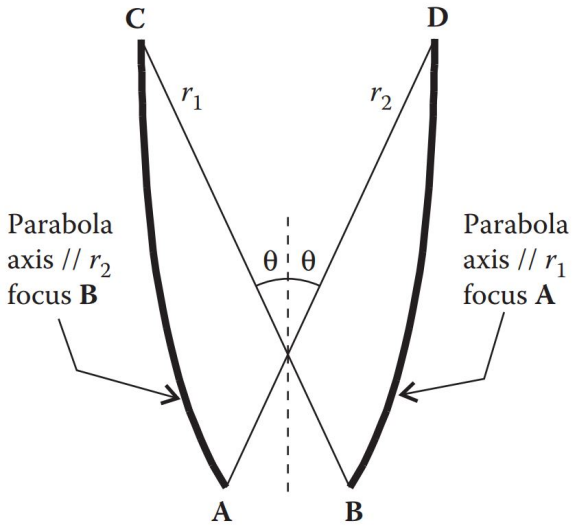

Figure 2.21. A CPC is a concentrator with entrance aperture CD, that accepts radiation, making a maximum angle of $\pm\theta$ with the vertical, and concentrates it into AB [62]

A CPC has a characteristic acceptance angle θ_{acc} from the vertical such that any rays with $|\theta|$ greater than θ_{acc} are rejected back out the entrance (Fig. 2.22). Angles less than θ_{acc} are also transmitted.

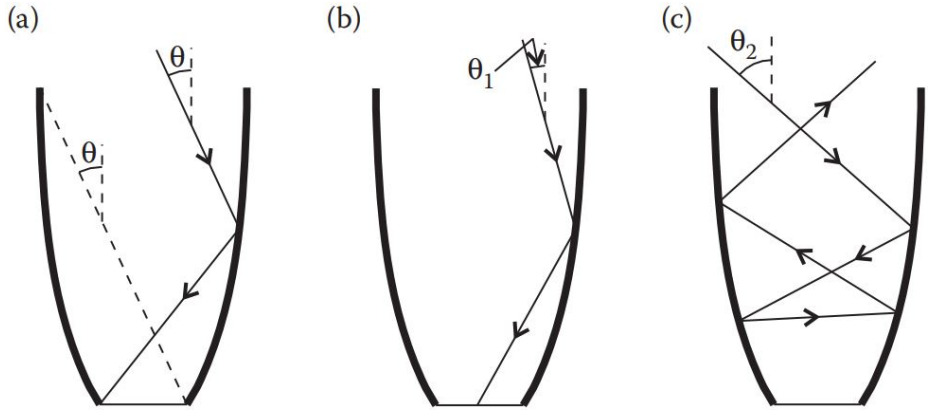

Figure 2.22. Rays can either be transmitted or rejected by an ideal 2D CPC, depending on their entrance angle. Rays in (a) enter at θ_{acc} meaning they will strike the edge of R. For rays with $|\theta| < \theta_{acc}$ (b), all are transmitted. Rays for which $|\theta| > \theta_{acc}$ are eventually reflected back out of the entrance aperture [62]

For an ideal 2D CPC, the follow equations describe the concentration ratio C and the height h_{cpc}. To clarify, any lowercase a refers to aperture lengths in a 2D CPC, while an uppercase A pertains to aperture areas in a 3D CPC.

$$C = \frac{a_{in}}{a_{out}} = \frac{1}{\sin\theta_{acc}} \tag{2.5}$$

$$h_{cpc} = a_{in}\frac{1+\sin\theta_{acc}}{2\tan\theta_{acc}} \tag{2.6}$$

Where a_{in} and a_{out} are the entrance and exit half widths of a CPC. As θ_{acc} approaches zero, both h_{cpc} and C approach infinity; so for small acceptance angles the height of the CPC becomes very large, but the concentration ratio also becomes large. Another note of importance is that the exit angle of light can range from 0° to 90°. So to capture all the transmitted flux, the target must be located at the exit. In practice, it is difficult to place receivers where they touch the CPC at its exit aperture because

the target can then conduct heat back to the CPC. It is typically more common to place the receivers close to the exit without actually touching.

By rotating the parabolas in Fig. 2.21 around their central axis, a 3D axisymmetric CPC is formed. Now, the entrance and exit area are defined as A_{in} and A_{out}, respectively. Considering a 3D CPC, the concentration ratio then becomes

$$C = \frac{A_{in}}{A_{out}} = \frac{n^2}{\sin^2 \theta_{acc}} \tag{2.7}$$

Where n is the refractive index of the CPC material. For lower values of θ_{acc}, the concentration ratio raises significantly more quickly than for the 2D case. Additionally, if the CPC is hollow such that the medium from E to O to R is constant, then n is taken as unity. The height of the CPC remains the same for both the 2D and 3D cases.

In reality, light sources are not typically collimated and in fact diverge diverge. Some of these divergent rays are skew to the CPC surface and will not be transmitted to R. Thus, not every ray with $|\theta| \leq \theta_{acc}$ is successfully transmitted. It is therefore necessary to define a transmission efficiency η_τ as

$$\eta_\tau = \frac{\text{Flux through } A_{out}}{\text{Flux through } A_{in}} = \frac{\dot{Q}_{out}}{\dot{Q}_{in}} \tag{2.8}$$

For an ideal 2D CPC, η_τ is equal to 1 for $|\theta| \leq \theta_{acc}$ and 0 elsewhere. Even for ideal 3D circular CPC's, η_τ is not unity (Fig. 2.23).

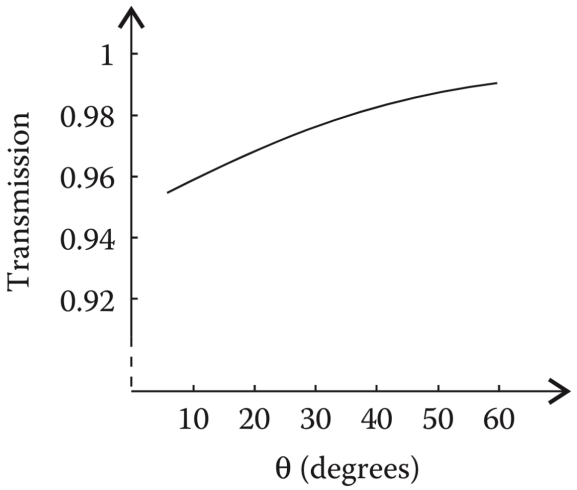

Figure 2.23. Transmission efficiency for rays within the design angle, θ_{acc}, for an axisymmetric, 3D CPC [62].

CPC's have found use for collecting and concentrating solar energy [63–66], solar-based thermoelectric generators [67], and light source concentrators [68]. They are used in industrial applications like these because they offer the most compact form of non-imaging concentration.

Darbe's thesis work describes the manufacturing and performance of several CPC's with different materials and cross-sectional profiles [68]. Real CPC's are not ideal and will have transmission efficiencies below those predicted by Fig. 2.23. Darbe's results show actual efficiencies as high as 92±2% for an acrylic concentrator of circular profile with $C = 15.6$ and as low as 67.7±8% for a plastic concentrator of square profile with $C = 42.25$. These efficiencies are significantly lower than those predicted by ray-tracing simulation software, and the losses arise from a variety of factors:

- Surface scattering: Manufactured components have an inherent surface roughness which can lead to diffuse reflection and power loss. A surface is said to be smooth in its relation to the wavelength (λ) of light striking the surface if the

Rayleigh criterion is satisfied [69]:

$$\Delta h < \frac{\lambda}{8 \cos \theta_i} \tag{2.9}$$

Where Δh is the root mean square of surface roughness, and θ_i is the angle of incidence. For design, it is often assumed that the distribution of diffuse reflection is Lambertian. Lambertian scattering is essentially a finite distribution:

$$I = I_0 cos(\theta) d\Omega dA \tag{2.10}$$

Where the intensity of the flux contained in a solid angle $d\Omega$ is proportional to the incident intensity, I_0, and the cosine of the angle of incidence. Fig. 2.24 provides a illustration of lambertian scattering.

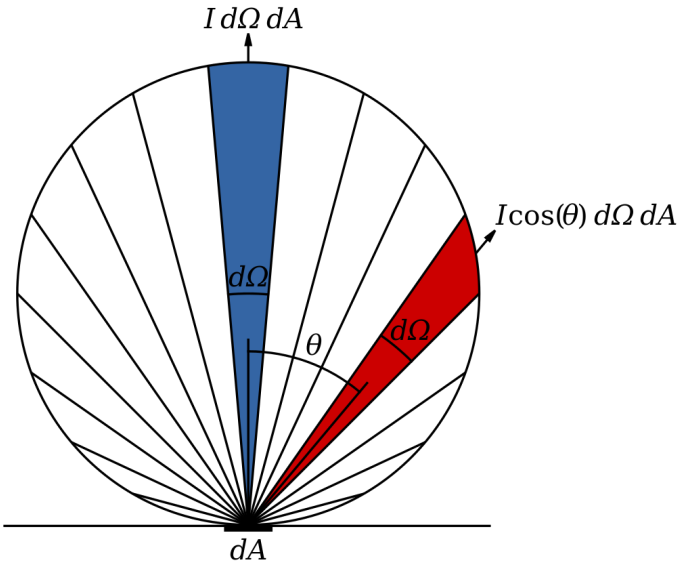

Figure 2.24. Lambertian scattering is a type of light scattering distribution. The intensity of reflected flux contained with $d\Omega$ is proportional to the original intensity and the cosine of the angle of incidence [70].

- Fresnel reflection: Fresnel reflectivity r is defined such that a surface has a reflectivity of 1 if none of the incident energy is absorbed by the material and

0 if all of the energy is absorbed. No real surface can have a reflectivity of 1, and therefore some power is lost at the material interface. The reflectivity depends on λ, but some highly-engineered mirrors for laser applications can have reflectivities from 99.8% to 99.999% for wavelengths in the near ultraviolet range [71]. Reflectivity r can also be defined as 1-α, where α is the absorbtivity coefficient of a material.

- Volume scattering: The volume scattering function is another inherent optical medium property and is defined as the dispersion of light in all directions from an infinitesimal scattering volume once it encounters a new medium [72].
- Shape Inacurracy: Due to machining tolerances, the final shape of a CPC will not exactly match its nominal shape, even ignoring surface roughness.

It was found that square CPC's are typically less efficient than circular CPC's because skew rays can bounce close to the corners and be reflected back out. Cooper et al. performed a numerical study on the transmission capabilities of hollow CPC's with polygonal cross-sections compared to circular profiles [73]. Circular CPC's are inherently difficult to manufacture due to the two-dimensional curvature, and polygonal (or faceted) CPC's offer a cheaper alternative with one-dimensional curvature. Timinger et. al found that by slightly altering the parabolic profile of faceted concentrators, the transmission efficiency can be optimized [74]. However, the numerical study by Cooper et al. did not optimize the axial profiles according to the method prescribed by Timinger et. al because it leads to a maximum 5% increase in efficiency and depends on the reflectivity of the concentrator, which may diminish over time. The optical efficiency for various polygonal CPC's is compared to a circular profile (Fig. 2.25) and one of the more anomalous results shows that for small θ_{acc}, square CPC's actually have higher efficiencies than pentagonal or hexagonal. Additionally, the average number of reflections is higher for the fewer sides a CPC has, which can lead to more losses based on surface roughness and fresnel losses. Normalized flux profiles for various shapes are shown in Fig. 2.26.

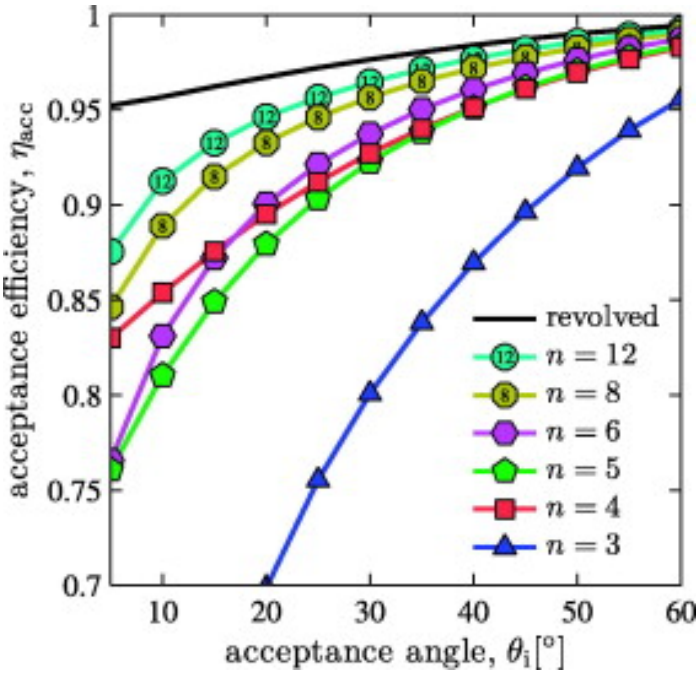

Figure 2.25. Optical efficiency for several polygonal (faceted) CPC's [73]. Square CPC's show an anomolous behavior where their acceptance efficiency is higher than that of pentagonal and hexagonal for low θ_{acc}.

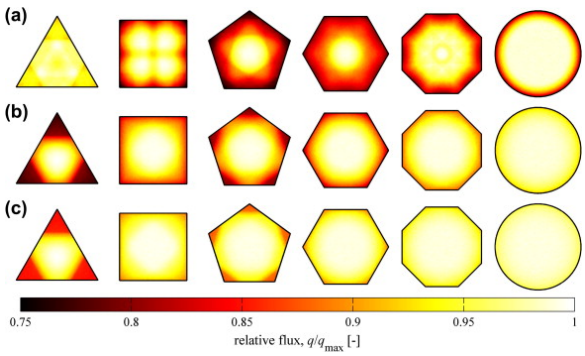

Figure 2.26. Normalized irradiance profiles for circular and polygonal CPC's with acceptance angles of (a) $\theta_{acc} = 5°$; (b) $\theta_{acc} = 30°$; and (c) $\theta_{acc} = 45°$ [73].

Other ray-tracing studies have been performed to consider how a collimated beam concentrated by an axisymmetric CPC is affected by a variety of parameters [75]. For example, η_τ decreases approximately at twice the rate of reflectivity because a single ray is reflected roughly twice on average before reaching the receiver (Fig. 2.27).

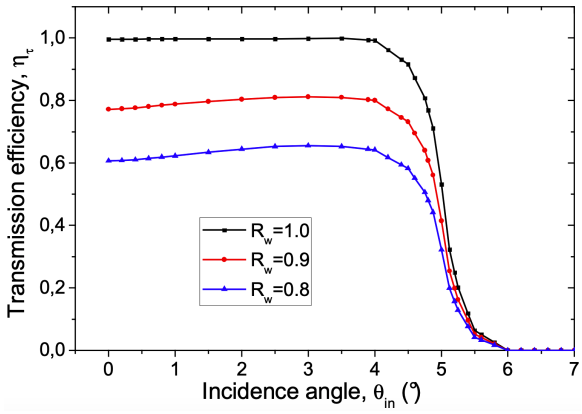

Figure 2.27. Optical transmission efficiency calculated for three wall reflectivities [75]. A collimated beam strikes a CPC with $\theta_{acc} = 5°$at different angles of incidence. The reflectivity of the CPC plays a large role in the overall transmission efficiency.

Chapter 3

CPC Design

3.1 Defining the CPC

The experimental setup consists of the three elements in non-imaging optics: the four VCSEL lasers (emitter E), concentrator(s) (optic O), and the actively-cooled plasma-facing component mockup (receiver/target R) (Fig. 3.1). It was decided to use CPC's to concentrate the laser power because they offer the most compact concentration, thus reducing material needs, and achieve the highest theoretical concentration ratio.

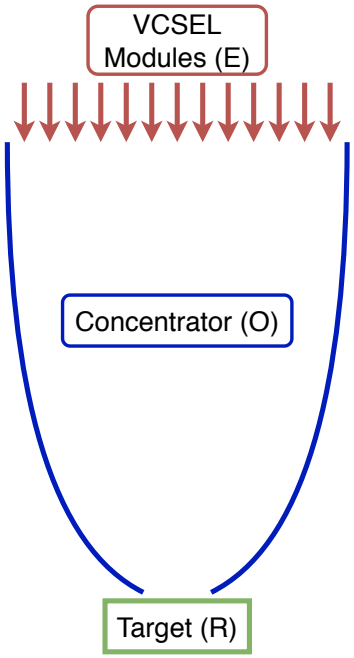

Figure 3.1. Experimental setup of non-imaging optics

The functional requirements for the optical performance of the CPC are as follows:

- The CPC must produce an irradiance which has an average irradiance, I_{avg}, greater than 5 $\frac{\text{MW}}{\text{m}^2}$.
- The irradiance must be 'even' enough such that one standard deviation, I_{std} below the mean must be greater than 5 $\frac{\text{MW}}{\text{m}^2}$.
- The output area of the CPC must be greater than 10 cm^2 so that relevant sized targets can be tested.

Generally speaking, the various designs for the setup can be broken down into two categories where (1) each laser acts as an emitter and has an associated concentrator or (2) the four lasers act as a single emitter and therefore there is one concentrator. Additionally, the lasers can be rotated to any angle in space that optimizes the irradiance on the target for either of the two configurations.

Using a CPC for each laser has a variety of benefits. The entrance aperture of an individual CPC can be minimized to match the emittance area of one laser, in contrast to (2) where there are portions of the entrance aperture that receive no flux because of the packing density of an array of VCSEL modules. Additionally, the CPC(s) may need some kind of cooling to abate the radiative heat from the target. The smaller, individual CPC's would be easier to cool because of an increase in surface area per unit volume when compared to a large single CPC. However, some of the drawbacks of this configuration arise from the conservation of étendue discussed in Section 2.3.

It is impossible to align the axes of multiple CPC's with the center axis normal of the target surface. In a configuration like this, the concentrators must be placed at some angle incident to the target. The nature of CPC's dictates that the outlet angles of rays vary from 0°(parallel) to 90°(perpendicular). Thus by angling a CPC farther away from the target surface normal, the total absorbed power will decrease. Additionally, moving the target farther from the exit aperture decreases the total flux felt by the target. Fig. 3.2 demonstrates how the conservation of étendue applies to

a CPC.

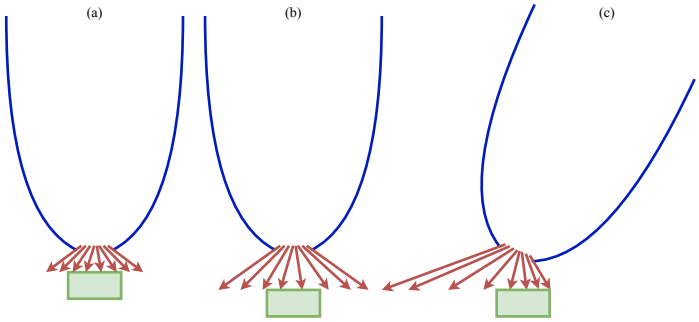

Figure 3.2. The target receives maximum flux when it aligns with the CPC exit aperture (a). The widely varying output angle from the CPC means that less power is absorbed the farther away the target is (b). Angling the CPC away from the target causes a reduction in surface flux due to the conservation of étendue

Treating the four lasers as a single emitter reduces the complexity of the system, as there is a need for only one CPC. The alignment problem is simplified in that the axis of the CPC can align with the normal to the target. Moreover, although the thermal mass of a large CPC is higher, the cooling system can be simplified in that only one optic has to be cooled, even if the cooling power is larger. One downside for a single CPC is that the actual emitting area is only a portion of the total area encapsulated by an array of the four VCSEL modules. In fact, if the modules are packed together in a 2x2 array as tightly as possible, only 28% of the bounded area is emitting (Fig. 3.3). However, the modules can be angled inwards so that this percentage decreases and the entrance aperture minimized. But this solution necessitates a larger θ_{acc} according to Eq. (2.7), which decreases the concentration ratio C.

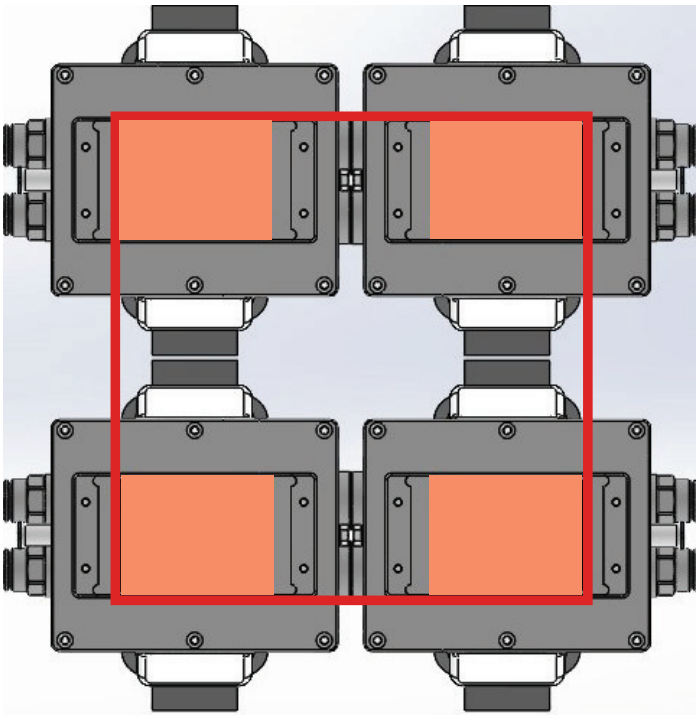

Figure 3.3. A 2x2 laser module array only utilizes 28% of the emittance aperture

Although the most logical array shape for (2) is 2x2, a 4x1 array and corresponding CPC were also considered. This configuration results in an area-emitting packing percentage of 33% (Fig. 3.4). However, the aspect ratio of the exit aperture was 7.8:1, which was deemed too large to reasonably test targets of interest, so this concept was disregarded.

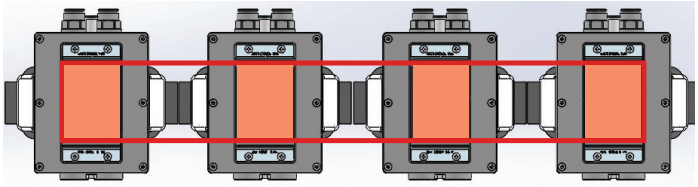

Figure 3.4. A 4x1 laser module array only utilizes 33% of the emittance aperture

The relevant geometric dimensions of the CPC are referenced in Fig. 3.5. Here, a_{in} and a_{out} are the half-widths of the entrance and exit apertures, respectively. The height, h_{cpc}, and the half-width of emission, w_e, are also important dimensions for defining a 2D CPC. The area of the entrance and exit aperture, A_{in} and A_{out}, are

used to calculate the concentration ratio.

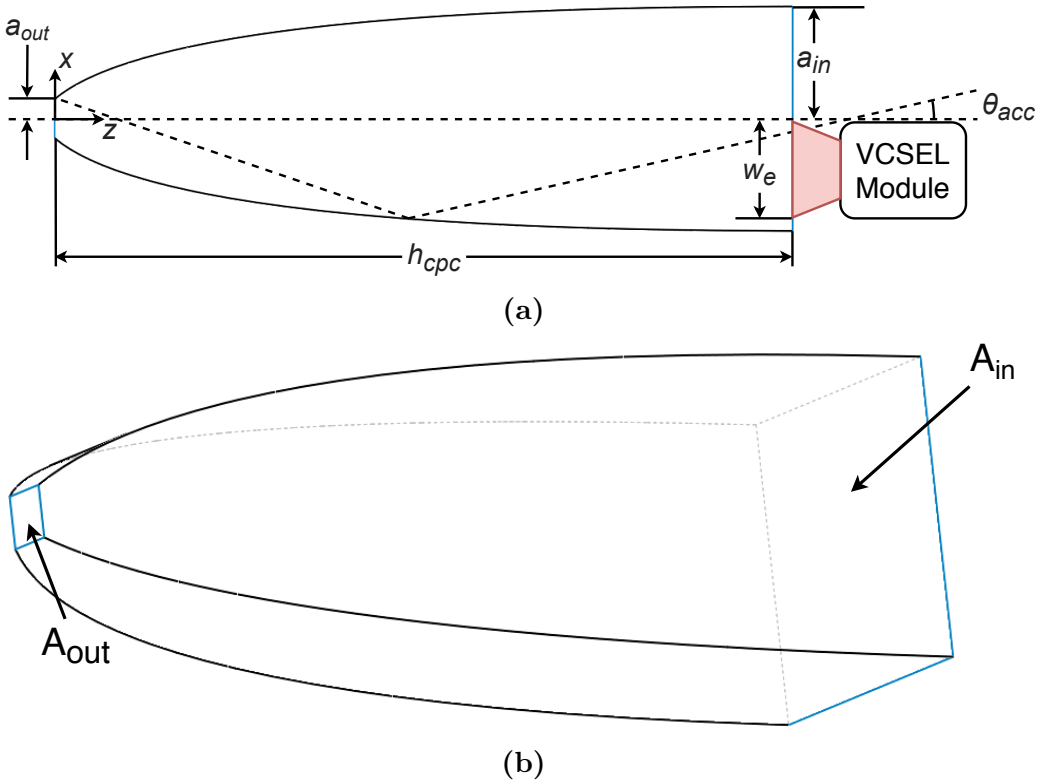

Figure 3.5. Reference for geometric parameters used to define a CPC in 2D (a) and 3D (b). The coordinate frame is located at the center of the exit aperture.

The 2D curve of a CPC can be defined by a parametric equation, with t_{cpc} as the parametric variable in radians:

$$\begin{cases} x_{cpc} = a_{out}\cos(t_{cpc}+\theta_{acc})\frac{1+\sin\theta_{acc}}{\sin^2\frac{t_{cpc}}{2}} \\ z_{cpc} = a_{out}\frac{1-\cos(t_{cpc}+2\theta_{acc})+2\sin(t_{cpc}+\theta_{acc})}{\cos t_{cpc}-1} \end{cases} \qquad \frac{3\pi}{2}-\theta_{acc} \le t_{cpc} \le 2(\pi-\theta_{acc}) \tag{3.1}$$

Where a_{out} is the distance from the central axis to the focus of one parabola. The value of a_{out} can be found by reordering Eq. (2.5).

$$a_{out} = a_{in}\sin\theta_{acc} \tag{3.2}$$

For the design, a_{in} was made slightly larger than half the width of emission, w_e, at the point where the lasers cross the plane of the CPC entrance (Eq. (3.3)). This 2%

increase was chosen to account for any small misalignment between the module and CPC.

$$a_{in} = 1.02\frac{w_e}{2} \tag{3.3}$$

The most straightforward configuration given the rectangular shape of the VCSEL modules is a rectangular CPC to maximize concentration for a certain θ_{acc}. Although a circular CPC is inherently more efficient than a rectangular one, there are a few problems with a circular concept. An inscribed circular CPC would not capture all the laser light which not only does not utilize the full power capabilities of the VCSEL modules, but is also very unsafe (Fig. 3.6a). A circumscribed circular CPC would capture all the flux, but only a small portion of the entrance aperture experiences this flux (Fig. 3.6b). Thus, the design began with a rectangular aperture.

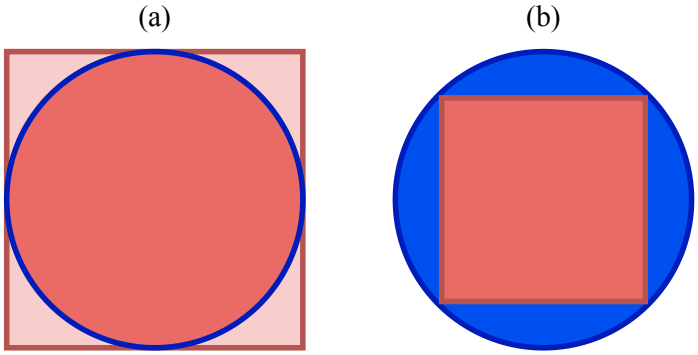

Figure 3.6. Inscribed circular CPC does not capture all the emitted light (a). Circumscribed cicular CPC captures all the light but requires more material and a higher concentration ratio (b)

For both the single and multiple CPC configurations, the inlet aperture will have different width and depth because the aspect ratio of the emitting area is not 1:1. It is therefore necessary to define equivalent lengths for the second direction as b_{in} and b_{out}. For instance, when using a CPC with each module, the aspect ratio is 0.76:1, and for a single CPC aligned with the modules' axes it is 0.98:1.

Because h_{cpc} depends on a_1 according to Eq. (2.6), the taller of the two parabolic

curves that make up the rectangular CPC must be truncated to match the height of the lower. Thankfully, the parabola is roughly parallel to the CPC axis near its entrance, meaning that truncation does not reduce the entrance aperture area (and therefore C) significantly [76].

3.2 Configuration Choice

With these principles in mind, several designs were created and simulated in LightTools, a ray-tracing simulation software provided by Synopsis. All simulations were performed with 10^7 rays, a total input power of 9.6 kW (2.4 kW from each VCSEL module), ideal conditions with mirror surfaces ($r = 1$), and a divergence half-angle of 10° (which contains ∼95% of the flux) [77].

Furthermore, the surfaces are assumed to be perfectly smooth, meaning that the Rayleigh criterion (Eq. (2.9)) is satisfied. Given a wavelength of 980 nm and conservatively assuming that $\theta_i = 90° - \theta_{div}$, the standard deviation of surface roughness must be below 705 nm. Hand-polishing can easily achieve average surface roughness below 400 nm [78], and [79] suggests that one can obtain the approximate standard deviation by multiplying this value by 1.1, resulting in 440 nm, which is less than the Rayleigh criterion of 705 nm. Therefore, by polishing the CPC, the assumption that the surfaces are optically smooth is valid.

The average error for a receiver is estimated by LightTools in post-processing, where the error is calculated as one divided by the square root of the number of rays reaching a pixel [80]. It is typically recommended that the error be less than 10% for the desired resolution. Once the desired resolution was chosen, 10^7 rays were enough such that the average errors for all runs were below 2%.

For all designs, it was only necessary to import surfaces (and not solid bodies) into LightTools, thus decreasing the number of computational nodes. Instead of meshing these surfaces, LightTools treats them as analytic surfaces, meaning that they can

be represented by a family of continuous equations as opposed to a discrete surface mesh [80]. There was, therefore, no need to perform a mesh independence study.

The designs can be separated into the following categories:

1. Single rectangular CPC whose axis aligns with those of the four VCSEL modules;
2. Single rectangular CPC whose axis does not align with those of the four VCSEL modules;
3. Single rectangular CPC with mirrors;
4. Single octagonal CPC with mirrors;
5. Multiple rectangular CPC's whose axes align with those of corresponding VCSEL modules but do not align with the normal of the target surface

Design 1 (Fig. 3.7) is the simplest design. The benefits of this design include ease of alignment, mounting the laser modules, and a minimal acceptance angle. However, there is wasted space in the entrance aperture where there is no flux.

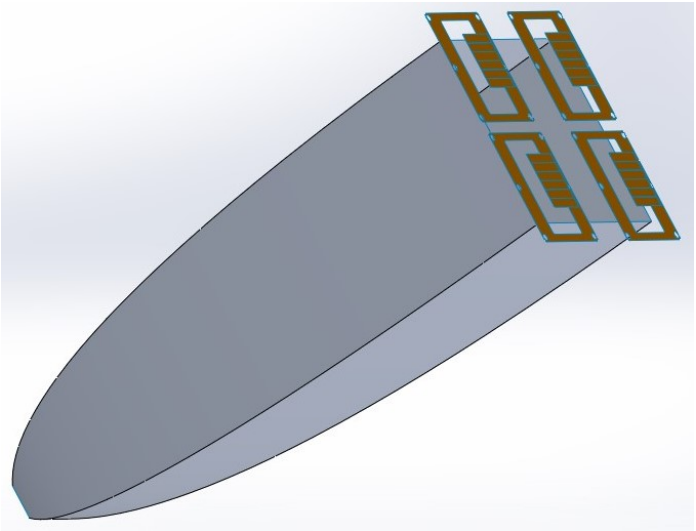

Figure 3.7. Design concept #1 for CPC. The axes of each laser module are parallel to the axis of the CPC.

Design 2 (Fig. 3.8) provides ease of target and CPC alignment, but it is more difficult

to design fixtures for the the laser modules. The modules are angled such that their axes intersect at the center of the exit aperture. While the entrance aperture area decreases by roughly 9% compared to Design #1, θ_{div} increases from 10°to 18.8°because the modules are tilted.

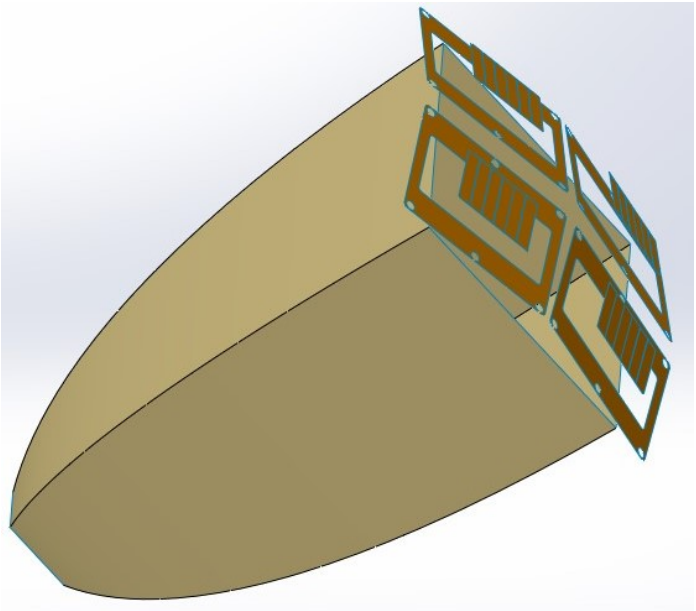

Figure 3.8. Design concept #2 for CPC. The axes of each laser module are angled such that they intersect the center of the exit aperture of the CPC.

Design 3 (Fig. 3.9) achieves a compromise between 1 and 2. Indeed, the lasers are placed such that their normal is perpendicular to the normal of the CPC. The mirrors are tilted at 45° with respect to the module normal. By rotating the lasers in their plane, flux can flow through more of the entire entrance aperture while maintaining a minimum θ_{acc}. However, this setup is significantly more complicated due to mounting difficulties and the additional mirrors.

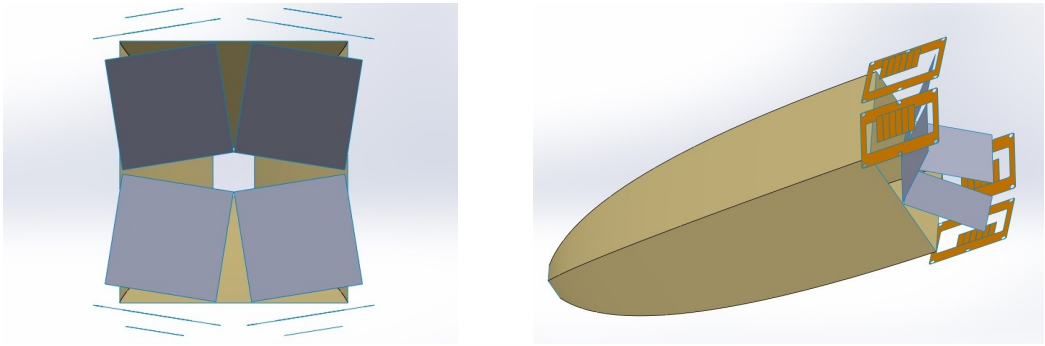

(a) (b)

Figure 3.9. Design concept #3 for CPC with orthogonal (a) and isometric (b) views. New mirrors are introduced as additional optical components. The mirrors and laser modules are arranged such that the area of the CPC entrance aperture is minimized.

Design 4 (Fig. 3.10) is likely to transmit more of the emitted light because the octagonal shape more closely approximates a circle. However, the output irradiance for a given concentration ratio is likely to be lower than that of Design 3 due to more unused area in the entrance aperture.

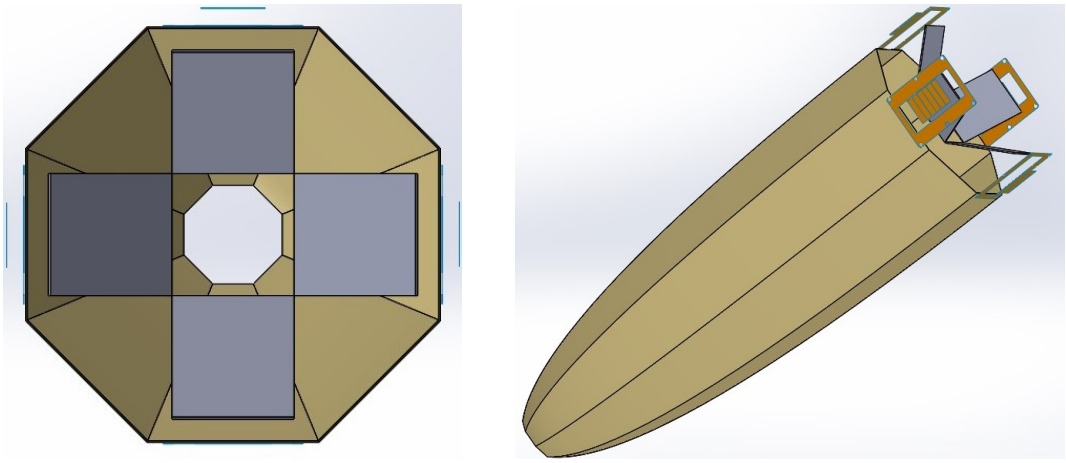

(a) (b)

Figure 3.10. Design concept #4 for CPC with orthogonal (a) and isometric (b) views. This octagonal shape results in a large entrance aperture area.

Each laser module has a corresponding rectangular CPC in Design 5, utilizing the entire entrance aperture. However, there are more losses at the exit aperture, due to conservation of étendue as described in Section 3.1. Two variations of this design

were simulated: those where the central axes of the CPCs aligned at the center point on the target surface (Fig. 3.11), and those where the axes were offset from the center to decrease the tilt angle of each CPC (Fig. 3.12).

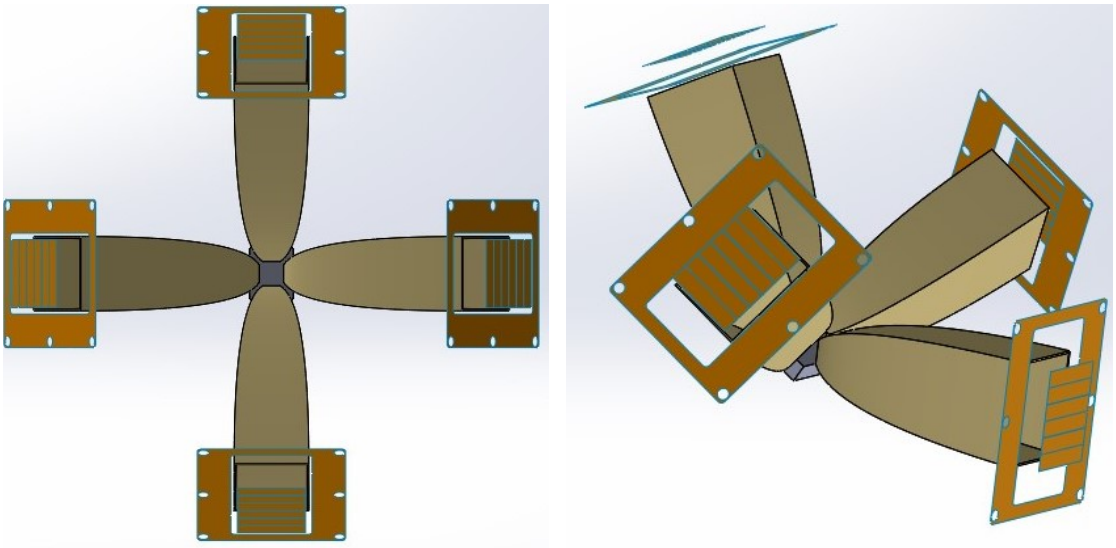

(a) **(b)**

Figure 3.11. Design concept #5a for CPC with orthogonal (a) and isometric (b) views. This concept uses a CPC for each laser module, and the central axis of each CPC is alinged at the center of the target.

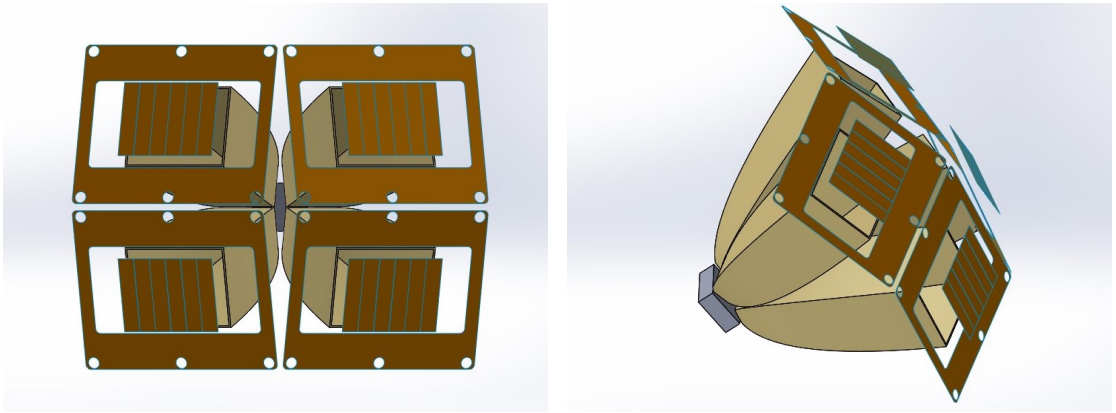

(a) **(b)**

Figure 3.12. Design concept #5b for CPC with orthogonal (a) and isometric (b) views. This concept uses a CPC for each laser module, and the central axis of each CPC is offset from the center of the target.

Initial simulations with Design 1 were performed to determine how the distance be-

tween the target and CPC (receiver to optic) (d_{RO}) affects the irradiance distribution (Fig. 3.13). The CPC has a concentration ratio of 30 for all studies, and the surface area and aspect ratio of the target surface is constant and equal to that of the CPC exit aperture. It is of utmost importance that the target surface is heated evenly to approximate conditions for a tokamak divertor. The standard deviation of irradiance (I_{std}) rises and η_τ falls roughly linearly with d_{RO}. Therefore, performance is optimized by bringing the target as close as possible to the CPC exit aperture. However, the CPC and target should not touch, as this would lead to conductive heat transfer between the two which would 1) be impossible to predict using ray-tracing software, 2) may overheat the CPC, and 3) would make it difficult to model the stress field in the target as the CPC itself would act as an additional mechanical constraint. Therefore, a target distance of 0.5 mm was chosen and used for subsequent studies.

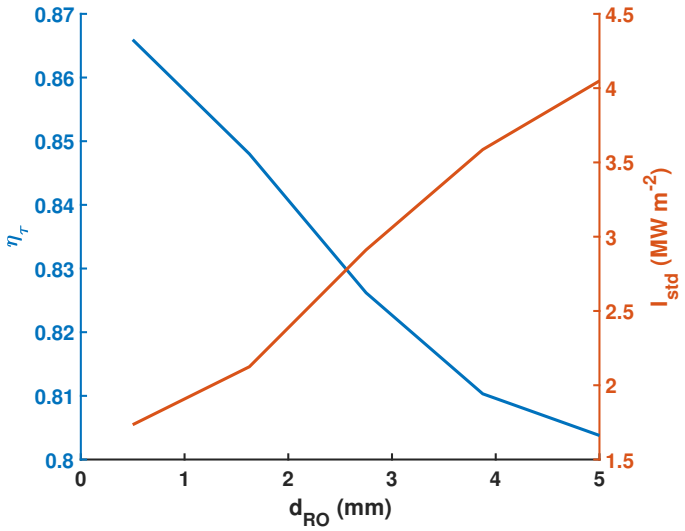

Figure 3.13. Variation of I_{std} and η_τ with d_{RO}. In this study, the concentration ratio was held constant at $C = 30$.

Studies were performed to determine the most effective design 1-5. Table 3.1 outlines the results and Fig. 3.14 shows the irradiance distributions. I_{avg} and I_{std} are the average and standard deviation, respectively, of the irradiance on the target surface.

Table 3.1. Results of ray tracing analysis in LightTools. All concentrators have concentration ratio $C = 30$ (which corresponds to $\theta_{acc} = 10.5°$) and $d_{RO} = 0.5$ mm.

Design #	CPC Height (mm)	I_{avg} $\left(\frac{\mathbf{MW}}{\mathbf{m^2}}\right)$	I_{std} $\left(\frac{\mathbf{MW}}{\mathbf{m^2}}\right)$	η_τ (%)
1	583	7.71	1.73	86.6
2	515	5.05	1.36	54.0
3	560	8.16	2.45	87.6
4	751	2.96	1.36	97.5
5, centered	133	8.45	2.15	42.5
5, offset	133	8.04	3.77	58.3

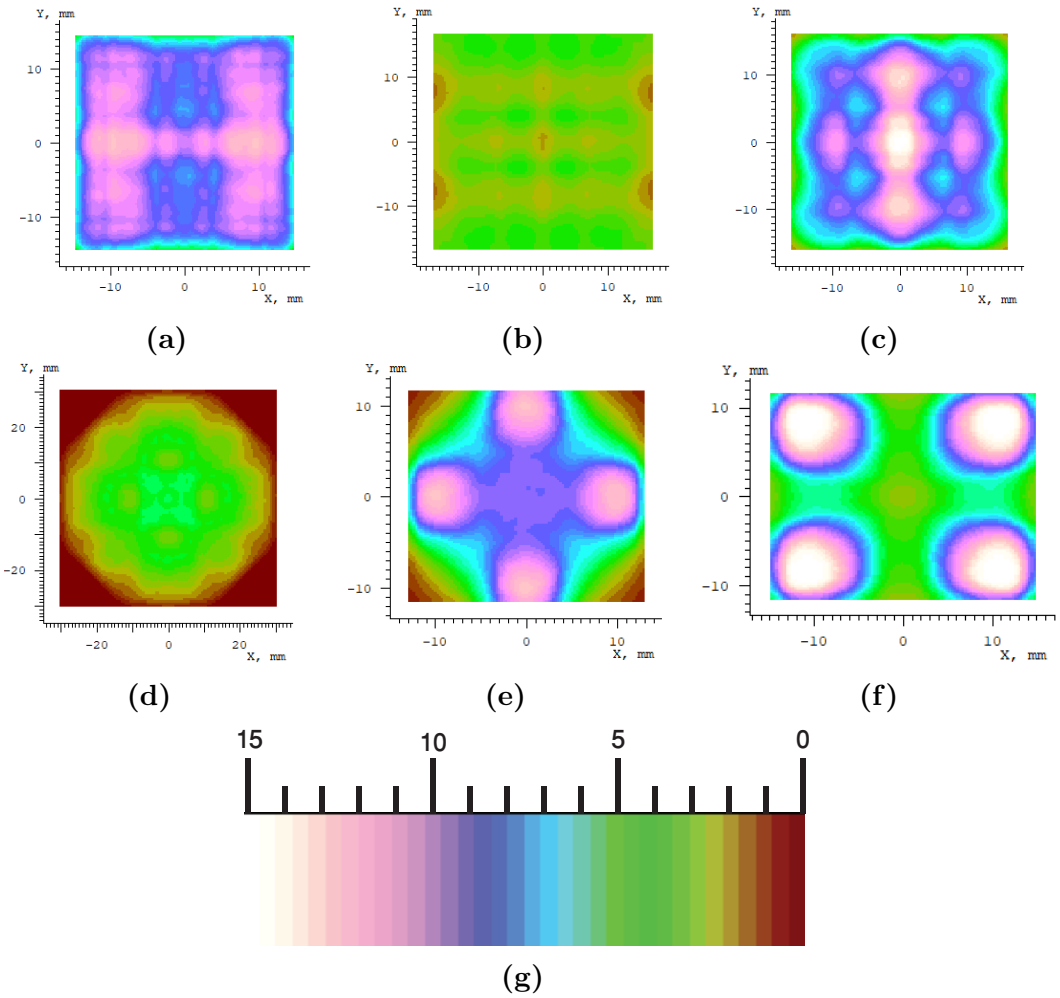

Figure 3.14. Irradiance patterns for design 1 (a), 2 (b), 3 (c), 4 (d), 5 centered (e), 5 offset (f), and a color bar in $\frac{\mathrm{MW}}{\mathrm{m^2}}$ (g). All concentrators have concentration ratio $C = 30$ (which corresponds to $\theta_{acc} = 10.5°$) and $d_{RO} = 0.5$ mm.

One of the most important considerations is how evenly the target surface is heated.

Design 1 delivers an average irradiance that surpasses the 5 $\frac{\text{MW}}{\text{m}^2}$ requirement while maintaining relatively low standard deviation and high transmission efficiency. The other designs either have too low a transmission efficiency, too high I_{std}, or too low I_{avg}. There will inevitably be some losses associated with non-ideal reflective surfaces and the target not absorbing 100% of the laser power. Yet, the results from Design 1 offer the simplest solution that can still meet operating requirements and allow for non-ideal losses in the actual device.

3.3 VCSEL Module Bracket

A simple sheet-metal bracket was designed which locates the four modules relative to each other (Fig. 3.15). The bottom of this bracket can be polished to a mirror surface finish, which will reflect some rejected rays, thereby increasing the transmission efficiency.

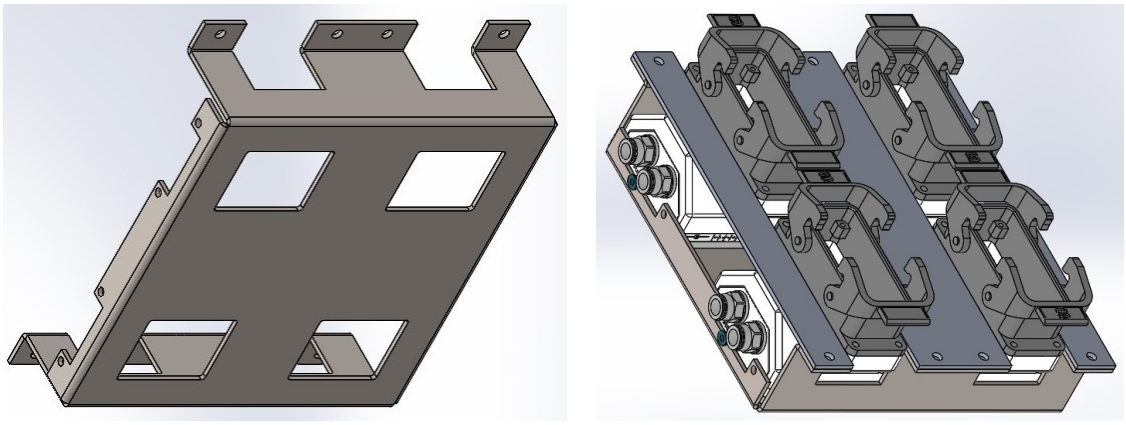

(a) **(b)**

Figure 3.15. Design of sheet metal bracket to locate the VCSEL modules relative to each other. The surface facing the reader in (a) will be brought to a mirror finish. The modules are bolted into the side of the bracket and held in place with cross braces (b)

Thus, a new LightTools study using Design 1 as a basis with a reflective bracket was executed to determine the effect of a changing concentration ratio on performance (Table 3.2). As predicted, the inclusion of the reflective bracket does increase η_τ

slightly. However, η_τ decreases as C increases because θ_{acc} falls below the divergence half-angle of 10°. A CPC with a concentration ratio of 32.5 yields a 2% higher I_{avg} but only 1.3% drop in η_τ when compared to a design with $C = 30$. More significantly, the outlet area drops below 10 cm^2 for a concentration ratio greater than 32.5. Thus, a CPC with $C = 32.5$ was chosen as the final design.

Table 3.2. LightTools study on how the concentration ratio affects the performance of design #1. Study includes a reflective mounting bracket and d_{RO} is set to 0.5 mm.

C	θ_{acc} (°)	A_{out} (cm^2)	I_{avg} $\left(\frac{MW}{m^2}\right)$	I_{std} $\left(\frac{MW}{m^2}\right)$	η_τ (%)
30 (no bracket)	10.5	11.9	7.71	1.73	86.6
30	10.5	11.9	8.07	1.71	90.9
32.5	10.1	10.1	8.23	1.66	89.6
35	9.7	8.71	8.68	1.62	87.7
37.5	9.4	7.59	9.07	1.57	85.6
40	9.1	6.67	9.43	1.50	83.4

3.4 Manufacturing

A variety of manufacturing techniques were considered. The advantages and drawbacks of each are shown in Table 3.3.

Table 3.3. Comparison of different manufacturing techniques considered for the CPC

Technique	**Advantages**	**Disadvantages**
3D Printing	Quick/easy to manufacture Suitable for complex shapes	Large part, expensive High interior surface roughness Difficult to apply coatings/polish Can only print certain materials
Traditional Manufacturing (Welding)	Cheaper production Good surface finish	Requires subdivision into parts Longer lead times Permanent joints
Traditional Manufacturing (Bolting)	Cheaper production Good surface finish Can disassemble	Requires subdivision into parts Longer lead times

Two of these three options were considered viable: 3D printing and traditional manufacturing (bolting). Although it is possible to print the entire CPC with metal

powder, this method was considered cost-prohibitive. On the other hand, the CPC could be printed in plastic filament, and then the inside lined with reflective, metal foil tape. This option provides customization to choose the reflective metal. This kind of manufacturing process is cheap and prototypes can be used for initial optical validation. However, this method is not suited for testing at full power, because the plastic material would likely not survive the high heat flux from the lasers.

The internal surface finish and project budgeting were critical factors that led to the decision to use traditional manufacturing over additive processes. Furthermore, it was desirable to have the ability to disassemble the CPC to ease the cleaning of those internal reflective surfaces. The CPC was then split into 8 pieces that bolt together. To ensure proper alignment, lap joints connect parallel surfaces, and precision dowel holes connect perpendicular surfaces (Fig. 3.16). The first iteration is machined from HE30 aluminum, which offers relatively high strength and corrosion resistance. After machining, the internal surfaces were polished to a mirror finish, thus satisfying the Rayleigh criterion (Eq. (2.9)) and achieving an optically smooth surface. There is relatively little data on the reflectivity of pure aluminum surfaces, but Edmund Optics suggests that the reflectivity of a mirror-like aluminum coating in the IR range is >90% [71] at 0° incidence angle.

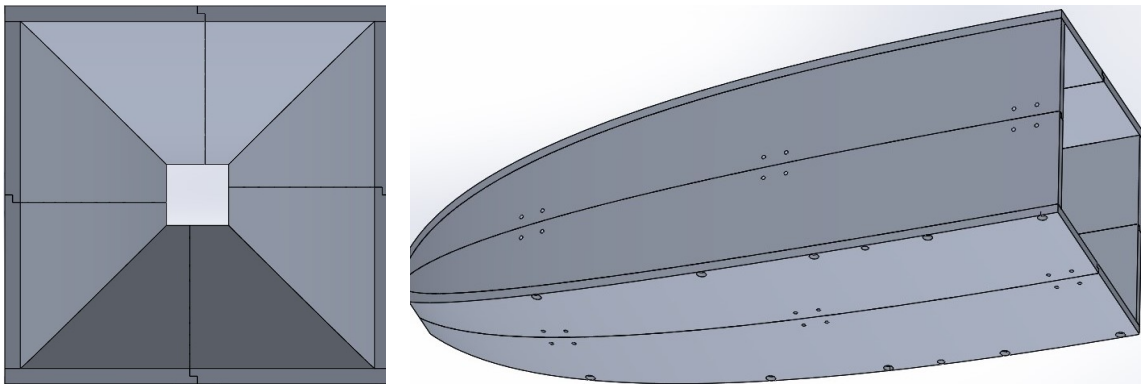

(a) **(b)**

Figure 3.16. The CPC must be split into several components. Orthogonal view (a) demonstrates the lap joints and (b) displays the bolt pattern and alignment holes for dowel pins

Chapter 4

Target Interface

4.1 Material Selection

A divertor target consists of an armor that shields against erosion from charged particles and a heat sink material. The armor must be able to withstand high temperatures and neutron bombardment, while the heat sink material must be able to withstand the coolant pressures and have a high thermal conductivity to transfer power effectively.

Tungsten was chosen as the armor of choice because it is a refractory metal with a melting temperature of 3,422 °C, presents very good mechanical properties at high temperatures, and has low permanent hydrogen retention at operating temperatures (meaning that the armor will not absorb tritium fuel) [81]. There are several drawbacks that come with W tiles, such as the formation of hydrogen bubbles and effects like blistering, which decrease not only the thermal conductivity but also the material strength. Moreover, pure tungsten has a high Ductile-to-Brittle Transition Temperature (DBTT), around 700 °C, which is unsuitable for structural applications, but since it is merely being used as an armor and the stresses are not very high, it can be used for fusion applications. Moreover, some alloys and thermomechanical techniques have been able to reduce the DBTT to 125 °C [82]. Despite its deficiencies, tungsten proves to be the most common armor material in target design.

CuCrZr was selected as the heat sink material based on its high thermal conductivity

and mechanical properties. Copper alloys are typically used as the divertor heat sink material [83]. This particular alloy, which is sometimes known as CuCrZr-IG (ITER Grade), has a higher modulus of elasticity for slightly lower thermal conductivity. The operating temperature range for this alloy (150 °C to 350 °C) is bounded by neutron-driven embrittlement on the low end and softening due to creep on the upper-end [84, 85].

4.2 Optical Target Interface

4.2.1 Surface Absorption

The target-laser interface is of critical importance, with the goal of absorbing as much of the incident power as possible. Fresnel derived the reflection and transmission coefficients for both electric field and power, but this work only refers to the coefficients as they relate to power transmission. The reflection coefficient describes the ratio of reflected to incident power, with similar logic for the transmission coefficient. The formula used for the reflection coefficient depends on the polarization of the light. Light can either be p-polarized (where the electric field is parallel to the plane of incidence), s-polarized (where the electric field is perpendicular), or a combination of the two.

VCSEL modules do not control the polarization of the emitted light, and therefore both modes are present [86]. The total reflection coefficient, R_{ps}, is the average of its p- and s-polarized components.

$$R_{ps} = \frac{R_p + R_s}{2} \tag{4.1}$$

Where R_p and R_s are defined below. Eqs. (4.2) and (4.3) are a part of the Fresnel equations and were derived as a combination of Snell's law, the law of reflection, and conservation of energy. These equations assume that the materials are non-magnetic and only apply at the interface (i.e. do not account for attenuation away from the

interface).

$$R_p = \left| \frac{n_1 \sqrt{1 - \left(\frac{n_1}{n_2} \sin\theta_i\right)^2} - n_2 \cos\theta_i}{n_1 \sqrt{1 - \left(\frac{n_1}{n_2} \sin\theta_i\right)^2} + n_2 \cos\theta_i} \right|^2 \tag{4.2}$$

$$R_s = \left| \frac{n_1 \cos\theta_i - n_2 \sqrt{1 - \left(\frac{n_1}{n_2} \sin\theta_i\right)^2}}{n_1 \cos\theta_i + n_2 \sqrt{1 - \left(\frac{n_1}{n_2} \sin\theta_i\right)^2}} \right|^2 \tag{4.3}$$

The angle of incidence, θ_i, is from the normal, and n_1 and n_2 are the indices of refraction for air and the target interface, respectively.

The transmission coefficient, which is the percentage of power that passes through an interface, can be found via conservation of energy:

$$T_{ps} = 1 - R_{ps} \tag{4.4}$$

Ray-tracing 10,000 rays in LightTools provided the θ_i for all rays hitting the target surface. The reference case for the best design (Chapter 3) was used (Design #1, $C = 32.5$, and $d_{RO} = 0.5$ mm). The simulation was downsized from 10^7 rays to avoid large text files for post-processing, while maintaining good representation of the spatial distribution. The discrete distribution of incident angles shown in Fig. 4.1 has an average value of 45.1°, median value of 46.5°, and standard deviation of 19.6°. Fig. 4.2 shows a qualitative version of Fig. 4.1. There are very few rays with θ_i close to either 0°or 90°.

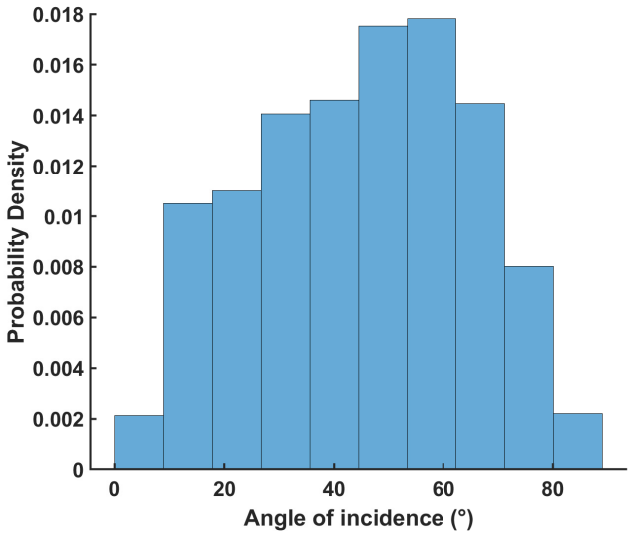

Figure 4.1. Histogram of angle of incidence on target from LightTools ray tracing of 10,000 rays. The histogram is normalized by probability density. This study was performed for the reference case of design #1 with $C = 32.5$ and $d_{RO} = 0.5$ mm.

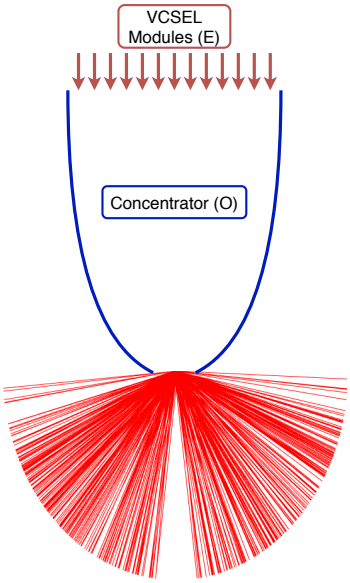

Figure 4.2. Visual representation of how the angle of incidence varies. Qualitatively, there are relatively few rays at both low incidence angles (close to 0°) and high incidence angles (close to 90°).

The power of all rays across the four modules ($\dot{Q} = 9600$ W) is evenly distributed amongst those simulated. For N rays, each one therefore carries $\frac{\dot{Q}}{N}$ W. The differential

power absorbed by the receiver from an individual ray can be written as:

$$\delta\dot{Q}_\alpha = \frac{\dot{Q}}{N} T_{ps} \tag{4.5}$$

Where T_{ps} is a function of each ray, depending on its angle of incidence. The total power absorbed by all rays, $\dot{Q}_\alpha$, is the incident power times the average transmission coefficient:

$$\dot{Q}_\alpha = \dot{Q}_i \frac{\sum T_{ps}}{N} = \dot{Q} T_{ps,avg} \tag{4.6}$$

Based on initial visual inspection of the spatial map (Fig. 4.3a), it was assumed that there are no areas where a certain incidence angle is dominant. If, for instance, θ_i in a certain quadrant was large compared to the other quadrants, this area would be a 'cold' spot because T_{ps} decreases for large θ_i. In order to validate this assumption, the spatial distribution of the angles was filtered into a 4x4 grid (Fig. 4.3b), and each grid was compared against the rest. The maximum average difference between any two boxes on the grid was 8.6%, which corresponds to a difference of only 4°; thus, the assumption that there are neither 'cold' nor 'hot' transmission spots is valid.

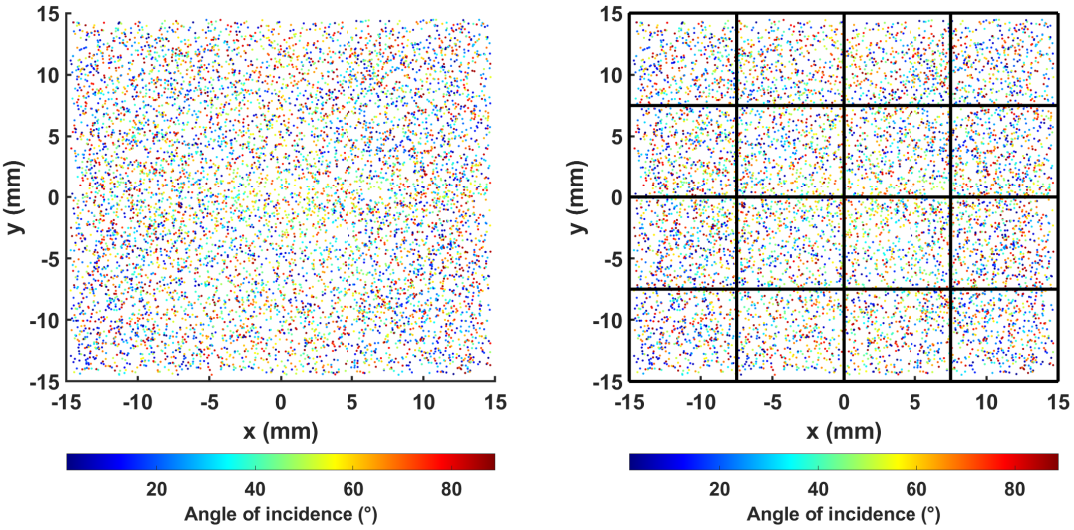

(a) **(b)**

Figure 4.3. Spatial distribution of incidence angle on the target. Figure (a) was subdivided into 16 even portions in (b) to test whether there were any 'hot' or 'cold' spots.

4.2.2 Optical Coating

The value of n_1 for air of 1.0003 comes from [87] . Because the target is a solid, the value for n_2 will inherently be complex such that $n_2 = n + ik$. The imaginary part of the refractive index, k, is known as the extinction coefficient.

Metals typically have low indices of refraction and high extinction coefficients, which leads to their having highly reflective (and thus poorly transmitting) surfaces. For experimental tests aiming to achieve maximal power absorption, it is therefore important that some kind of anti-reflective coating or blackening treatment be applied to the target surface.

Fig. 4.4 demonstrates how the average transmission coefficient changes for different values of n_2. If $n_1 = n_2$, the transmission is always 100%. However, as either the extinction coefficient or real index of refraction rises, the transmission decreases. A coating with a refractive index close to n_1 and a low extinction coefficient would produce the highest transmission.

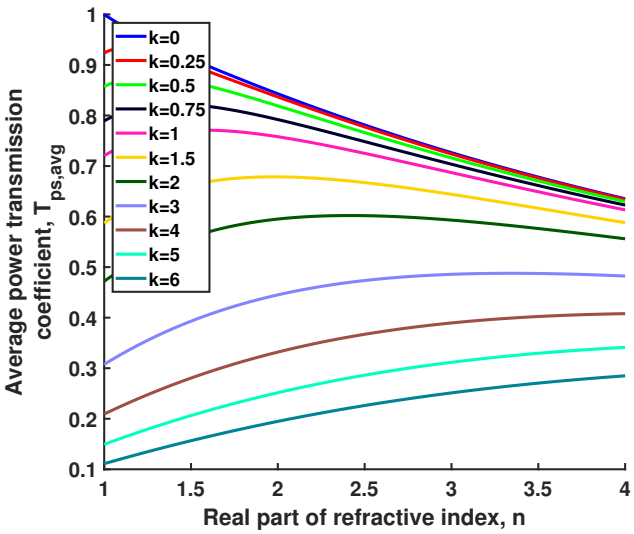

Figure 4.4. Effect of complex index of refraction, n_2, on the average transmission coefficient. The real part for n_2 is almost always greater than 1 for solids because of their high density.

Another useful property to determine the optical performance of a coating is total hemispherical emissivity (or the total hemispherical reflectance, which is simply the complement). Whereas emissivity is actually directional, the hemispherical emissivity is the weighted average over all incident rays at a given wavelength and temperature. Typically, values for emissivity are given as this total hemispherical, as this is an important measure of how much radiation a coating will absorb.

In addition to optical properties, there are a few other functional requirements for the target coating. The target test piece consists of the CuCrZr heat sink without the use of tungsten armor. So at maximum power, it is therefore assumed that the coating will reach the creep limit for CuCrZr (350 °C) at maximum power.

Additionally, the coating must be thin enough such that there is negligible temperature distribution in the normal direction because an IR camera is used to remotely sense temperature at the target surface.

Another important property of a coating is its outgassing rate. If the coating releases trapped gases at high temperature operation, those gases could condense onto

the VCSEL modules. In turn, the condensate would absorb laser energy and heat up, posing a risk to overheating the module. The industry standard for outgassing measurements is maximum collected volatile condensable material (CVCM) [88], and should be less than 0.1% according to [89].

Several options for an anti-reflective coating were considered, and the relevant data for each is reviewed (Table 4.1). The materials of each coating also give a relative scale of cost; for instance, while Multi-Walled Carbon Nanotubes (MWCNT) are typically expensive because the manufacturing and deposition process is labor intensive, black paints are less expensive.

Table 4.1. Comparison of anti-reflective coatings considered for high emissivity/absorption target. Results for hemispherical emissivity are at 980 nm, or the closest data point if information was not provided at that wavelength. Temperature data was not held constant for emissivity.

Coating	**Material**	ϵ (%)	**Thickness (µm)**	T_{max} (°C)	**Outgassing (CVCM %)**
Vantablack S-VIS [90]	MWCNT	99.8	200	300	<0.1
Acktar Magic Black™ [91]	Inorganic	99.1	3-5	380	0.001
Acktar Fractal Black™ [91]	Inorganic	98	5-14	380	0.001
Singularity™ Black [92]	Nanotube solvent-based paint	98.8	-	450	0.04
Rolls-Royce HE6 [93]	Proprietary paint	95	-	1300	-
Rolls-Royce HE23 [93]	Proprietary paint	93	-	1300	-
Aremco 840-MS [94]	Silicone-ceramic paint	∼85	-	593	-

Vantablack S-VIS from Surrey Nanosystems was chosen as the optimal coating because of its extremely high emissivity, though Singularity™ Black is another good option that may be cheaper. This coating is made of MWCNT and meets all the

previous criteria. At 980 nm, its refractive index is 1.05 and its total hemispherical emissivity 99.8% [90]. Although Surrey Nanosystems does not provide data for the extinction coefficient, [95] has developed a highly absorbent coating with similar characteristics and performance capabilities. Their multi-walled carbon nanotube coating has a fill factor of 1%, meaning that most of the volume of the coating is air. This low-density coating leads to an index of refraction close to unity, and it can thus be safely assumed that the extinction coefficient is 0.

The combination of the refractive index close to n_1 and low extinction coefficient lead to a high average transmission coefficient of 0.989, meaning that 98.9% of the incident laser power is absorbed by the target. Further, Vantablack S-VIS can survive steady-state temperatures up to 300 °C in air or 350 °C in an inert environment [90]. Given a maximum incident heat flux of 10 $\frac{\mathrm{MW}}{\mathrm{m}^2}$, a coating thickness of 200 µm [90], and an assumed thermal conductivity of ∼3000 $\frac{\mathrm{W}}{\mathrm{mK}}$ of multi-walled carbon nanotubes at 350 °C [96], the temperature variation across the thickness would be negligible (<1 °C).

Chapter 5

Thermomechanical Performance

5.1 Problem Definition

There were two main concerns regarding the steady-state, thermomechanical performance of the target, CPC, and VCSEL modules. First, the borosilicate glass in the VCSEL modules must not reach temperatures greater than 70 °C [97]. Second, the thermal gradient in the CPC must not induce strain such that its max displacement, δ_{max} is greater than the machining tolerance of 0.5 mm.

The thermal boundary conditions are as follows:

- As described in Section 4.2.2, the target surface will reach a max temperature of 350 °C during steady-state operation. This high temperature will produce a significant amount of radiation.
- The CPC itself will absorb some of the incident power from the VCSEL modules, but then radiate that off. Under steady-state conditions, the amount absorbed and radiated is equal.
- Some kind of active cooling may be needed: fans, for example, that cool down the outside of the CPC.

Assuming the target surface will be heated to 350 °C [85], there will be a significant amount of radiation coming from the target back to the CPC and glass. Planck's

Law describes radiation from a black body Eq. (5.1).

$$H(\lambda, T) = \frac{2h\lambda^2}{c^2} \frac{1}{e^{\frac{h\lambda}{(kT)}} - 1} \tag{5.1}$$

Where the spectral power density (intensity) H, the power per solid angle per area per frequency, is a function of the body temperature T and the frequency of radiation λ. The universal constants, h, c, and k are Planck's constant, the speed of light, and the Boltzmann constant, respectively. Assuming the radiation projects from a flat surface to a hemisphere in space, and that the radiation is lambertian, one can derive the Stefan-Boltzmann equation from Plank's Law:

$$j = \sigma(T^4 - T_0^4) \tag{5.2}$$

Where j is the power per unit area from the surface, σ is the Stefan-Boltzmann constant, T_0 is the ambient temperature, and both T and T_0 are calculated in absolute units. Assuming a surface temperature of 350 °C and ambient temperature of 25 °C, $j = 8,100 \ \frac{\mathrm{W}}{\mathrm{m}^2}$. This translates to approximately 8.1 W of radiating heat from the target surface.

In steady-state, the absorption coefficient α and the emissivity ϵ are equal [98]. At full power, it was assumed that 9600 W are incident and evenly distributed on the inner surface of the CPC, but only a portion of that is absorbed. The emissivity (and thus absorption coefficient) was found in [99] to be 0.04-0.06 for highly polished aluminum for temperatures between 50-500 °C. A max value of 576 W may significantly heat the CPC, and it may be necessary to provide active cooling. As described in Section 4.2.2, the absorption coefficient and thus emissivity of the target is 0.989. Finally, [100] provides the emissivity of borosilicate glass at ∼2 mm thickness as 0.79.

Forced convection coefficients for air typically range from 10 to 1000 $\frac{W}{m^2K}$ in various conditions [101]; air-cooled desktop fans can achieve coefficients between 50-150 $\frac{W}{m^2K}$

[102]. A numerical study in Section 5.2 investigated varying levels of air-cooling.

Fins were added to the sides of the CPC and a flange to the bottom (Fig. 5.1). The final design of these cooling elements was an iterative process, including consultation with the machine shop at OTI. It was necessary to have a flat surface along nearly the entire length of the CPC against which the work holding could register. Thus, the fins facilitated a simpler machining setup in addition to providing more effective cooling. The 8 mm thickness of the fins and flange were recommended to not produce significant chatter while machining. Finally, the bottom of the flange will be polished to a mirror finish as well, which will help reflect the radiative heat emitted by the target surface.

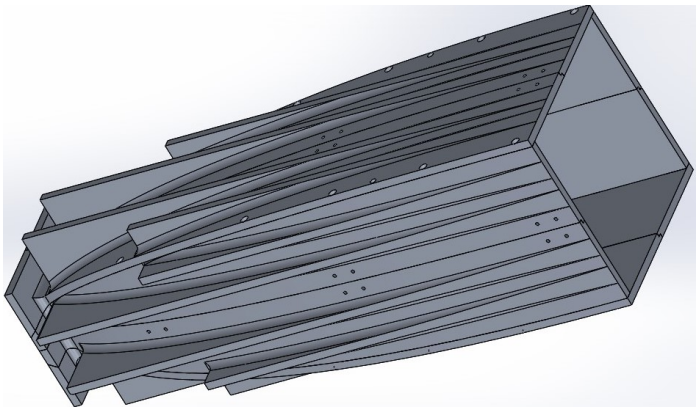

Figure 5.1. Addition of fins to CPC to allow for manufacturing on a three-axis mill and to facilitate better convective heat removal.

5.2 Numerical Study

Before finalizing the design, a thermal analysis was performed in ANSYS Mechanical to ensure that neither the CPC nor the VCSEL modules would overheat during steady-state operation. A multiphysics simulation including surface-to-surface radiation, conductive, and convective heat transfer in solids provides a measure for the thermal performance of the experimental design. Material properties for aluminum and copper alloys from the ANSYS general material library, and borosilicate glass from [103] were applied to the CPC, target, and glass, respectively. Quarter-symmetry

was applied as detailed in Fig. 5.2. The boundary conditions are summarized:

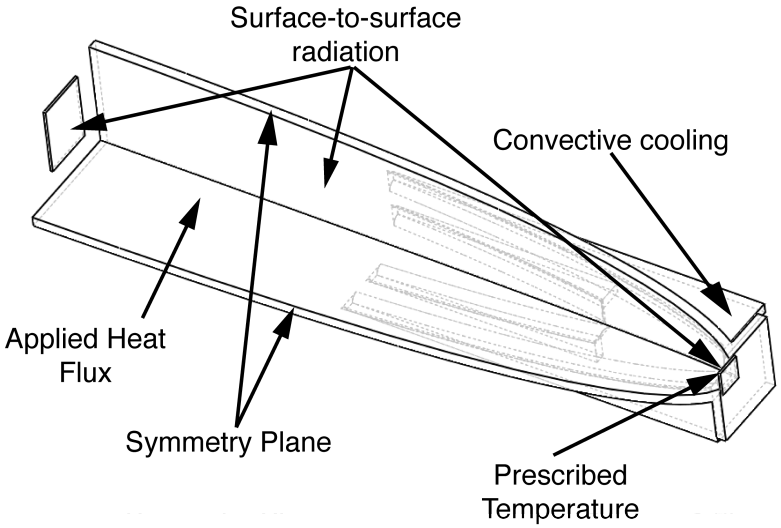

Figure 5.2. Quarter-symmetric geometry used in ANSYS Mechanical. The geometry includes the glass from one laser module, one-quarter of the CPC, one-quarter of the receiver, and is simplified to facilitate the meshing and numerical processes. Boundary conditions include an applied heat load on the CPC inner surface, surface-to-surface radiation, convective cooling coefficient applied to the outer surface of the CPC, and a prescribed temperature of the target.

A static structural simulation provided the total displacement field of the CPC, using the thermal simulation as a loading condition. The glass and receiver were completely fixed, as their displacement was not relevant to the study. The CPC was fixed at three points on one side of the fins to prevent translation and rotation of the whole body but allow for thermal expansion.

A tetrahedral, unstructured mesh was used to capture the geometry. A mesh sensitivity study was performed before selecting a reference mesh for a parametric study. Convergence criteria were based on the program-controlled options in ANSYS Mechanical.

5.2.1 Mesh Sensitivity

A reference case with the boundary conditions in Table 5.1 was used to determine mesh sensitivity. ANSYS Mechanical calculates the radiation view factors automat-

ically via the hemicube method [104, 105]. The results from a coarse and fine mesh are outlined in Table 5.2.

Table 5.1. Boundary loads for thermomechanical study in ANSYS. Reference case to test for mesh independence.

Convective heat transfer ($\frac{W}{m^2K}$)	Incident power (W)	ϵ (CPC)	ϵ (Receiver)	ϵ (Glass)	Receiver Temp. (°C)
50	144	0.06	0.989	0.79	350

Table 5.2. Results from mesh sensitivity study for the thermomechanical performance of the CPC. There is very little difference between the coarse mesh and the fine mesh, with the largest being in the deformation. A 3.3% difference between meshes was not deemed significant, as this corresponds to a displacement ∼0.01 mm on a ∼600 mm component.

Result	# Elements	Min. CPC Temp. (°C)	Max CPC Temp. (°C)	Max Glass Temp. (°C)	δ_{max} (mm)
Coarse	41,000	37.93	52.26	28.93	0.377
Fine	290,000	37.93	52.26	28.81	0.365
% Difference	-	0	0	0.4	3.3

Mesh independence was assumed when the results differed less than 5% between meshes. Results from the coarse mesh satisfy these criteria, and this was the mesh used in the parametric study outlined in Section 5.2.2 (Fig. 5.3). The element size was doubled from the coarse mesh to the fine, resulting in the largest percentage difference being in the max deformation (3.3%). This was deemed negligible because it corresponds to a displacement of only ∼0.01 mm, which is significantly less than the ∼600 mm height of the CPC.

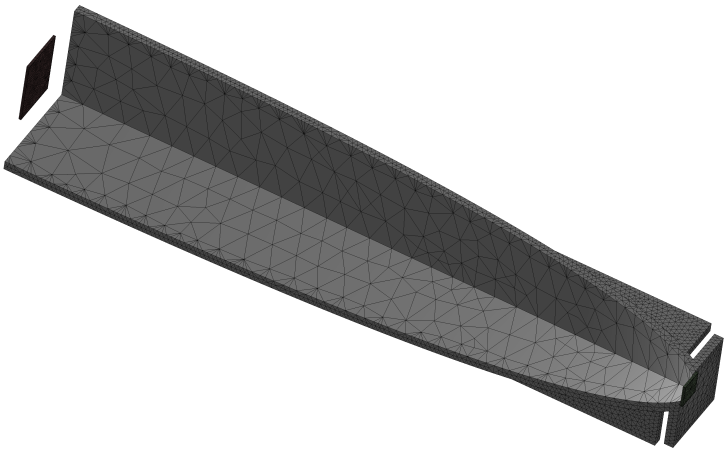

Figure 5.3. Coarse mesh used in ANSYS Mechanical study. This mesh produced results which were deemed independent of any further refinement.

Results from the thermomechanical study show that the temperature of the borosilicate glass does not exceed the critical limit of 70 °C (Fig. 5.4). Furthermore, the temperature gradient is less than 1 °C over the 24 cm^2 area, meaning that the heating is fairly evenly distributed and would not lead to large thermal stresses.

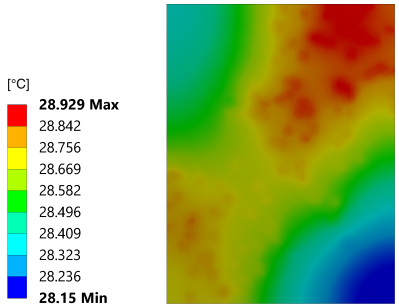

Figure 5.4. Contour plot of temperature on the surface of the borosilicate glass. The simulation demonstrates that the glass will not exceed temperatures of 70 °C during steady-state operation.

Furthermore, the numerical study provides evidence that the thermal deformation does not exceed the machining tolerance of 0.5 mm Fig. 5.5. The deformation is largest at the entrance of the CPC and smallest at the exit because the temperature

is highest at the entrance (52.2 °C) and lowest at the exit (37.9 °C).

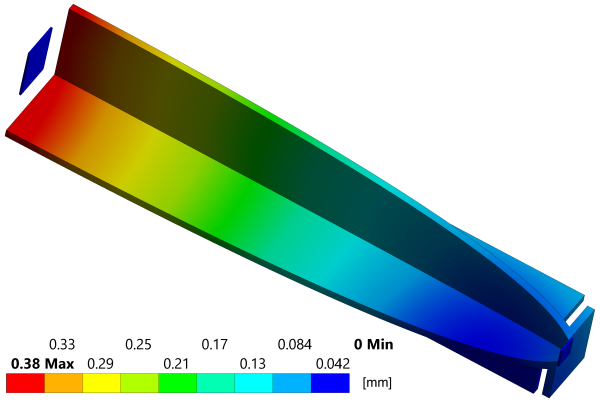

Figure 5.5. Contour plot of displacement due to thermal deformation. Results indicate that the maximum displacement does not exceed 0.5 mm, meeting requirements.

Thus, both functional requirements have been met via the thermomechanical numerical study. A parametric study was then performed to understand the behavior under a variety of operating conditions.

5.2.2 Parametric Study

Having determined an appropriate mesh, a parametric study was performed on several variables. The 350 °C prescribed temperature on the receiver is given by the maximum temperature of the heat sink material (Section 4.1). However, if at some point the target is tested with tungsten armor in addition to the CuCrZr heat sink, the surface temperature may reach as high as 1,000 °C [106]. Additionally, the convective cooling rate may differ on the outer surface of the CPC, depending on the cooling method chosen.

Performance based on changes in prescribed receiver temperature (Fig. 5.6a) shows that the max deformation of the CPC is weakly dependent on this temperature, with only a ∼3% change from 350 °C to 1000 °C. However, the max glass temperature increases by 104% between the prescribed temperature range. Because the glass has a relatively high emissivity (0.79) compared to the polished aluminum CPC (0.06),

the heat it absorbs due to radiation will be significantly more depending on the temperature of the receiver.

Looking at the convective cooling rate (Fig. 5.6b) shows again that the max deformation of the CPC is not really affected by changes in receiver temperature. It does, however, show a greater than four times difference between cooling rates of 10 and 50 $\frac{\mathrm{W}}{\mathrm{m^2K}}$. Only at 40 $\frac{\mathrm{W}}{\mathrm{m^2K}}$ does the max displacement drop below the 0.5 mm requirement, regardless of temperature. The max glass temperature does show a temperature drop greater than 5 °C over the range of convective cooling rates, but it is more highly dependent on the target temperature. Regardless of temperature or cooling rates, the glass stayed below the requisite 70 °C limit.

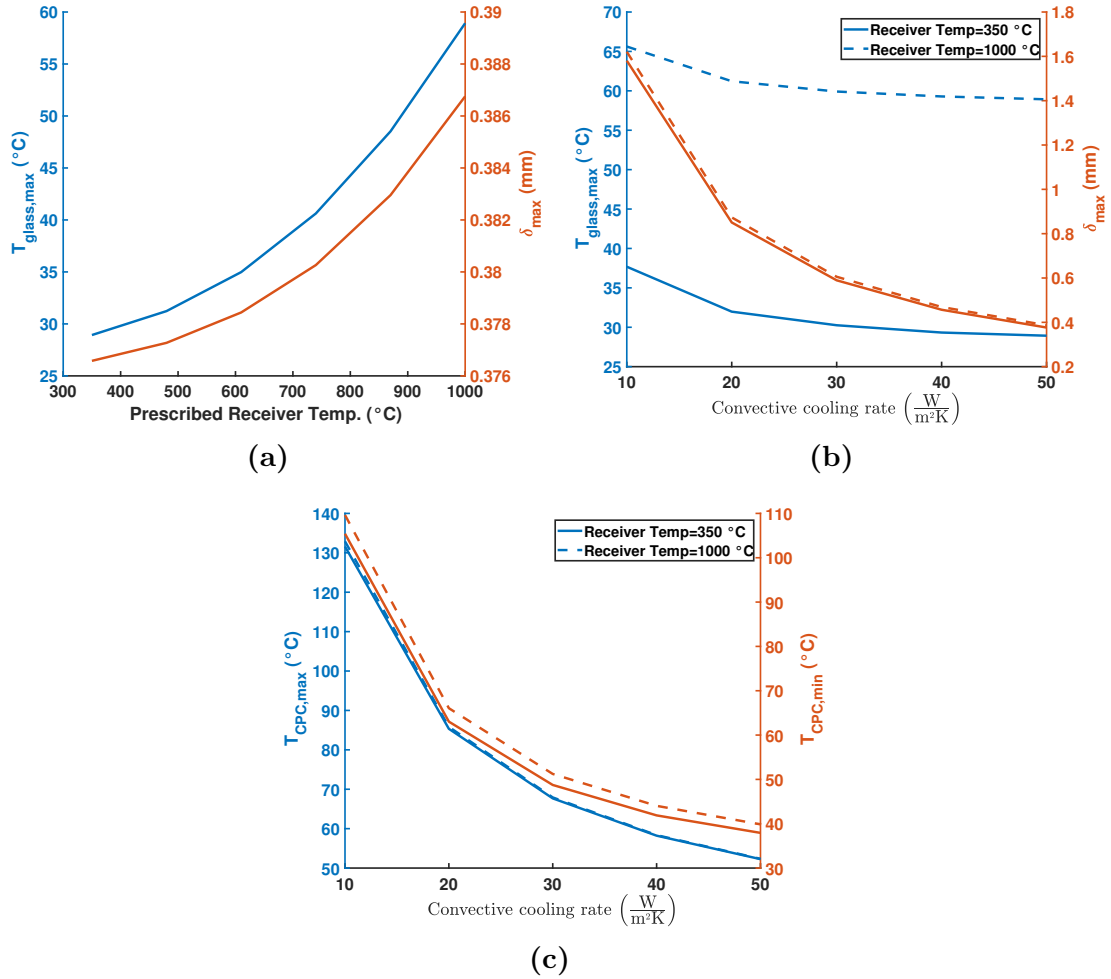

Figure 5.6. Parametric study results for thermomechanical performance of CPC. Only the prescribed receiver temperature and convective cooling rate are varied, while all other input parameters from Table 5.1 are constant. Subfigure (a) shows how the max glass temperature ($T_{glass,max}$) and max CPC deformation (δ_{max}) change with respect to prescribed target temperature. In this figure, the convective cooling rate is held constant at 50 $\frac{W}{m^2K}$. Subfigure (b) shows how those same two variables change depending on the convective cooling rate. Subfigure (c) demonstrates how the maximum and minimum CPC temperature change with the cooling rate.

Chapter 6

Novel Spiral Plate Module

6.1 Spiral Plate Heat Sink

This non-imaging optical system consists of the four VCSEL lasers (emitter E), concentrator(s) (optic O), and the test specimen (receiver/target R). While previous sections have discussed the emitter and optic, this section focuses on the target design.

Modular designs, like that of Nicholas et al. [55], offer several benefits over integrated designs such as the ITER-like W MB. Modularity allows for user-specified control of mass flow rates to different areas of the divertor. Because the heat flux can vary from an average $\sim$5 up to a peak of $\sim$20 $\frac{\mathrm{MW}}{\mathrm{m}^2}$, it is beneficial to control the mass flow rate to match the heat flux profile. The flow path is also significantly shorter for many modular designs, which means the bulk fluid will not heat up as much and typically offers more even heat transfer coefficients on its surface. There are some drawbacks associated with modularity, such as higher pressure drops and difficulty of manufacturing.

One of the negatives of impinging jets is the pressure drop associated with the stagnation point. Yet, impinging jets offer some of the best heat transfer capabilities because of the thin boundary layer that forms upon impact. The author has designed a novel divertor target that aims to achieve high heat transfer coefficients – like those

of impinging jets – while maintaining a low pressure drop. This design is based on a concept for producing neutrons in a radiation-based cancer treatment known as Boron-Neutron Capture Therapy [107]. A swirling jet strikes the center of the HF surface at an oblique angle and is driven through a spiraling channel(s). The design aims to decrease pressure drop due to the stagnation point while keeping the overall heat transfer coefficient high. This new design was termed the Spiral Plate Module (SPM).

6.1.1 Flow in Curved Channels

The author's concept is heavily dependent on the behavior of flow in curved channels, which is typically quite different from that in equivalent straight channels. Curved channels have been used in a variety of applications for their increased heat transfer capabilities [108–112]. Flow through a curved channel generates centrifugal forces, which lead to a pressure gradient in the outward radial direction. This pressure gradient induces secondary flow, improving mixing and thus heat transfer. Dean first quantified the effect of this phenomenon and showed that heat transfer and pressure drop increase [113, 114]. It was demonstrated that the corresponding heat transfer coefficient and friction factor can be written as functions of the dimensionless Dean number, De, which was proposed in his honor [115]:

$$De = Re\sqrt{\frac{D_h}{2R_c}} \tag{6.1}$$

Where Re is the Reynolds number, D_h the hydraulic diameter, and R_c the radius of curvature. Another important parameter, which appears here, and often in correlations with the Dean number, is the curvature ratio, $\frac{D_h}{2R_c}$. The Reynolds number non-dimensionalizes the inertial and viscous forces in the fluid based on the fluid

density ρ_f, bulk velocity v_b, hydraulic diameter D_h, and dynamic viscosity μ.

$$Re = \frac{\rho_f V D_h}{\mu} \tag{6.2}$$

Another important parameter in channel flow is the Darcy-Weisbach friction factor, f, which is a dimensionless form of pressure drop due to friction, ΔP_{fric}:

$$\Delta P_{fric} = f \frac{L}{D_h} \frac{\rho_f v_b^2}{2} \tag{6.3}$$

Finally, the Nusselt number is a non-dimensional parameter that compares fluid conduction and convection. The Nusselt number is predicted by experimentally- and numerically-based correlations depending on geometry and flow characteristics. The heat transfer coefficient, h can then be determined because the hydraulic diameter and thermal conductivity of the fluid k_f are known.

$$Nu = \frac{h D_h}{k_f} \tag{6.4}$$

Boussinesq's theoretical analysis of laminar flow through a curved rectangular channel [116] demonstrated the formation of symmetrical vortices, which were confirmed by [113] and often called Dean vortices. These vortices lead to an increased velocity profile towards the outer wall of the channel (Fig. 6.1). Additionally, concurrent work in 1929 by Taylor and White observed that when turbulent flow from a straight section transitioned to a curved pipe, the flow became laminar [117, 118]. Somewhat surprisingly, the secondary flow provides a stabilizing effect, such that the critical Reynolds number can more than double before a transition to turbulence is observed [119], even though curvature produces additional forms of instability.

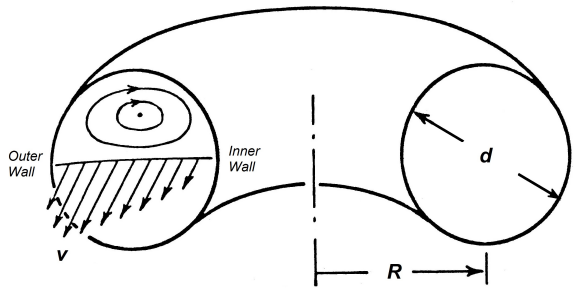

Figure 6.1. Dean flow is a phenomenon that occurs with fluid flow through curved pipes. A velocity gradient with a maximum near the outer wall of the pipe creates vortices within the channel. Typically, this secondary flow increases mixing, but also increases the critical Reynolds number to achieve turbulence when compared to an identical, straight pipe [120].

There has been much experimental and numerical investigation of Dean flow. An overview of correlations has recently been provided, including formulae for critical Reynolds numbers, heat transfer coefficients, and friction factors [121]. However, the majority of studies primarily concern laminar flow [119]. A recent summary of turbulent flow behavior in curved channels, including large-eddy/direct numerical simulations, has been able to validate experimental models of turbulent flows [119]. The flow structure is more complicated than flow in straight channels due to the added instabilities from centrifugal forces. Turbulent phenomena such as vortex shedding [122, 123] and several modes of instability [124], which are highly dependent on the curvature ratio $\frac{D_h}{2R_c}$, make it difficult to create generalized correlations for heat transfer and friction factors [121].

Studies on flow in spiral channels are limited. As the radius of curvature, and thus Dean number, is constantly changing, most of the work on spirals has employed some kind of spatial averaging. Ghobadi et al. impinge laminar flow on a constant-temperature spiral plate [125], and observed that heat transfer capabilities become more pronounced as the flow rate increases. They produced a 1D analytical model with spatially averaged Nusselt numbers to predict laminar flow, but the model produced a minimum of 25% error for water. Other studies use a spatially averaged radius of curvature [126, 127], but most studies used a spatially averaged Nusselt

number [128–131].

6.1.2 Conceptual Design

To establish a local reference frame for the geometry, a cylindrical coordinate system was defined such that θ_{sp}, r_{sp}, and z correspond to the streamwise, radial, and vertical directions, respectively. (Fig. 6.2).

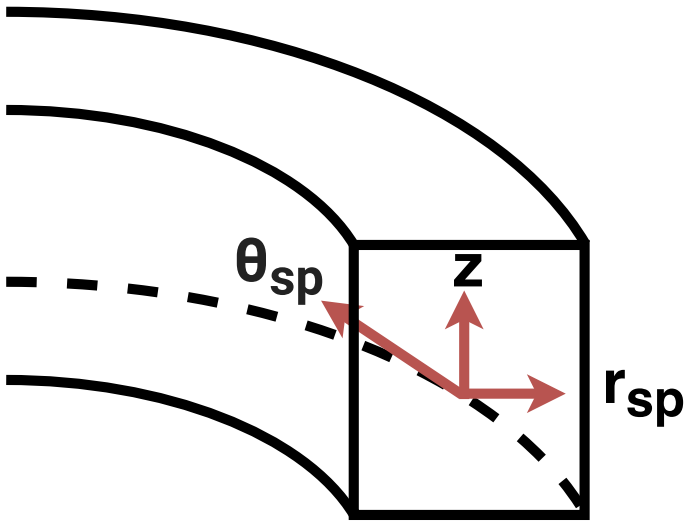

Figure 6.2. Local coordinate system defining flow in an arbitrary curved channel, where r_{sp} points in the radial direction outwards, z points upwards, and θ_{sp} points along the direction of the channel.

An Archimedean spiral can be defined by the polar equation Eq. (6.5), where a_{sp} can be viewed as a sizing factor. This type of spiral has the unique characteristic that the separation distance between successive turns is constant and equal to $2\pi a_{sp}$ if θ_{sp} is measured in radians (Fig. 6.3a). This trait allows for multiple spirals to be nested together with a constant distance between them (Fig. 6.3b).

$$r_{sp} = a_{sp}\theta_{sp} \tag{6.5}$$

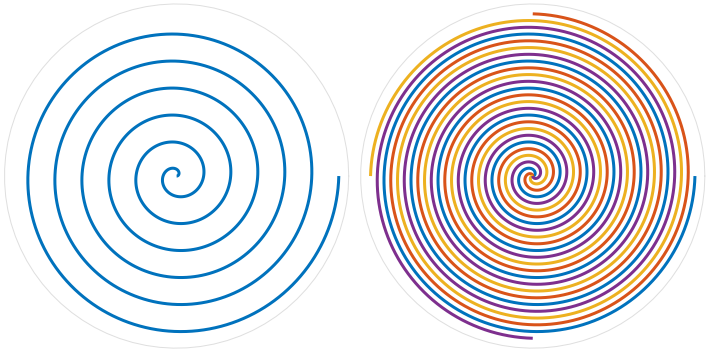

(a) **(b)**

Figure 6.3. An Archimedean spiral has the unique characteristic that the distance between consecutive turns is a constant (a). This property allows multiple spirals to be nested with constant spacing (b).

A Cartesian, parametric form of Eq. (6.5) is necessary for programmatic drawing computer design softwares (Eq. (6.6)).

$$\begin{cases} x_{sp} = a_{sp}\theta_{sp}\cos\theta_{sp} \\ y_{sp} = a_{sp}\theta_{sp}\sin\theta_{sp} \end{cases} \tag{6.6}$$

The geometry of the spiral features affects the heat transfer coefficient and pressure drop through the swirl plate. It was predicted that a decrease in a_{sp} would produce larger values for h due to a tighter bend radius and higher pressure drop because of the increased flow path length and friction factor. An increased number of nested spirals, denoted by n, requires thinner flow channels along the r-axis, and also allows for shorter flow paths; both changes would increase the overall heat transfer capability, but while the latter would increase pressure drop, the former would offset that drop to some degree. A MATLAB script, detailed in Section 6.2, was written to scrape the design space to compare geometries.

The general shape of the module was chosen to be a hexagon so that multiple can be packed together with no gaps. The design consists of four major components (Fig. 6.4): the target plate, swirl plate, backing, and housing. The critical portion of the design is contained in the spiral plate, as heat transfer and pressure drop can be

considered negligible elsewhere.

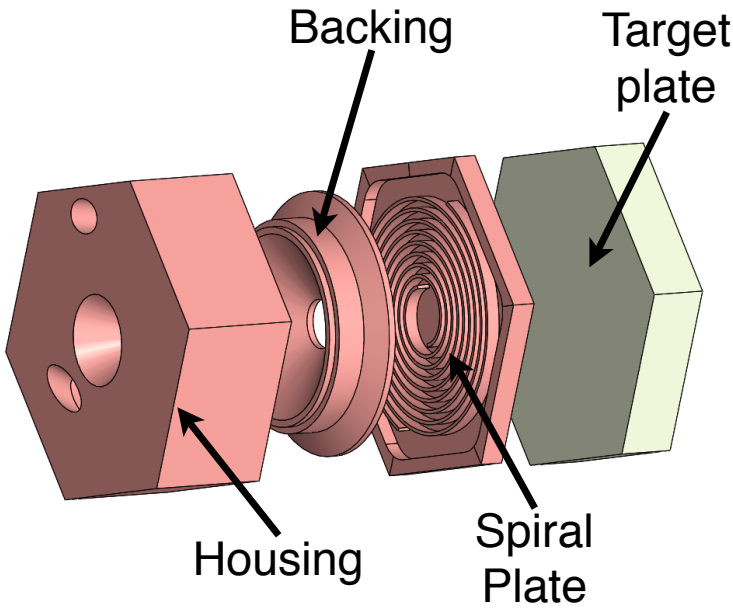

(a)

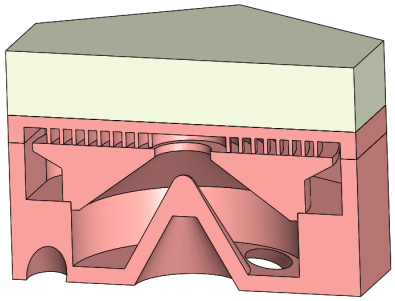

(b)

Figure 6.4. The geometry of an SPM consists of four components, as can be seen in an exploded view of the model (a). Subfigure (b) offers a cross-sectional view of the assembled geometry. Coolant enters through the inner portion of the housing, which spirals around into the spiral plate, at which point it is channeled outwards and exits through the outer portion of the housing. The inner and outer portion of the housing are separated by a backing plate. The target plate sits atop the spiral plate and acts as a neutron shield.

- **Target Plate**: The heat flux strikes the fully tungsten target plate. The target plate can withstand the high temperatures and neutron flux present during steady-state operation of DEMO.

- **Housing**: Coolant enters and exits through channels in the housing. The inlet

is skew to the normal of the target plate to induce swirl around the central cone of the housing. The design directs coolant towards the swirl plate by inducing a vortex.

- **Spiral Plate**: The vortex flow strikes the swirl plate, which directs the flow in several spiral channels with a non-circular cross-section. Here is where the majority of the heat transfer occurs. The idea of a spiral-shaped, two-fluid heat exchanger [132–134], where the two fluids are separated by a thin metal strip, is not to be confused with the SPM, which is a single-fluid concept.

- **Backing**: The backing separates the inlet and outlet. A seal is formed by diffusion bonding the backing to the swirl plate and housing. The backing also prevents flow from one spiral channel from flowing into another in the radial direction. The backing also shapes the inlet flow into a pyramid-like vortex.

The maximum size of the test target was constrained by the output area of the CPC, such that it could be circumscribed by a hexagon. By circumscribing, the number of stray rays will be significantly lower than for an inscribed hexagon. Although safer for laser-based experiments, this method does not replicate heat flux conditions in DEMO, where the module might receive an even heat flux over the whole target surface. This constraint results in a side length (s) of 23.2 mm. Although the numerical studies in the following sections assume DEMO-like conditions, it is possible to simulate the heat flux conditions for the test apparatus.

6.2 1D Numerical Optimization

Having defined the SPM design, a one-dimensional model was created in MATLAB to optimize the geometry. The script was broken up into four distinct sections: material and constraint definitions, design space definition, thermodynamic and hydraulic performance, and result visualization. The following assumptions were made:

- The flow is one-dimensional along the θ_{sp} streamwise direction;

- The flow is single-phase;
- There is negligible contact resistance between the target and spiral plates;
- The curved channels range in the r_{sp} direction from the center of the hexagon to its apothem;
- The mass flow rate is divided equally among n spiral channels;
- Each channel is exposed to an equal amount of heat flux per unit area.

Water was used as the coolant, and the liquid and vapor properties were taken from the National Institute of Standards and Technology (NIST) tables [135]. The fluid properties were interpolated based on the input pressure and temperature. CuCrZr was chosen as the swirl plate material and tungsten as the target plate material. The material properties for both were interpolated based on an input temperature from Appendix A of the ITER Structural Design Criteria for In-vessel Components (SDC-IC) [83].

The maximum allowable temperature of the spiral plate, $T_{sp,max}$ was set to 350 °C per [85]. Above this temperature thermal fatigue/creep becomes apparent; irradiated material will have worse performance, and thus thermomechanical behavior of irradiated materials is a critical issue under investigation [136]. The tungsten target plate is limited by a operational window between 500 °C and 1300 °C that becomes even smaller with irradiation [137]. DBTT determines the lower limit, $T_{t,min}$, and recrystallization/creep the upper, $T_{t,max}$.

6.2.1 Parameter Space

The design space ranged over the values in Table 6.1, visually outlined by Fig. 6.5. The width of each channel, t_r, is implicity defined by the values of a_{sp} and the wall

thickness, t_w Eq. (6.7).

$$t_r = \frac{2\pi a_{sp}}{n} - t_w \tag{6.7}$$

The channel depth, t_z, and mass flow rate, $\dot{m}$, were also parameters of interest.

Table 6.1. Numerical design space of one-dimensional optimization script

n	t_z (mm)	t_w (mm)	a_{sp} (mm)	$\dot{m}$ $\left(\frac{\text{kg}}{\text{s}}\right)$
2 to 5	1 to 3	0.5 to 3	0.5 to 5	0.025 to 0.15

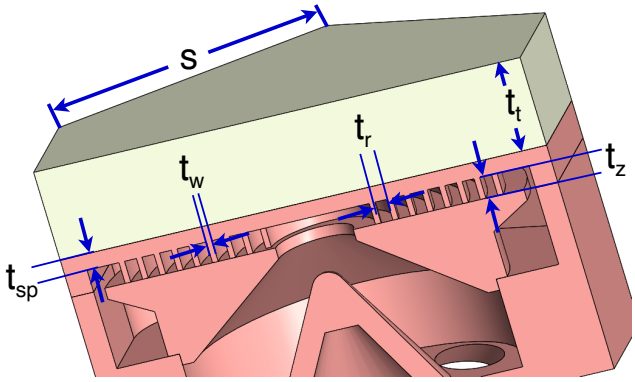

Figure 6.5. Cross-sectional view of the target concept. The critical features, including the wall thickness, channel width, and channel depth are all displayed. The sizing factor, a_{sp}, and the number of channels, n, determine the distance between each consecutive spiral.

In correspondence with [55, 56], the reference pressure, P_{ref}, was set to 20 MPa and the spiral plate thickness, t_{sp} was set to 1.4 mm. Recent studies have established a tungsten armor thickness, t_t, of 8 mm for the ITER-like monoblock to increase erosion lifetime [138]. The channels were spaced evenly around 360°; so if for example, there are four channels, they are each 90°apart. Finally, the fluid inlet temperature was set to 150 °C, which corresponds to the lower limit for CuCrZr embrittlement [32, 84].

The static inputs to the MATLAB code are expounded in Table 6.2. A steady-state heat flux input of 10 $\frac{\text{MW}}{\text{m}^2}$ was set for initial studies, but further investigation is required for the slow-transient heat fluxes in the range of 17-21 $\frac{\text{MW}}{\text{m}^2}$ [32].

Table 6.2. Static inputs to MATLAB optimization script. The choice of each parameter value is substantiated by the citation next to its name.

Parameter	Value	Units
s[1]	23.2	mm
t_{sp} [56]	1.4	mm
t_t [138]	8	mm
$\dot{q}$ [19]	10	$\frac{\text{MW}}{\text{m}^2}$
T_{ci} [84]	150	°C
P_{ref} [56]	20	MPa

6.2.2 One-Dimensional Modeling

The maximum value of θ_{sp} occurs when r_{sp} is equal to the length of the apothem, $l_{apothem}$, and it can be found by plugging into Eq. (6.5):

$$\theta_{sp,max} = \frac{a_{sp}}{l_{apothem}} = \frac{a_{sp}}{\frac{\sqrt{3}}{2}s} \tag{6.8}$$

The length along one spiral, l_{sp}, is a function of θ_{sp} and can be found by substituting Eq. (6.5) into the formula for the length of a polar curve:

$$\begin{aligned} l_{sp} &= \int \sqrt{r^2 + \left(\frac{dr}{d\theta_{sp}}\right)^2} d\theta_{sp} \\ &= a_{sp} \int \sqrt{1 + \theta_{sp}^2} d\theta_{sp} \\ &= \frac{a_{sp}}{2}\left(\theta_{sp}\sqrt{1+\theta_{sp}^2} + \sinh^{-1}\theta_{sp}\right) \end{aligned} \tag{6.9}$$

The orthogonal distance between loops of the same spiral is constant and equal to $2\pi a_{sp}$, so the distance between different spirals is $\frac{2\pi a_{sp}}{n}$. If this distance is less than t_w, the design is deemed invalid because the paths overlap.

[1]Determined by the area of the exit aperture of the CPC

For a polar equation $r(\theta)$, the radius of curvature is defined as [139]:

$$R_c = \frac{(r^2 + r_\theta^2)^{\frac{3}{2}}}{|r^2 + 2r_\theta^2 - r r_{\theta\theta}|} \tag{6.10}$$

The curvature is thus also a function of a_{sp} and θ_{sp}. Plugging in Eq. (6.5), the radius of curvature for an archimedean spiral is:

$$R_c = a_{sp} \frac{(\theta_{sp}^2 + 1)^{\frac{3}{2}}}{\theta_{sp}^2 + 2} \tag{6.11}$$

Correlations involving the Dean number are typically only valid for values of $\frac{2R_c}{D_h}$ greater than unity. Taking the lower limit of Eq. (6.11), R_c has a minimum value of $\frac{a_{sp}}{2}$. It is possible, therefore, that $\frac{2R_c}{D_h}$ is less than unity near the center of the spiral, and this geometry would require numerical simulation to adequately resolve. However, based on the values from Table 6.1, the minimum value of $\frac{2R_c}{D_h}$ increases to unity at just over $0.08 l_{sp}$. Consequently, in all cases where $\frac{2R_c}{D_h}$ falls below the bounds of a correlation, the author has assumed that the correlation is still valid due to the negligible length over which it is out-of-bounds.

6.2.3 Pressure Drop

The hydraulic losses in the SPM come from major and minor losses. Minor losses like the change of direction in the inlet and outlet and transition to the spiral plate are considered negligible. Major losses are accounted for by the pressure drop due to friction in the spiral channels. The friction factor for turbulent flow in smooth, straight pipes is given by the Petukhov correlation:

$$f_s = (0.79 \ln Re - 1.64)^{-2} \tag{6.12}$$

Unlike straight channels, the transition to turbulence does not include an increasing friction factor for higher Reynolds numbers, which then falls again once fully-

developed turbulence is achieved. Instead, the friction factor in curved channels monotonically decreases, but is always larger than or equal to a corresponding straight channel [140]. The transition to fully-developed turbulence occurs over a wider range and at a higher critical Reynolds number Re_c for flow in curved pipes. Because the radius of curvature is maximum at the outer channel wall and minimum at the inner, the outer portion may be turbulent while the inner remains laminar. Cioncolini and Santini experimentally determined critical Reynolds numbers for various strengths of curvature [140]:

$$\text{Strong Curvature} \quad Re_c = 30,000 \left(\frac{2R_c}{D_h}\right)^{-0.47}, \qquad \frac{2R_c}{D_h} \leq 24 \quad (6.13a)$$

$$\text{Medium Curvature} \quad Re_c = 120,000 \left(\frac{2R_c}{D_h}\right)^{-0.57}, \qquad 30 \leq \frac{2R_c}{D_h} \leq 110 \quad (6.13b)$$

$$\text{Mild Curvature} \quad Re_c = 2,300 \left[1 + 210 \left(\frac{2R_c}{D_h}\right)^{-1.12}\right], \qquad \frac{2R_c}{D_h} \geq 150 \quad (6.13c)$$

Thus, the flow can be laminar at the beginning of the spiral, where the curvature is lowest, but turbulent at some point later where the centrifugal forces are lower. Only strong and medium curvature is relevant for the design space specified in Table 6.1. The experimental results in [140] for strong and medium curvature coils align well with Ito's friction factors for both laminar and turbulent flow in curved channels, Eq. (6.14) and Eq. (6.15), respectively [141].

$$f_c = 4\frac{344\left(\frac{2R_c}{D_h}\right)^{-0.5}}{\left[1.56 + \log_{10} De\right]^{5.73}}, \qquad (6.14)$$

$$13.5\left(\frac{2R_c}{D_h}\right)^{0.5} \leq Re \leq 2000\left[1 + 13.2\left(\frac{2R_c}{D_h}\right)^{-0.6}\right] \cup 5 \leq \frac{2R_c}{D_h} \leq 2000$$

$$f_c = 4\left[0.076Re^{-0.25} + 0.00725\left(\frac{2R_c}{D_h}\right)^{-0.5}\right], \tag{6.15}$$
$$Re \geq 15,000 \ \cup \ 5 \leq \frac{2R_c}{D_h} \leq 2000$$

Where the factor of four is to convert from a Fanning friction factor to Darcy-Weisbach. Cioncolini and Santini's experimental results show that the friction factor monotonically decreases [140], so the maximum between Eq. (6.14) and Eq. (6.15) was chosen for flows that are in the transitional region.

The pressure drop was then found by summing over all the differential lengths, δl along the length from Eq. (6.3):

$$\Delta P_{fric} = \sum f_c \frac{\delta l_{sp}}{D_h} \frac{\rho_f v_b^2}{2} \tag{6.16}$$

The pumping power is defined as:

$$\dot{P} = \frac{\dot{m}\Delta P_{fric}}{\rho_f} \tag{6.17}$$

The pumping ratio, η_P, is an important parameter to determine whether or not the pressure drop is too large based on the total incident heat flux. A_t is simply the area of a regular hexagon with side length s:

$$\eta_P = \frac{\dot{P}}{\dot{Q}} = \frac{\dot{P}}{A_t \dot{q}} = \frac{\dot{P}}{\frac{3\sqrt{3}}{2}s^2\dot{q}} \tag{6.18}$$

For He-cooled divertors, this ratio must not exceed 10%, according to [34]. However, the value for η_P is typically significantly lower when water is used as the coolant. For example, the ITER-like MB concept has a pumping ratio of 0.0049 [56]. Therefore, this water-cooled design must meet or exceed the hydraulic performance of the ITER-like design.

6.2.4 Heat Transfer

The heat transfer was assumed to occur only at the HHF surface of the spiral channel and was negligible elsewhere. Fig. 6.6 shows a simplified thermal circuit to represent the heat flow in the system. The variables are defined as follows:

- T_b: Bulk fluid temperature (Eq. (6.22))
- T_w: Temperature at the fluid-solid interface on the upper surface of the channel (Eq. (6.33))
- T_{fin}: The wall that separates two fluid channels is treated as an adiabatic tip fin, extending from the HHF surface. T_{fin} is the temperature of the fin at it's base (Eq. (6.32)).
- T_{sp}: Temperature at the top surface of the spiral plate (Eq. (6.34))
- T_t: Temperature at the top surface of the target plate (Eq. (6.35))
- R_t: Thermal resistance through the thickness of the target plate (Eq. (6.26c))
- R_{sp}: Thermal resistance through the thickness of the spiral plate (Eq. (6.26b))
- R_f: Thermal resistance through the boundary layer of the fluid to the bulk fluid (Eq. (6.26a))
- R_{fin}: Equivalent thermal resistance of fin, where it is assumed that the temperature of the fin tip is equal to the bulk temperature of the fluid (Eq. (6.31))
- $\dot{q}$: The heat flux per unit area through the thermal circuit
- $\dot{Q}$: The heat flux through the thermal circuit (Eq. (6.21))
- $\dot{Q}_{fin}$: The heat transfer rate of the fin (Eq. (6.19))
- $\dot{Q}_f$: The heat transfer through the coolant boundary layer (Eq. (6.20))
- δl_{sp}: Differential length along the streamwise direction

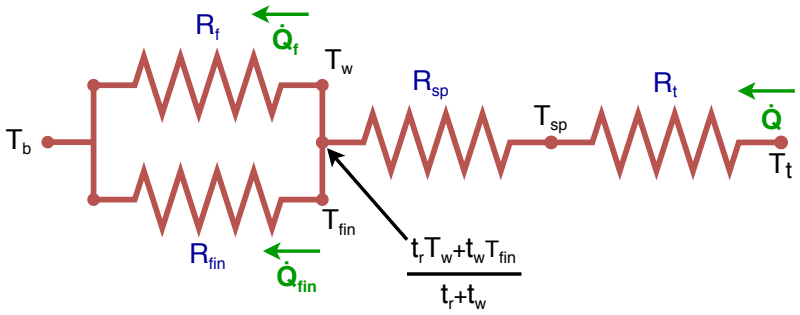

Figure 6.6. Thermal resistance diagram for 1D thermofluid model. It was assumed that the temperature at the tip of the fin is equal to the bulk temperature of the fluid. Furthermore, the temperature of the spiral plate was calculated using a weighted average of T_w and T_{fin}.

It was assumed that the bulk fluid absorbs all the heat from the top surface of the channel and the fin. The differential heat transfer rates for both the fin and fluid can be expressed over an effective area:

$$\delta\dot{Q}_{fin} = \dot{q}\delta l_{sp} t_w \tag{6.19}$$

$$\delta\dot{Q}_{f} = \dot{q}\delta l_{sp} t_r \tag{6.20}$$

$$\delta\dot{Q} = \delta\dot{Q}_f + \delta\dot{Q}_{fin} = \dot{q}\delta l_{sp}(t_r + t_w) = \dot{q}\delta A \tag{6.21}$$

Where δA is the differential area through which heat flux passes. The bulk temperature at a, T_b, is calculated via conservation of energy, assuming it remains below the saturation temperature.

$$T_b = T_{ci} + \frac{n\delta\dot{Q}}{\dot{m}c_p} \tag{6.22}$$

The temperature of the fin and the fluid-wall interface temperature are both functions of the heat transfer coefficient, h. This parameter was determined by correlations for internal flow.

Heat transfer through a straight channel is typically smaller than that for corresponding flow through a curved channel. The Nusselt number correlation for turbulent flow in a smooth, straight pipe can be found through the Gnielinski correlation [142]:

$$Nu_s = \frac{(f/8)(Re - 1000)Pr}{1 + 12.7(f/8)^{1/2}\left(Pr^{2/3} - 1\right)} \tag{6.23}$$

Where Pr is the Prandtl number. Turbulent flow entering a curve does not exhibit a thermal or hydrodynamic entry length [143]. The Nusselt number for laminar [143] and turbulent [144] flow in a curved channel is given by Eq. (6.24) and Eq. (6.25), respectively. The choice of equation is dictated by Eqs. (6.13a) to (6.13c).

$$Nu_c = 0.13\left(\frac{f}{4}Re^2 Pr\right)^{1/3}, \tag{6.24}$$
$$6,000 < Re < 65,000 \ \cup \ 2.9 < Pr < 5.7$$

$$Nu_c = \frac{Pr^{0.4}}{41.0}Re^{5/6}\left(\frac{2R_c}{D_h}\right)^{-1/12}\left\{1 + \frac{0.061}{\left[Re\left(\frac{2R_c}{D_h}\right)^{-2.5}\right]^{1/6}}\right\}, \tag{6.25}$$
$$Pr > 1$$

The local heat transfer coefficient, h, is then determined by substituting into Eq. (6.4). The individual resistances in the thermal circuit were then calculated by equations for convection through the fluid and conduction through the target plate and spiral

plate:[2]

$$\text{Convective fluid} \qquad r_f = \frac{R_f}{\delta A} = \frac{1}{h} \tag{6.26a}$$

$$\text{Spiral Plate Conduction} \qquad r_{sp} = \frac{R_{sp}}{\delta A} = \frac{t_{sp}}{k_{sp}} \tag{6.26b}$$

$$\text{Target Plate Conduction} \qquad r_t = \frac{R_t}{\delta A} = \frac{t_t}{k_t} \tag{6.26c}$$

The wall that separates channels was modeled as a finite, adiabatic tip fin. Because of the previous assumption that the fluid absorbs all the heat from both the top surface of the channel and the fin, the fin tip must be adiabatic, meaning that no heat is transferred from the walls of the spiral plate to the backing plate. The equations to determine the heat transfer rate through a fin of this type (Eqs. (6.27) to (6.30)) can be back-solved to determine T_{fin}. The free-stream temperature is T_b, the wetted perimeter, P_w, is δl_{sp}, and the cross-sectional fin area, A_c, is $\delta l_{sp} t_w$. The excess temperature at the base, θ_b, is defined as:

$$\theta_b = T_{fin} - T_b \tag{6.27}$$

The temperature distribution along the length of the fin is a type of exponential decay, with a decay rate m.

$$m^2 = \frac{hP_w}{k_{sp}A_c} \tag{6.28}$$

The heat transfer rate into the fin is directly proportional to M, which is a scaling factor that is dependent on boundary conditions.

$$M = \theta_b \sqrt{hP_w k_{sp} A_c} \tag{6.29}$$

[2]To clarify, when uppercase R is used, it is meant to represent a thermal resistance, while a lowercase r represents a thermal resistance per unit area.

For a fin with an adiabatic tip, the heat convected away by the bulk fluid is $\dot{Q}_{fin}$.

$$\dot{Q}_{fin} = M \tanh mt_z \tag{6.30}$$

Eq. (6.30) and Eq. (6.19) can be set equal to determine an equivalent fin resistance, R_{fin}, which can be used to find T_{fin}:

$$R_{fin} = \tanh mt_z \sqrt{hP_w k_{sp} A_c} \tag{6.31}$$

$$T_{fin} = T_b + \frac{\dot{Q}_{fin}}{R_{fin}} \tag{6.32}$$

The temperature at the spiral plate surface, T_{sp}, is found as the sum of the temperature increase due to solid resistance and the weighted average of the fin base temperature (Eq. (6.32)) and the fluid-wall interface temperature (Eq. (6.33)).

$$T_w = T_b + r_f \dot{q} \tag{6.33}$$

$$T_{sp} = \frac{t_r T_w + t_w T_{fin}}{t_r + t_w} + r_{sp} \dot{q} \tag{6.34}$$

Finally, the temperature of the target plate surface is determined via:

$$T_t = T_{sp} + r_t \dot{q} \tag{6.35}$$

The wall overheat was then defined using the maximum heat sink temperature, $T_{sp,max}$ [56]:

$$\tau_s = \frac{\dot{m} c_p \left(T_{sp,max} - T_{ci}\right)}{\dot{Q}} \tag{6.36}$$

For the dimensionless mass flow rate, the thickness of the heat sink, t_{sp}, and the target area, A_t, were used as the characteristic length and area scale, respectively, in Eq. (2.2).

$$m^* = \frac{\dot{m} c_p t_{sp}}{k_{sp} A_t} \tag{6.37}$$

6.2.5 Design Selection

A design from Table 6.1 was considered acceptable if it met the following constraints:

1. The surface temperature of the tungsten target plate must lie between 500 and 1300 °C [137].
2. The maximum surface temperature of the CuCrZr spiral heat sink must not exceed 350 °C [85].
3. The pumping power must not exceed 0.49% of the incident power [56].

If a specific design passes these constraints, the most important parameters to determine the 'best' design are η_P and τ_s. Fig. 6.7 reveals how the geometric parameters affect the pumping ratio and wall overheat.

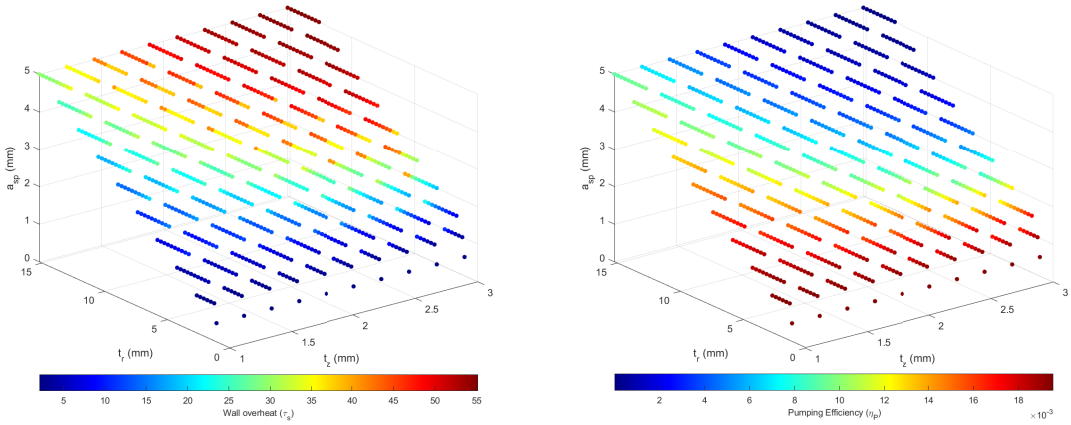

(a) **(b)**

Figure 6.7. The choice of geometry has a significant impact on τ_s (a) and η_P (b). In each of these graphs, the mass flow rate and the number of channels were held constant at 0.065 $\frac{\text{kg}}{\text{s}}$ and 2, respectively. All other inputs correspond to Table 6.2.

The effect of the number of channels was more difficult to visualize over the whole design space, so an arbitrary geometry was chosen to show how performance depends on n (Fig. 6.8).

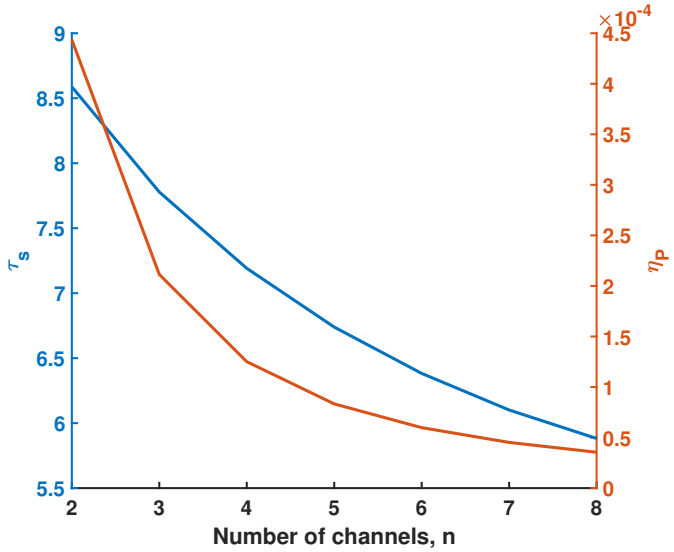

Figure 6.8. Performance of the SPM for both τ_s and η_P as they depend on n. The other geometric parameters were fixed at arbitrary values.[3]

[3]The other parameters were set as: $a_{sp} = 5$mm, $t_z = 2$ mm, $t_r = 1$ mm, and $\dot{m} = 0.065$ mm.

With $\dot{m}$ held constant, the outcomes for each of the independent variables were as follows:

- An increase in a_{sp} increases the curvature, R_c. This increased curvature results in a higher pressure drop and improved heat transfer. The pumping ratio increases and the wall overheat increases as a_{sp} increases.
- An increase in t_z or t_r both decrease the Reynolds number, meaning that the pressure drop and heat transfer coefficients will also decrease. Thus, the channel width and depth are inversely related to both pumping ratio and wall overheat.
- An increase in the number of channels, n, for a given a_{sp} and t_r, decreases the wall thickness, t_w. A smaller wall thickness means that a large portion of the target area is in contact with the coolant, leading to better heat transfer and thus lower τ_s. Moreover, the flow rate through each channel becomes smaller as n increases, meaning that the hydraulic friction is lower, and therefore η_P also decreases.

  There is, however, a trade-off for increasing n. As the wall thickness decreases, it may become so thin that it either cannot be machined without breaking or deforms under the pressure and thermal strain during steady-state operation.

Fig. 6.9 presents the results for the overall performance metrics over the entire design space. For a given mass flow rate, there is a trade-off between low τ_s and low η_P.

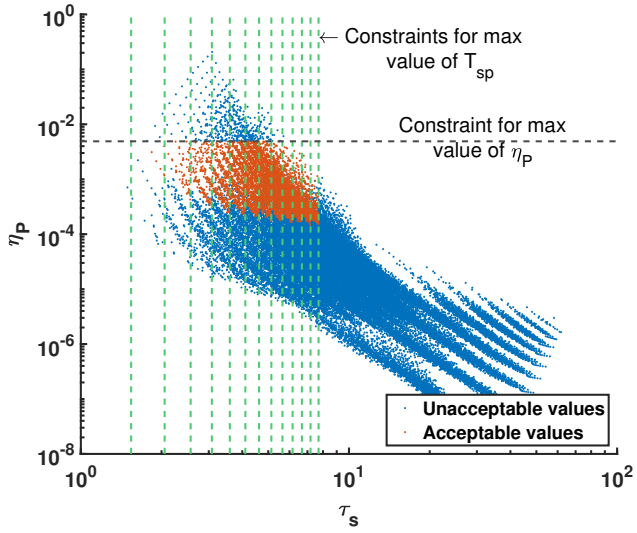

Figure 6.9. The performance of the entire design space from Table 6.1. The vertical green lines represent the $T_{sp,max} \leq 350$ °C for each of the mass flow rates simulated. The horizontal line corresponds to the pumping ratio achieved by an ITER-like MB concept [56].

To pick a geometry, it was also helpful to look at how wall overheat changes with respect to dimensionless mass flow rate. These results were compared to lines of constant Biot number. The Biot number, Bi, is an important figure of merit for heat exhaust, and it is the dimensionless ratio of thermal resistance due to conduction versus convection.

$$Bi = \frac{ht_{sp}}{k_{sp}} \tag{6.38}$$

Wall overheat can be rewritten as a function of m^* and Bi:

$$\tau_s = m^* \frac{Bi + 1}{Bi} \tag{6.39}$$

The dashed lines on Fig. 6.10 represent lines of constant Bi.

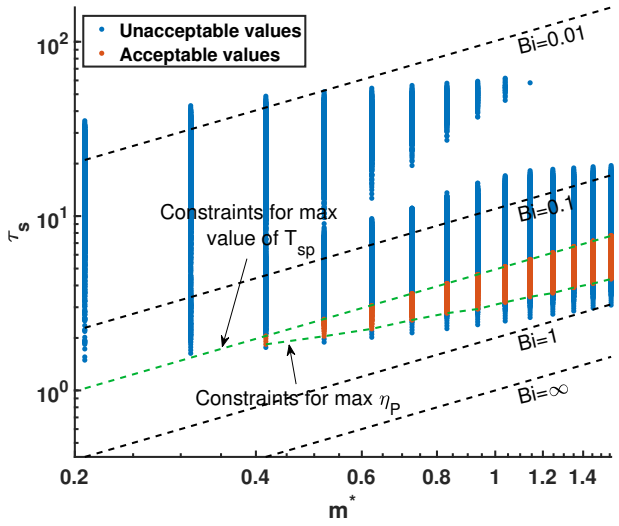

Figure 6.10. The performance of the entire design space from Table 6.1, visualized as the wall overheat versus the dimensionless mass flow rate. The acceptable designs were restrained both by the max temperature of the heat sink (i.e. minimum Bi) and the pumping ratio. The lines of constant Bi demonstrate τ_s drops as either convective heat transfer increases or conductive heat transfer decreases.

Thus, the larger the Biot number, the better the thermal performance for a given m^*. However, as wall overheat became lower and lower, the design was no longer considered acceptable because it surpassed the pumping ratio of the ITER-like monoblock reference design. Moreover, by equating Eq. (6.39) and Eq. (6.36), the minimum Biot number was found for an acceptable design, which corresponds to the upper green dashed line:

$$\begin{aligned} \frac{\dot{m}c_p\left(T_{sp,max}-T_{ci}\right)}{\dot{Q}} &= m^*\frac{Bi+1}{Bi} \\ Bi &= \frac{t_{sp}\dot{Q}}{k_{sp}A_t\left(T_{sp,max}-T_{ci}\right)-t_{sp}\dot{Q}} \end{aligned} \tag{6.40}$$

Choosing a single 'best' design was a trade-off between low pumping ratios and high wall overheat. Typically, a lower pumping ratio corresponds to a larger wall overheat, and vice-versa. More importance was placed on the cooling capabilities (and thus τ_s)

than the pumping ratio because avoiding CHF is imperative to protect hardware and the users.

The dimensionless mass flow rate m^* from Eq. (2.2) is more appropriate when comparing results for τ_s because it relates to the thermal characteristics of the fluid and heat sink. On the other hand, the Reynolds number is more appropriate for comparison of the pumping ratio because it relates to hydraulic characteristics. Re_A was defined such that the reference length is equal to the square-root of the heated area:

$$Re_A = \frac{\dot{m}}{\mu\sqrt{A}} \tag{6.41}$$

The chosen design has the geometric parameters listed in Table 6.3. The selected design was compared to both an ITER-like tungsten MB design and the HPJC divertor target (Table 6.4).

Table 6.3. Geometry and performance of chosen design from 1D modeling in MATLAB. The inputs to this simulation are outlined in Table 6.2.

n	a (mm)	t_z (mm)	t_r (mm)	t_w (mm)
2	0.5	1.9	1.07	0.5

Table 6.4. Comparison of the chosen design to ITER-like tungsten MB and HPJC concepts [56]. All results are for an incident heat flux of 10 $\frac{\text{MW}}{\text{m}^2}$. Results for the HPJC concept come from a numerical study where the peak heat sink temperature is 350 °C.

Design	τ_s	m^*	η_P	Re_A
ITER-like	91.3	16.7	4.9E-3	3.43E5
HPJC	4.08	0.749	0.86E-3	5.58E3
SPM (1D)	2.40	0.675	4.6E-3	8.54E3

Channel flow concepts like the ITER-like design have significantly higher wall overheat because the mass flow rate per unit area must be large to limit the CuCrZr temperature to 350 °C. Even though there is a relatively large pressure drop that is associated with impingement, the heat removal rate is significantly improved over

channel flow. For this reason, the pumping ratio of HPJC is significantly smaller. The one-dimensional model predicts that both m^* and τ_s are lower than that of the HPJC. On the other hand, the pumping ratio is comparable to, but still less than, the ITER-like design.

The one-dimensional modeling has some drawbacks that may lead to over-predicted performance. These trade-offs are discussed in Section 6.4.

6.3 Computational Validation

6.3.1 Model Creation

The 1-D optimization provided a geometry and preliminary results for a 3-D, steady-state, Computational Fluid Dynamics (CFD) study to verify. A conjugate heat transfer study in ANSYS 19.2 CFX was performed on the full geometry, as no symmetries were present.

Water was modeled using the IAPWS-97 (International Association for the Properties of Water and Steam) library in CFX. Fluid properties from this library are valid from 273.15 K to 1073.15 K and up to 100 MPa. A reference pressure of 20 MPa was chosen based on the HPJC concept [56]. The CuCrZr and W armor properties were taken at a reference temperature of 300 °C and 900 °C, respectively, from [83].

A constant, uniform heat flux of 10 $\frac{\text{MW}}{\text{m}^2}$ was applied to the top surface of the target plate, and all other external surfaces were adiabatic. The fluid inlet was given a mass flow rate boundary condition with a temperature of 150 °C, which meets the lower limit for CuCrZr embrittlement [32, 84]. In initial simulations the outlet experienced some backflow, indicating that it may be close to a recirculation zone. Therefore, the outlet was given an Opening boundary condition with a static relative pressure of 0 Pa and static opening temperature set to the mass flow averaged temperature at the outlet. The flow directions at the inlet and outlet were set parallel to their respective axes. All boundary conditions are outlined in Fig. 6.11.

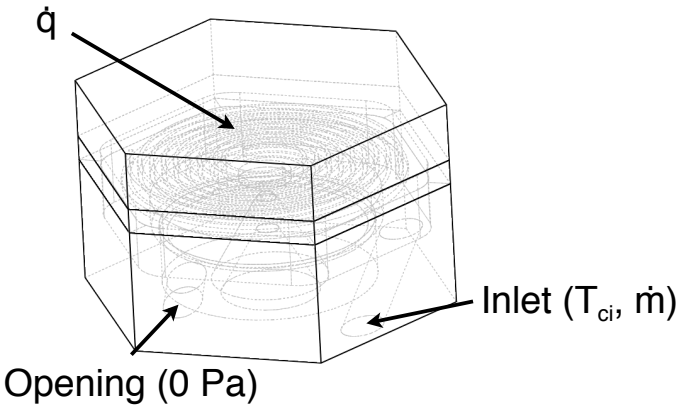

Figure 6.11. Boundary conditions applied to the model in CFD. The outlet pressure is relative to P_{ref}.

The advection scheme and turbulence numerics were both set to High Resolution. The heat transfer in all domains was set to thermal energy because kinetic effects were negligible, since the Mach number was below 0.3 in the fluid [145].

Prism layers close to the solid-fluid interface are used to capture near-wall effects. By providing a finer mesh close to no-slip boundaries, the viscous sublayer, buffer layer, and the log-law layer can be resolved. Without the prism layers, the mesh would be coarse close to boundaries, and wall effects would not be predicted correctly.

The dimensionless parameter, y^+, is used to determine whether the effects of the near-wall flow can be captured appropriately for a given solver. The value of y^+ is related to the height of the cell closest to the wall, h_1, and can be determined via Eqs. (6.42) to (6.44) and (6.46).

$$\frac{1}{\sqrt{C_f}} = 4.0 \log_{10}\left(\frac{Re\sqrt{C_f}}{1.26}\right) \tag{6.42}$$

$$\tau_w = \frac{1}{2} C_f \rho_f v_b^2 \tag{6.43}$$

$$u_\tau = \sqrt{\frac{\tau_w}{\rho_f}} \tag{6.44}$$

$$u^+ = \frac{u}{u_\tau} \tag{6.45}$$

$$y^+ = h_1 \frac{\rho_f u_\tau}{\mu} \tag{6.46}$$

The skin friction coefficient, C_f, is given by [146] for internal, turbulent flow in a smooth pipe. The wall shear stress τ_w and frictional velocity u_τ are intermediate values to determine the value of y^+. The dimensionless velocity, u^+, can be plotted against y^+ to demonstrate the different regimes of the boundary layer (Fig. 6.12).

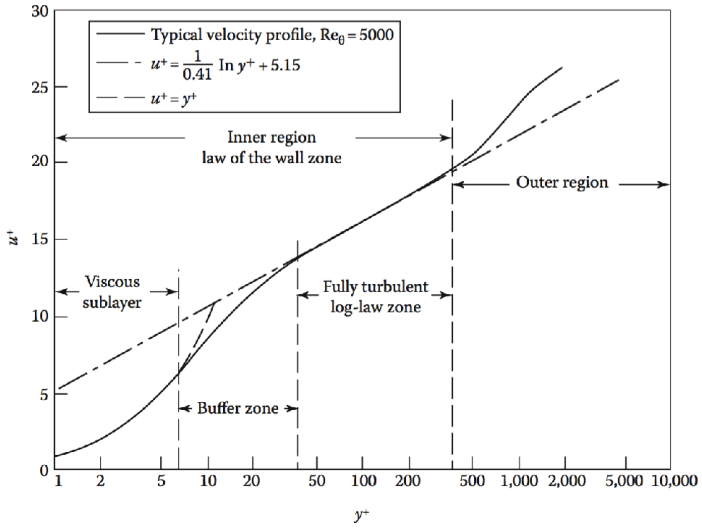

Figure 6.12. For an arbitrary turbulent flow over a plate, the different regimes of the boundary layer are shown. The flow is laminar in the viscous region, and eventually transitions to turbulence in the log-law zone. Viscous effects are non-negligible in the inner region [147].

There are generally two ways to capture the behavior of the flow close to the walls: wall functions and wall resolved models. The wall resolved models are the most accurate, as they capture the behavior down to the viscous sublayer. This type of model requires that y^+ be less than 2 [145], which is computationally expensive. Wall functions, on the other hand, are used to approximate the behavior between the wall and the fully-developed turbulence (or log-law) region. This approach requires y^+ greater than 30 and uses significantly less computational power.

The choice of how to represent flow in the boundary layer depends on how the turbulence is modeled. A sensitivity study (Section 6.3.3) was performed to determine an appropriate boundary layer mesh.

6.3.2 Turbulence Modeling

The Reynolds numbers in the spiral channels are on the order of 10^5, well into the turbulent regime. Because turbulence is computationally difficult to predict on small scales [145], the Reynolds Averaged Navier-Stokes (RANS) equations take a statistical approach to turbulence. The RANS evaluate the Navier-Stokes equations using time-averaged values of the dependent variables, but add additional terms known as the Reynolds stress terms. These equations require a turbulence model to provide closure to the RANS equations. Boussinesq's approximation introduced the concept of turbulent viscosity, which can be thought of as internal fluid friction that arises from eddies in turbulent flow [148].

There are several methods to solve for the turbulent viscosity. Two-equation models are the most commonly used in CFD [149]. The following models were considered for this study:

- **k-ϵ:** This model and the k-ω model both utilize turbulent kinetic energy, k, and the second variable determines the scale of the turbulence. In this case, ϵ determines the length scale over which turbulence occurs [149]. CFX employs a scalable k-ϵ model, which allows arbitrarily fine mesh near the wall and thus $y^+ < 30$ [145]. The k-ϵ model is the industry standard for first approximations in CFD because it is fairly robust and predicts flow in the boundary layer well [145].

- **SST k-ω:** The k-ω model is similar to the k-ϵ in that it is a two-equation model for turbulent viscosity. However, the second variable (ω) models the characteristic time scale over which turbulence occurs [149]. The goal of this model is to predict near-wall flows more accurately than k-ϵ [145]. This model is also

highly sensitive to initial conditions and can diverge if not provided with close approximations to k and ω. CFX uses automatic wall treatment for all ω-based models, meaning that the solver can switch between fully-resolved modeling ($y^+ < 2$) and wall functions. The shear stress transport (SST) variation on this model was selected because it offers a better prediction of flow separation.

The scalable k-ϵ model was used to perform an initial study on mesh and mass flow rate sensitivity. The reference case (Section 6.4) then also used the automatic wall-treatment SST k-ω to obtain a better resolution in the boundary layer.

6.3.3 Mesh Sensitivity

Four levels of mesh refinement were tested – coarse, medium, fine, extra-fine – with 6.7, 9.6, 11.3, and 14.1 million fluid elements, respectively. Mesh refinement was applied to the base mesh, and then prism layers were grown to a specified height.

The log-law predicts a transition from the inner- to outer-layer at $y^+ = 300$ [147]. Assuming a mass flow rate of 0.065 $\frac{\text{kg}}{\text{s}}$, the total prism layer height at this transition point was determined to be 73 µm. Although the CFX k-ϵ model provides automatic wall treatment for $y^+ < 30$, the choice of prism layers sought to produce an average y^+ on the spiral plate top surface between 30 and 300, which is appropriate for wall functions [150]. Four prism layers were grown to this height with an exponential growth ratio of 1.2, which means that the first prism layer should have a y^+ value of 55.9, corresponding to a first layer height of 13.7 µm.

It was assumed that the heat transfer through the CuCrZr parts was negligible compared to that of the fluid. Therefore, the spiral plate, backing, and housing could all be modeled as a single body. Thus, the geometry was defined as three different bodies (Fig. 6.13) – the tungsten target plate, the CuCrZr components, and the fluid region.

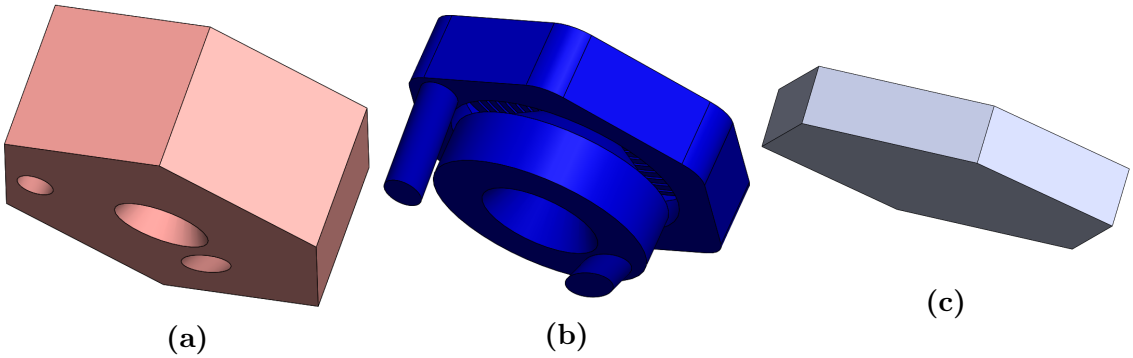

Figure 6.13. The target was modeled as three separate bodies. The CuCrZr structural components (a) could be modeled as a single body because the thermal contact resistance between them was assumed negligible. The fluid was modeled as the space within the body (b). And the tungsten target plate (c) was modeled separately from the CuCrZr components so that it could be assigned different thermomechanical properties.

The unstructured, tetrahedral meshes for each body were created in ICEM. The minimum quality of the fluid mesh before adding prism layers was above 0.3, which is the limit recommended by [151]. The surface mesh of the fluid is shown in Fig. 6.14, with a cross-section that captures the prism layers.

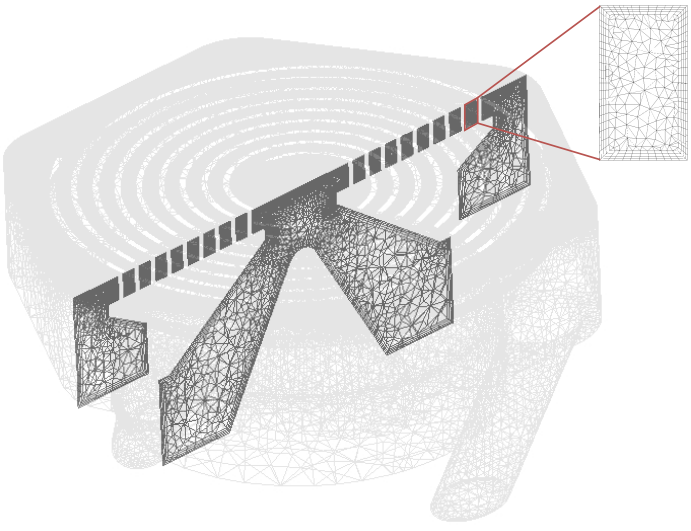

Figure 6.14. Surface mesh of the fluid domain. A cross-section of the mesh is highlighted and shown up close, demonstrating the use of boundary prism layers.

A mesh sensitivity study was performed on the geometry with four levels of refine-

ment. The meshes for the target plate and CuCrZr components were kept constant, with 9,300 and 2.4 million elements, respectively. Mesh independence was based on several variables, including maximum spiral plate temperature, maximum target plate temperature, the pressure drop, the mass flow-averaged outlet temperature, and the local heat transfer coefficient. Table 6.5 outlines the boundary conditions for the mesh sensitivity study.

Table 6.5. Boundary conditions imposed for the mesh sensitivity study

P_{ref} (MPa)	$\dot{q}\left(\frac{\text{MW}}{\text{m}^2}\right)$	T_{ci} (°C)	$\dot{m}\left(\frac{\text{kg}}{\text{s}}\right)$
20	10	150	0.065

All results achieved root-mean-squared residuals lower than 5×10^{-5} and global imbalances below 1%. Comparison of the results (Fig. 6.15) to the extra-fine mesh shows that all the parameters of interest, except the pressure drop, had less than a 0.25% difference. As this value is below the upper limit for global imbalances, this difference was not considered significant. The pressure drop did seem to converge as the mesh became finer, but only the coarsest mesh produced a significant difference greater than 1%.

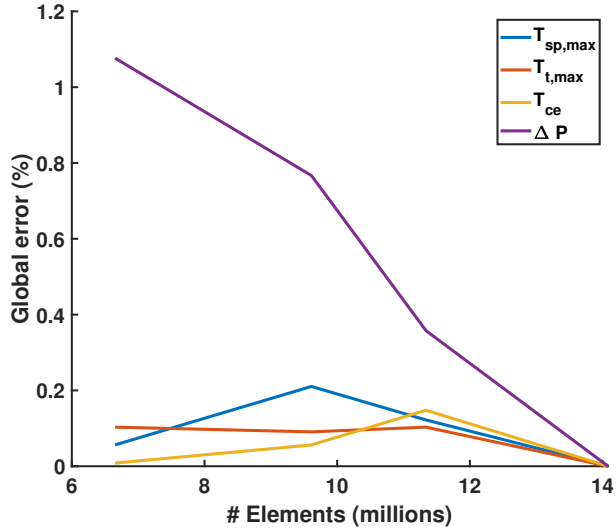

Figure 6.15. Error for key global parameters. The results from each mesh are compared to those of the extra-fine mesh with 15.1 million cells in the fluid region.

Local mesh sensitivity was determined by extracting data from along a line on the top surface and along the center of the spiral channel (Fig. 6.16). The local heat transfer coefficient, h, was defined as:

$$h = \frac{\dot{q}}{T_w - T_{ref}} \tag{6.47}$$

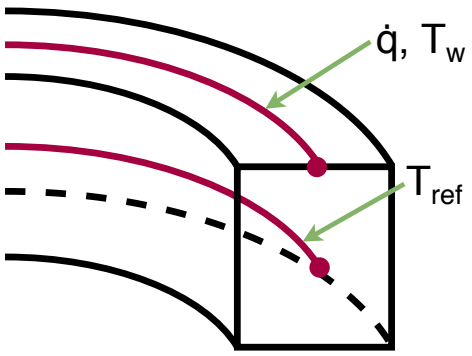

Figure 6.16. The local heat flux is determined by extracting a few parameters along the streamwise direction. The wall heat flux and wall temperature are obtained from a line on the top middle of the channel, while the reference temperature is obtained from a line in the center of the channel, directly below the top line. Because the flow is turbulent, this reference temperature is approximately equal to T_b.

Where T_{ref} is the reference temperature along the center of the channel, which is approximately equal to T_b in the spiral channel since the flow is turbulent. The local heat transfer coefficient is plotted along the normalized radius from the center of the target for all four meshes (Fig. 6.17). Visual inspection shows that all meshes roughly predict the same h.

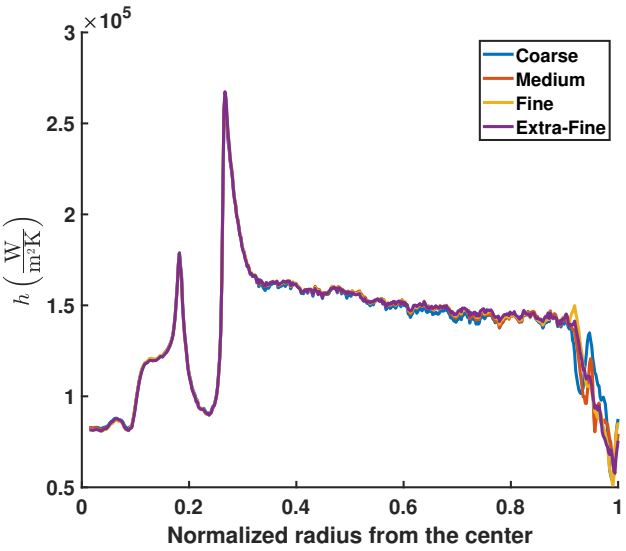

Figure 6.17. Comparison of local h for all four meshes, over the normalized radius from the center

Further comparison shows how the average error along the line in Fig Fig. 6.17 relates to the mesh refinement (Fig. 6.18). The relation is almost perfectly linear, showing that only the fine mesh comes within 1% of the extra-fine mesh, on average.

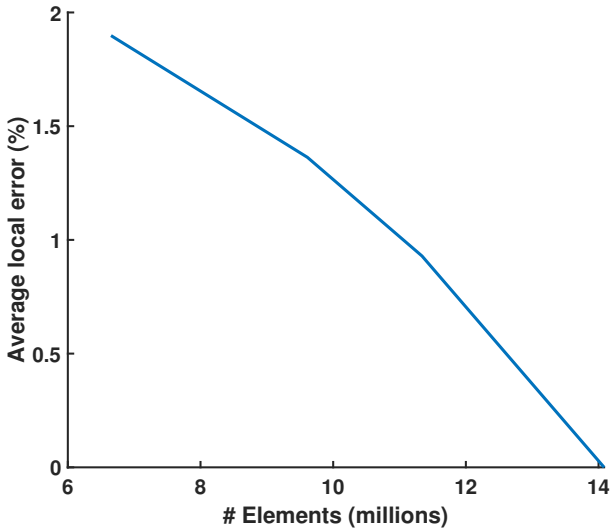

Figure 6.18. The average error for each mesh was calculated comparing that mesh to the next refinement. The extra fine mesh was the most fine, so the average error for it was 0% because it was compared to itself.

Given the results from global and local comparisons, the fine mesh was chosen as the reference mesh, as further refinement would have a negligible effect on the results.

6.4 Reference Case

Two reference simulations were performed with both the scalable k-ϵ and the k-ω SST with automatic wall treatment. The k-ω model used a mesh where the boundary layer was fully resolved, so although the tetrahedral base meshes are the same for the two models, there are significantly more prism layers in the k-ω mesh (Fig. 6.19). Mesh in the fully resolved model were grown such that $y^+ < 2$, per [145]. The desired y^+ values were confirmed by obtaining the average value on the heat flux surface; they were 97 and 1.15 for the k-ϵ and k-ω models, respectively.

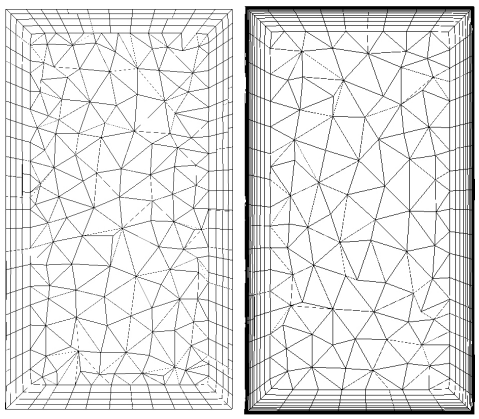

Figure 6.19. Zoomed in view of the cross-section of mesh in the spiral channel. Both meshes were grown to a height of 73 µm. The mesh in the k-ϵ model (a) uses wall functions and has 4 layers with a growth rate of 1.2, corresponding to a first layer height of 13.7 µm. The mesh in the k-ω model (b) fully resolves the boundary layer and has 19 layers with a growth rate of 1.3, corresponding to a first layer height of 0.15 µm.

Results for both reference meshes and the one-dimensional model are outlined in Table 6.6. The value of the ΔP used to calculate η_P in Eq. (6.18) was determined by calculating the mass flow averaged relative pressure at the inlet.

Table 6.6. Comparison of the CFD studies on the SPM to the 1D model in MATLAB. All results are for an incident heat flux of 10 $\frac{\text{MW}}{\text{m}^2}$. Mass flow rates for both k-ϵ and k-ω studies are such that the maximum temperature of the CuCrZr heat sink was nominally 350°C.

Design	τ_s	m^*	η_P	Re_A
SPM (1D)	2.40	0.675	4.6E-3	8.54E3
SPM (k-ϵ)	3.34	0.675	3.3E-3	8.54E3
SPM (k-ω)	3.31	0.675	3.2E-3	8.54E3

The one-dimensional MATLAB model under-predicts the wall overheat, but over-predicts the pumping ratio. These discrepancies are likely due to a few reasons:

- The 1D model does not include edge effects, which leads to an under-prediction of the maximum heat sink temperature. The edges of the SPM are, in reality, not cooled via a spiral channel (as the 1D code assumes), but instead by the flow exiting the spiral channels, where the heat transfer coefficient becomes significantly lower.

- The 1D model does not account for the initial swirling flow that strikes the heat sink surface. Instead, it assumes that there is no thermohydraulic entrance length and the spiral channel begins at the center of the target. For this reason, the pressure drop is higher in this region in the 1D model, but the heat transfer coefficient is actually over-predicted. These two conclusions would lead to a lower τ_s, but higher η_P, in the 1D model.

- In the 1D model, the bottom of the target plate, where it comes into contact with the backing and housing, is considered adiabatic; whereas the CFD model treats the target plate, backing, and housing as one thermally continuous body. The fluid will therefore absorb some heat in the inlet region before it strikes the spiral plate. Thus, the 3D model would predict a higher τ_s.

- The 1D model assumes that the walls behave as a fin, meaning that the temperature gradient is negligible other than in the z-direction. This is not in fact

the case, as the temperature changes through the width of the wall, as well.

The CFD results, however, are numerical and not experimental. Experimental work is needed to validate the CFD code, and there are several differences that are likely to appear in an experiment, for instance:

- The machined surfaces of the channels would likely not be considered hydraulically smooth. This inherent roughness could lead to both improved heat transfer coefficients (i.e. lower wall overheat) and higher friction factors (i.e. higher pressure ratio).
- The turbulence models are just that. There is no way for traditional CFD to correctly predict turbulent behavior. By using the wall resolved, k-ω model, a better prediction was obtained because wall functions were not used, but it is still an approximation.
- Boundary conditions are also nominal, meaning that they will not exactly match the actual operating conditions of an experiment.
- The fluid and solid thermomechanical properties were modeled at a single temperature. In reality, these properties will change as the temperatures within each domain vary.

The following sections describe local behaviors from the CFD studies. There were three regions of interest on the heat flux surface of the fluid Fig. 6.20 – the center (where the swirling flow first strikes the spiral plate), the spiral (where the flow is channeled through the spirals), and the outlet (where the flow exits the channels and moves around the outside toward the outlet).

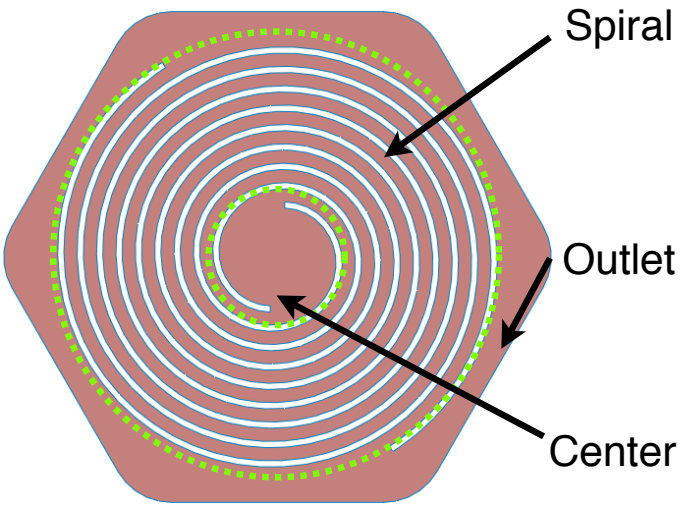

Figure 6.20. Considering local phenomenon, there were primarily three regions of interest: the center, spiral, and outlet.

6.4.1 Heat Transfer Distribution

A contour plot of the heat transfer coefficient is shown in Fig. 6.21. Although a more appropriate estimation is obtained by setting T_{ref} in Eq. (6.47) to the temperature in the center of the channel (like in Fig. 6.16), this plot was constructed with $T_{ref} = T_{ci}$ purely for visualization purposes.

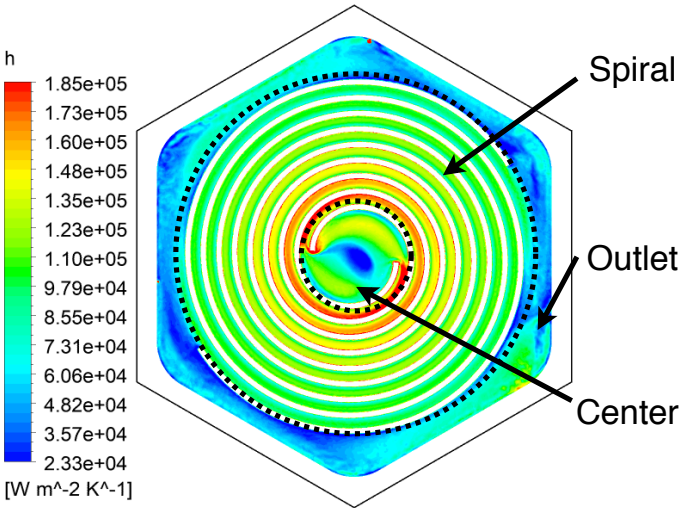

Figure 6.21. A contour plot of the local heat transfer coefficient. Results were produced from the k-ω study with $T_{ref} = T_{ci}$. There are three main regions – the center, spiral, and outlet – separated by the black dotted lines for clarity.

The heat transfer coefficient was low where the swirling flow first strikes the spiral plate, but then quickly increased in the center region. Upon entering the spiral region, there appeared to be some thermal entrance length before h steadily decreases radially outwards. As the flow exited through the outlet region, there were some edge effects where h decreased and then increased as it was squeezed along the hexagonal edge.

Fig. 6.22 shows a comparison of the two reference simulations and 1D model. Typically, k-ω does a better job predicting flow separation, which is the likely cause for why this model predicts a lower h at the center of the target. In the spiral section, the average difference between the k-ω and k-ϵ models was 8.0%. In this section, k-ω predicts a higher h likely because the mesh fully resolves the boundary layer, whereas k-ϵ only models the boundary layer through wall functions.

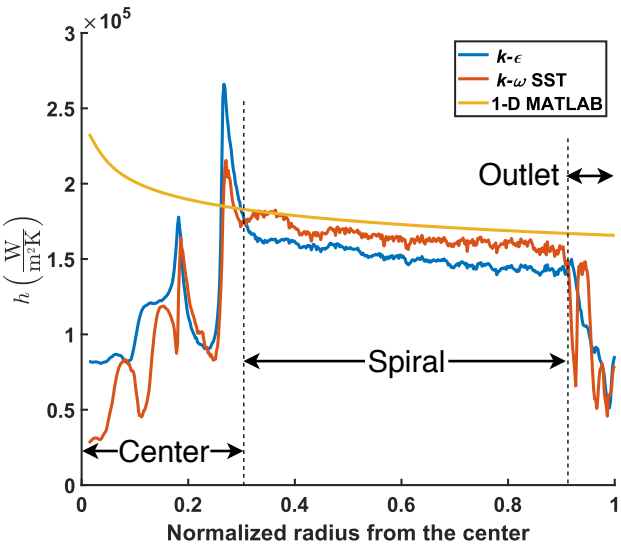

Figure 6.22. Variation of local heat transfer coefficient along the normalized radius. The curves along which the CFD data was extracted are visualized in Fig. 6.16. In the 1D model, the value of T_{ref} was set to T_b from Eq. (6.22).

The 1D model does a poor job of predicting h in the center and outlet region, but this was expected because it treated entire geometry as a spiral channel flow. On the other hand, the MATLAB model predicts h very close to that of the CFD models in the spiral section. Compared to the results from k-ω, there was only a 5.2% average error.

As predicted by heat transfer correlations in Dean flow, h does steadily decrease in the spiral section as the radius of curvature, R_c, becomes larger.

Although the global performance from Table 6.6 shows a large difference between the CFD and 1D models, the local results in the spiral region show a strong agreement. Because the 1D model is based on equations from experimental data, this correspondence provides some validation to the CFD results.

6.4.2 Solid Temperature Distribution

Flow rates were set such that the maximum temperature on the target plate was nominally 350 °C. The temperature distributions on the fluid-solid interface and heat sink are shown in Fig. 6.23. The k-ω model predicted a peak solid temperature of 348 °C, which differs by only 0.6% from the nominal value.

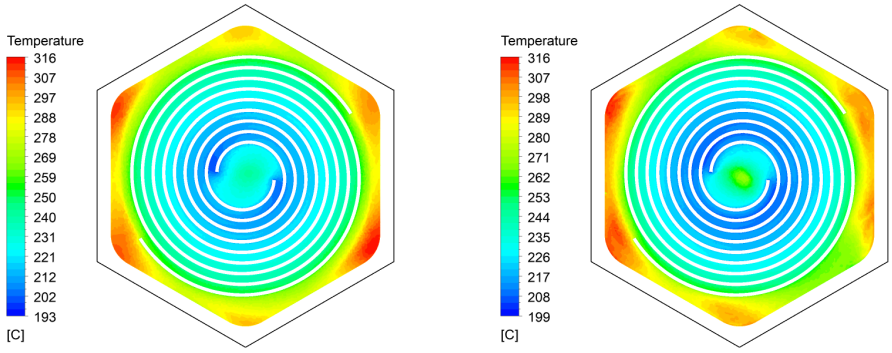

(a) Fluid-Solid Interface (k-ϵ) **(b)** Fluid-Solid Interface (k-ω)

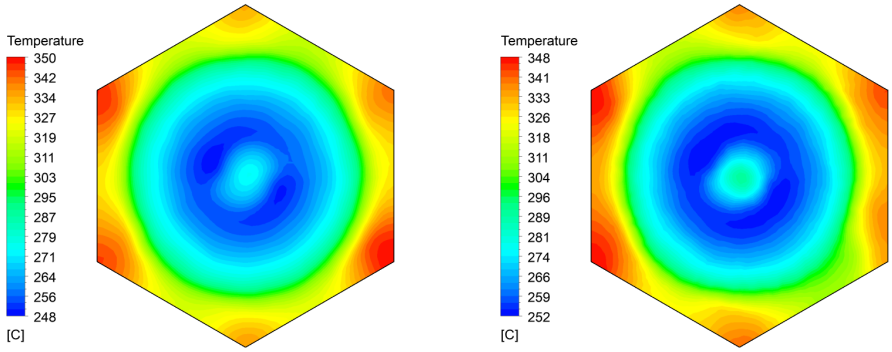

(c) Spiral Plate Surface (k-ϵ) **(d)** Spiral Plate Surface (k-ω)

Figure 6.23. Local temperature distribution on the top fluid wall for the k-ϵ (a) and k-ω (b) models. Local temperature distribution on the spiral plate surface in the k-ϵ (c) and k-ω (d) models.

There are several points to note from the temperature distribution on the fluid and solid heat flux surfaces. First, the minimum temperature of the fluid-solid interface was greater than 190 °C, meaning that the inlet temperature could be reduced to match the lower limit of 150 °C for CuCrZr embrittlement [32, 84]. By lowering the inlet temperature, the peak temperature on the solid could also be reduced. Interestingly, the temperature in the center region was a local maximum but quickly decreases as flow moves into the spiral section. This behavior likely occurs because h was much lower in the center region. Additionally, the maximum solid temperature occurred in the corners of the module. Similar behavior occurred in the HPJC concept [56], and it was suggested to either 1) decrease the solid thickness in these regions to decrease the path of thermal conductance or 2) change the geometry to increase the heat transfer coefficients in the outlet region. Point 2 can be addressed by increasing the number of channels or extending the spiral channels farther out radially.

6.4.3 Pressure Drop

The pressure drop is also an important consideration for determining where the design can be improved. Streamlines of the normalized pressure gradient are shown below (Fig. 6.24).

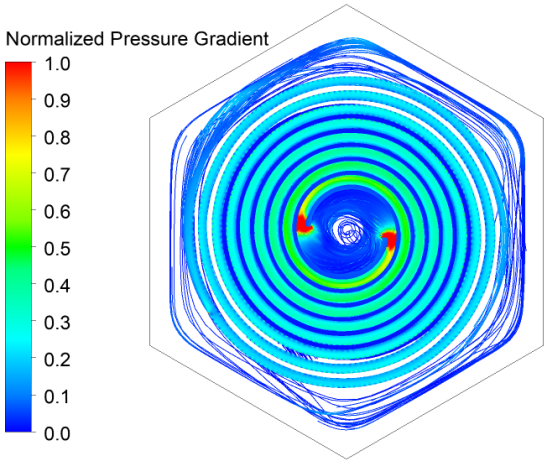

Figure 6.24. The normalized pressure gradient viewed on velocity streamlines. Areas of high pressure gradient are where the pressure drop is highest.

The pressure drop in the outlet and center sections were negligible compared to those in the spiral channel. The gradient was highest at the entrance to the channel, indicating that there was some hydraulic entrance length.

The local pressure drop and its gradient were considered in detail in Fig. 6.25. The values of relative pressure were obtained by plotting along a line that runs through the center of the spiral channel, similar to T_{ref} in Fig. 6.16. Fig. 6.25a also includes the relative pressure drop along just the spiral channel, which was more relevant for comparison to the CFD simulations.

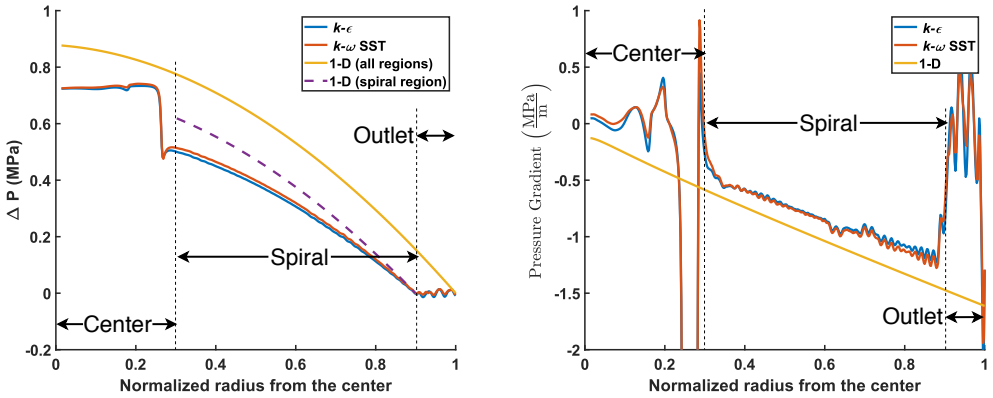

Figure 6.25. Local pressure drop (a) and pressure gradient (b) extracted from the center of the spiral channel, similar to T_{ref} in Fig. 6.16. The values are plotted over a normalized radius from the center. The pressure gradient was inherently noisy, so a smoothing function with a moving average filter was applied to the CFD data purely for visualization purposes.

Visually, the k-ϵ and k-ω models seem to match quite well, and in fact, there was only a 4.7% average difference between the pressure gradients of each in the spiral region. The MATLAB code predicted a higher pressure drop, and the pressure gradient was larger in magnitude, with an average difference of 29% in the spiral region when compared to the k-ω model. Although the correspondence was better for predicting the heat transfer coefficient, the fact that the CFD results in the spiral region roughly agreed with the 1D model gives further validation to the CFD simulation.

Although the entrance section, where there was a large pressure gradient, is relatively short, it contributed substantially to the overall pressure drop (36%). The magnitude of the gradient in this region could be improved by changing the geometry to gradually ease the flow into the spiral channel, as opposed to 'squeezing' the coolant all at once.

6.5 Divertor Target Design Comparison

6.5.1 Parametric Study

Having chosen a mesh, a parametric study was performed so that the target design could be compared to other divertor designs. Comparisons were performed for mass flow rates ranging from 0.05 to 0.14 $\frac{\text{kg}}{\text{s}}$ and heat fluxes of 10 and 20 $\frac{\text{MW}}{\text{m}^2}$ (Fig. 6.26).

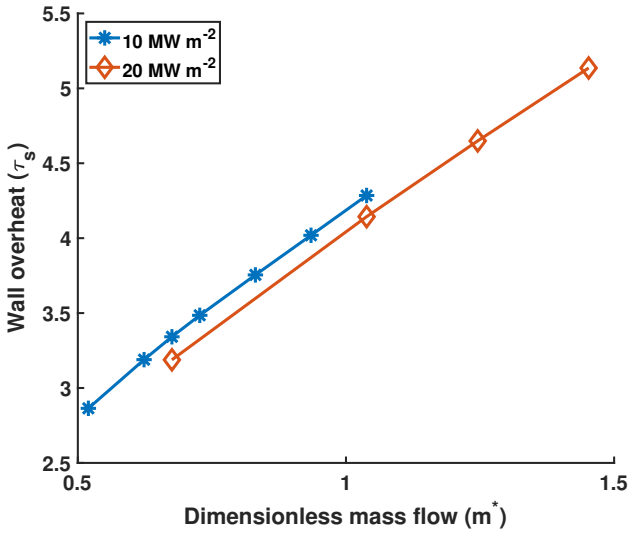

Figure 6.26. Parametric study results for the SPM concept, using results from the reference k-ϵ model. For a given dimensionless mass flow rate, m^*, τ_s was found at heat fluxes of both 10 and 20 $\frac{\text{MW}}{\text{m}^2}$.

As predicted by Eq. (2.1), the wall overheat was not strongly dependent on the incident heat flux, with only a 4.6% difference at 0.065 $\frac{\text{kg}}{\text{s}}$. The wall overheat appeared to have a linear correlation to the dimensionless mass flow rate.

While m^* presents a dimensionless mass flow rate based on thermal characteristics (and is thus more appropriate when comparing τ_S values), Re_A provides a dimension-

less mass flow rate based on fluid hydraulics and is better suited for comparison with the pumping ratio (Fig. 6.27).

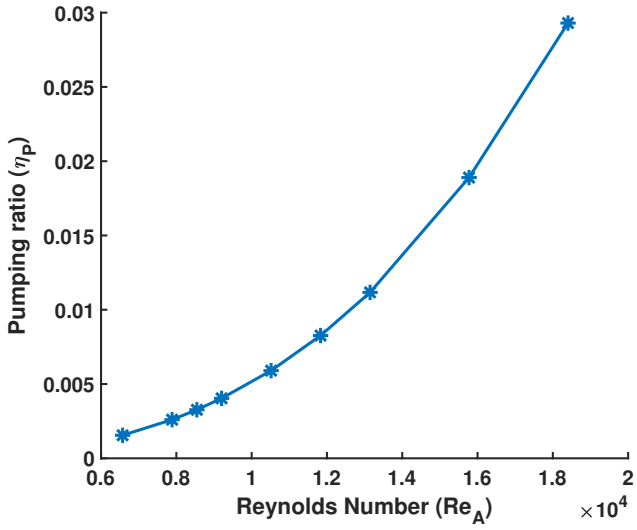

Figure 6.27. Parametric study results for the SPM concept, using results from the reference k-ϵ model. The pumping ratio is shown for a range Reynolds numbers, where the reference length is the square-root of the heated area. The incident heat flux for all points was 10 $\frac{\text{MW}}{\text{m}^2}$.

The pumping ratio was highly dependent on Re_A, increasing exponentially. Minimizing the mass flow rate is essential to achieving low pumping ratios.

6.5.2 Comparison to Other Divertor Concepts

The performance of the SPM was compared to other designs from the past and present. Nicholas et al. provided a comparison of the wall overheat of the HPJC to many other target concepts (reviewed in Section 2.2.2). Table 6.7 compares the results from the CFD studies to that of two leading designs.

Table 6.7. Comparison of the CFD studies on the SPM to the ITER-like and HPJC concepts [56]. All results are for an incident heat flux of 10 $\frac{\text{MW}}{\text{m}^2}$. Mass flow rates for the HPJC, k-ϵ, and k-ω studies were such that the maximum temperature of the CuCrZr heat sink was nominally 350°C.

Design	τ_s	m^*
ITER-like	91.3	16.7
HPJC	4.08	0.749
SPM (k-ϵ)	3.34	0.675
SPM (k-ω)	3.31	0.675

The CFD studies confirm the 1D model (Table 6.4) that both the wall overheat and the dimensionless mass flow rate are lower than that of the HPJC and ITER-like concepts to achieve similar results. For an equivalent value of m^*, the wall overheat of the SPM (interpolated from Fig. 6.26) is nearly 13% more effective at cooling than the HPJC. The SPM concept has the lowest wall overheat of all divertor target designs considered. The superb thermal performance is likely because this design utilizes a relatively short flow path, increased heat transfer coefficients associated with flow in curved channels, and even some impinging effects in the center region.

The pumping ratio is another important consideration that has been compared to other designs. Fig. 6.28 shows the relation between the pumping ratio and Reynolds number for a range of designs. A good design minimizes η_P for a given Re_A.

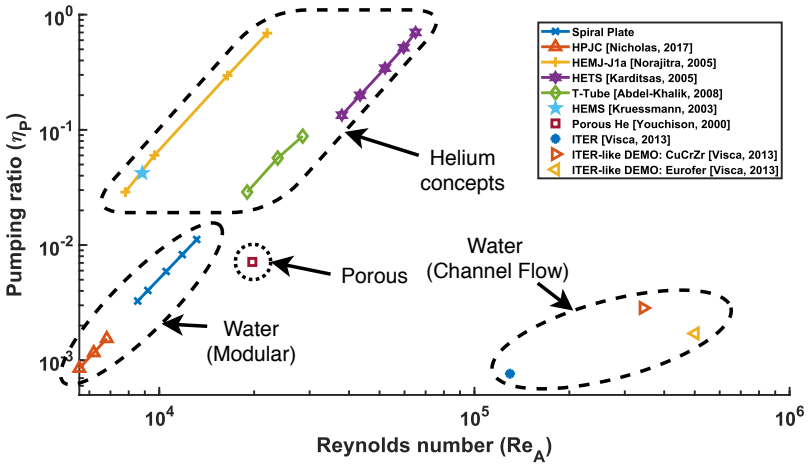

Figure 6.28. Comparison of the pumping ratios of several different divertor concepts as they vary with the Reynolds number [39, 42, 56, 152–155].[4]

The Helium-based concepts typically have a much higher pumping ratio than the ones that use a water coolant. The SPM has a good pumping ratio, on par with that of the ITER-like CuCrZr design, and it also touts a low Re_A. The pumping ratio for the SPM can be significantly improved by changing the geometry in the center region, as described in Section 6.4.3.

Another useful way to visualize performance is simultaneously comparing the pumping ratio and wall overheat (Fig. 6.29). A good design will have both low τ_S and η_P.

[4]This graph does not include some references from Fig. 2.14 because hydraulic data was not available.

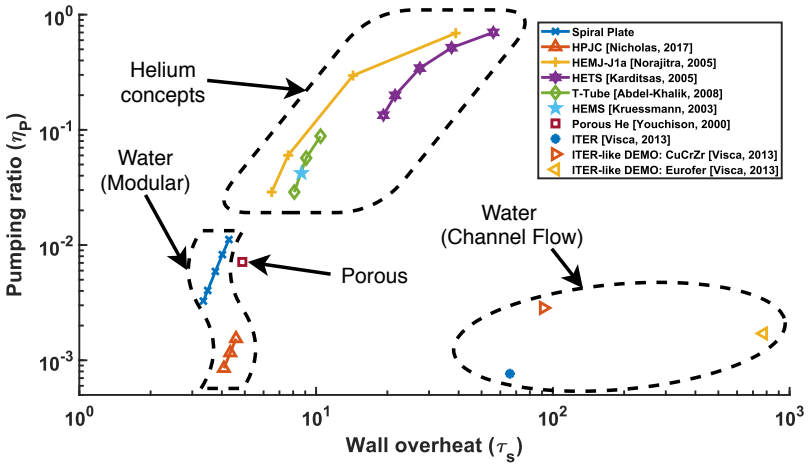

Figure 6.29. Comparison of the pumping ratios of several divertor concepts as they vary with wall overheat [39, 42, 56, 152–155].[5]

The SPM achieves the lowest wall overheat, but not the lowest pumping ratio. Nonetheless, the pumping power is still less than 1% of the incident heat flux, which is considered very good performance.

[5]This graph does not include some references from Fig. 2.14 because hydraulic data was not available.

Chapter 7

Facility Controller

The VCSEL modules by TRUMPF come with a National Instruments Labview software for primitive control. The controller has several capabilities, divided into tabs on the front panel (Fig. 7.1). Each laser module consists of six bars, which can be controlled individually to achieve the desired spatial power distribution. The software also can log data through an ethernet connection on the status of the various electronic systems that operate the lasers. Finally, the system has redundant safety features to protect both the users and the lasers. For example, the experimental rig room is interlocked during use and the lasers are provided with purge air and water cooling and cannot operate until these systems are engaged.

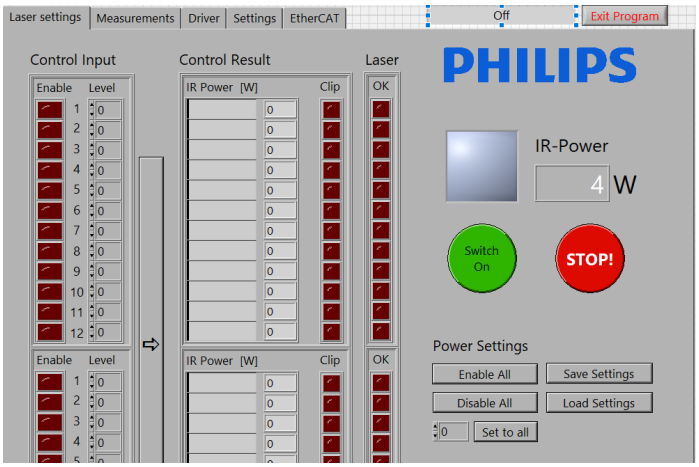

Figure 7.1. Front panel of 48 Channel Laser controller supplied by TRUMPF. The main labview controller was essentially 'wrapped around this virtual instrument to communicate with the lasers.

However, this controller is very basic and lacks the necessary capabilities. Therefore, the author designed a new Labview program, which encapsulates this basic controller, to meet the following feature requirements.

1. The user can provide any temporal, periodic power profile they desire
2. The program can log any historical analog or digital measurement signal
3. The periodicity of data logging can be either continuous or cyclical
4. The program monitors process parameters. Each process parameter has a warning and critical limit, at which either the user is warned or the lasers are shut off, respectively.

The program was divided into three front panels: Main Controller, Data Collection, and Process Monitoring. The Main Controller (Fig. 7.2) allows the user to control the power of the lasers over time. The user can choose from sine, sawtooth, and square waves which can be defined by the number of cycles, period, amplitude, and vertical offset with a temporal resolution set by Laser Update Frequency. Additionally, the user can write their own function, which will be repeated periodically for the number of cycles given. The input to this function is a Python 2.7 script, and cannot support the use of packages like numpy or scipy. A preview of the waveform is shown on the front panel once the user presses the "Show Preview" button. Any error in the custom-built function generator will display on the error panel. The user sets the global parameters for process and data measurement on this front panel.

Some experiments will be short (<1 minute) which will require continuous data collection at a specified frequency; other experiments may be significantly longer (>1 day), during which the user may desire cyclical data collection. Cyclical logging, where, for example, five data points are sampled at a rate of 1 Hz every 10 minutes, is useful for minimizing the amount of data that has to be post-processed. The Start Lasers button sends the time-varying signal to the basic Labview software provided by TRUMPF, which directly controls the lasers. The STOP button will cease all

power to the lasers immediately, and as a safety feature, the user cannot press the Start Lasers button while the STOP button is depressed.

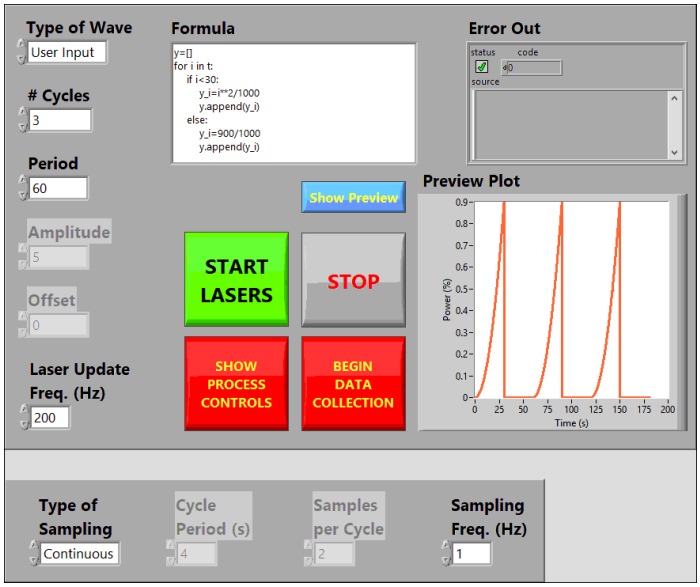

Figure 7.2. Front panel of main Labview controller

The Data Collection front panel (Fig. 7.3) can be opened on its own or during operation of the Main Controller. This front panel displays the global variables that control how data is logged. Additionally, the value from every sensor is displayed in an indicator and the historical data is shown on a chart. Once the data collection ceases, the data is written to a .csv file for post-processing. The data is read through an ethernet connection from a Data Acquisition System (DAQ) provided by National Instruments. The user can add sensors by altering the DAQ assistant node in the block diagram.

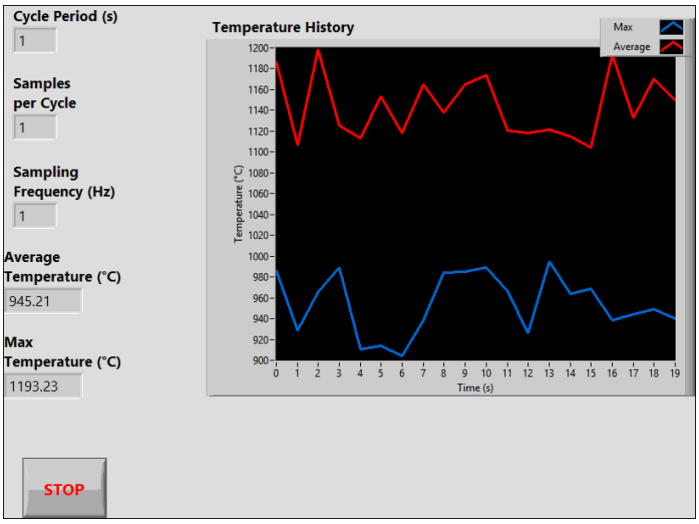

Figure 7.3. Front panel of Labview data collection

The Process Monitoring front panel (Fig. 7.4) consists of two tabs: General Readings and Setpoints/Details. The purpose of this virtual instrument is to monitor all of the process functions which are not crucial to record for post-processing but may result in harm to the user or experimental rig. The front panel constantly displays the actual readings of the processes, which also comes from a National Instruments DAQ. Every single process has either an upper or lower warning and critical limit, or sometimes both. The General readings tab shows the user if there are any faults in the system with a single boolean indicator. This indicator will be green if all processes are within the appropriate range, yellow if any process is in the 'warning' range, and red if in the 'critical' range. Any warning or critical process will be displayed in the text box next to the boolean indicator, and a noise alert will be played to get the user's attention if either arises. The STOP button will cease monitoring of all process monitors.

(a)

(b)

Figure 7.4. Front panel of Labview process monitor, including General tab (a) and Details tab (b)

The Setpoints/Details tab gives the user control of the warning and critical ranges of each process. Moreover, every process has an associated boolean indicator that follows the same color scheme as that on the General Readings tab. The list of all process recordings in in Table 7.1.

All the process parameters can be divided into a few categories:

- Flow rate sensors: There are several flow rates that are monitored. Most of these sensors measure water, but the ALICAT sensor measures air that cools the VCSEL modules. If the flow rate of the process water, for example, drops below a certain threshold, there could be a leak in the hydraulic system. If, on the other hand, the flow rate is too high, that could indicate that the coolant controller is sending more flow to stop a certain component from overheating.

- Thermocouples: There are many devices in the facility that could be damaged if they reach a certain temperature. For instance, the LED lights, which illuminate the testbed, cannot operate at an ambient temperature above 70 °C.
- Humidity sensors: there are two lines of dry air cooling, one to purge the VCSEL modules and the other to cool them. If either line becomes exposed to a critical amount of moisture, this could damage the electronics of the VCSEL module.

Some experiments will not utilize certain processes (for example, CPC thermocouples will only be used when the CPC is in use), so the user has the option to disable these readings. The software includes safety features to prevent non-intentional disabling.

Table 7.1. All process monitors for the experimental rig which can trigger a critical shutdown.

Process	**Units**	**Number of Measurements**	**Warning/ Critical Limits**
VCSEL Shield Flow Rate	SLPM	1	Upper and Lower
Panel Flow Rate	SLPM	1	Upper and Lower
Process Water Flow Rate	SLPM	1	Upper and Lower
Air Cooling (ALICAT) Flow Rate	SLPM	1	Upper and Lower
Rig Ambient Temp.	°C	2	Upper
Rig Ambient Temp.	°C	2	Upper
Room Ambient Temp.	°C	1	Upper
Frame Temp.	°C	1	Upper
Water Inlet Temp.	°C	1	Upper
Water Oulet Temp.	°C	3	Upper
Water-Cooled Panel Temp.	°C	8	Upper
Camera Temp.	°C	2	Upper
IR Camera Temp.	°C	2	Upper
LED Light Temp.	°C	4	Upper
VCSEL Shield Temp.	°C	8	Upper
VCSEL Module Temp.	°C	4	Upper
CPC Temp.	°C	2	Upper
CPC Bracket Temp.	°C	2	Upper
Purge Air Humidity	%	1	Upper
Cooling Air Humidity	%	1	Upper

Chapter 8

Conclusions and Future Works

8.1 Research Contributions

The goals of this thesis included (1) designing an optical system that can achieve fusion-relevant heating conditions using a new laser-based heating facility (OLAHF), (2) creating a novel divertor target concept that may be used as a PFC in DEMO, and (3) designing a facility controller and process monitor for OLAHF. The following are the numerous achievements that contributed to reaching the three goals:

- Numerous configurations of concentrators were designed and simulated to determine the concept with the best optical performance.
  - The four VCSEL modules with axes parallel to that of a single, large CPC produced the best results.
  - A concentration ratio of $C = 32.5$ and a target distance of $d_{RO} = 0.5$ mm achieves an average irradiance of 8.23 $\frac{\text{MW}}{\text{m}^2}$.
  - The heating across the target surface is fairly even, with a standard deviation of 1.66 $\frac{\text{MW}}{\text{m}^2}$.
- The area of the CPC exit aperture is 10.1 cm^2, which is large enough such that relevantly sized test specimen can be cooled.
- An anti-reflective coating was chosen for the target surface such that 98.9% of

the incident light is absorbed.

- Numerical simulations provide evidence that a small amount of air cooling on the outside of the CPC will prevent it from overheating. Under normal operating conditions, where the convective cooling rate is 50 $\frac{\mathrm{W}}{\mathrm{m^2K}}$ and the temperature of the target is 350 °C...
  - The temperature of the glass in the VCSEL module is around 29 °C, which is lower than the 70 °C limit;
  - The max deformation of the CPC is about 0.4 mm, which is less than the machining tolerance and therefore not significant enough to impact optical performance.
- A novel divertor target design was created – the SPM
  - The geometry of the design was optimized through a 1D model, based on the pumping ratio and wall overheat.
  - A numerical, steady-state CFD study was performed on the optimized design under DEMO-like conditions, and the results were compared to other divertor concepts.
  - The CFD results were compared to the 1D model in the spiral region of interest, and aligned well, meaning that the results have some validation.
  - The spiral plate design had the lowest wall overheat of all concepts considered while satisfying all the temperature requirements for both the tungsten armor and CuCrZr heat sink.
  - The pumping power necessary to cool the module was less than 1% of the incident heat flux.
- A facility controller was designed and created in Labview to safely control and monitor all processes in OLAHF remotely. Three user panels achieve this goal.

- The main controller gives the user complete customization control to vary the laser power in time. Here, the user can also set how they would like to collect data over time.
- The data collection panel shows and records key data points during experimental runs.
- The process monitor provides the user with real-time feedback on the health status of the experiment. Depending on the severity of the problem, this monitor can either warn the user or shut all systems down if a reading becomes either too high or low

8.2 Future Works

There are several potential works that may be done to build upon the results from this thesis:

- Experimental work needs to be done to validate the optical and thermal performance of the CPC. Optical validation can occur at lower power levels, but the thermal performance must be done at full laser power.
- The ray-tracing model can be improved by incorporating non-ideal surfaces that are not optically smooth nor perfectly reflective.
- The geometry of the spiral target should be improved to minimize the pressure drop in the center region of interest and lower the temperatures at the vertices of the hexagon.
- A steady-state, thermomechanical, numerical study should be performed on the spiral target concept. The pressure and temperature fields from the thermofluid study can be used as boundary conditions.
- Further effort is required to investigate the manufacturing methods for the spiral target. The author suggests classical machining or even metal 3D-printing for

initial experimental work.

- Thermohydraulic experimental validation should be performed on the spiral target concept using the CPC. This validation will provide more evidence that the design is a likely candidate to be used in a future DEMO divertor.
- The Labview facility controller must be linked with the testing facility, once it is ready for commission.

Bibliography

[1] *Global Grand Challenges*. Singularity University. URL: https://su.org/about/global-grand-challenges/ (visited on 03/14/2020).

[2] Cesar Pasten and Juan Carlos Santamarina. "Energy and quality of life". In: *Energy Policy* 49 (2012). Special Section: Fuel Poverty Comes of Age: Commemorating 21 Years of Research and Policy, pp. 468 –476.

[3] Irshad Ali Sodhar. *Essays by CSPs — Global energy crisis*. GCAol. URL: http://gcaol.com/essays-by-csps-global-energy-crisis/ (visited on 03/14/2020).

[4] R. F. Keeling et al. *Keeling Curve*. Scripps CO_2*Program*. URL: https://scrippsco2.ucsd.edu/ (visited on 03/14/2020).

[5] Martin I. Hoffert et al. "Advanced Technology Paths to Global Climate Stability: Energy for a Greenhouse Planet". In: *Science* 298.5595 (2002), pp. 981–987. eprint: https://science.sciencemag.org/content/298/5595/981.full.pdf.

[6] *The quality of life of individuals and societies is affected by energy choices*. CLEAN. URL: https://cleanet.org/clean/literacy/energy7.html (visited on 03/14/2020).

[7] *Fueling the Fusion Reaction*. ITER. URL: https://www.iter.org/sci/FusionFuels (visited on 03/14/2020).

[8] *Advantages of Fusion*. ITER. URL: https://www.iter.org/sci/Fusion (visited on 03/14/2020).

[9] *Plasma Physics*. Lawrence Livermore National Laboratory. URL: https://lasers.llnl.gov/science/understanding-the-universe/plasma-physics (visited on 07/03/2020).

[10] *The Solar Interior*. NASA, Marshall Space Flight Center. URL: https://solarscience.msfc.nasa.gov/interior.shtml (visited on 03/14/2020).

[11] *A star war on earth*. EURO Fusion. URL: https://www.euro-fusion.org/news/2018/november/a-star-war-on-earth/ (visited on 03/23/2019).

[12] *Creating a Star on Earth*. United States Department of Energy. URL: https://www.energy.gov/articles/creating-star-earth (visited on 03/05/2014).

[13] D. Merkl. "'Current Holes' and other Structures in Motional Stark Effect Measurements". In: 2004.

[14] *D-T Fusion*. University of Waikato. URL: https://www.sciencelearn.org.nz/images/245-d-t-fusion (visited on 03/14/2020).

[15] D. Mueller. "The physics of tokamak start-up". In: *Physics of Plasmas* 20.5 (2013), p. 058101. eprint: https://doi.org/10.1063/1.4804416.

[16] Robert Arnoux. *ITER ... and then what?* ITER. URL: https://www.iter.org/mag/3/22 (visited on 03/14/2020).

[17] *The demonstration power plant: DEMO*. EUROfusion. URL: https://www.euro-fusion.org/programme/demo/ (visited on 03/14/2020).

[18] Gregory Dubus. "From Plain Visualisation to Vibration Sensing: Using a Camera to Control the Flexibilities in the ITER Remote Handling Equipment (Doctoral Dissertation)". PhD thesis. Oct. 2014.

[19] F. Crescenzi et al. "ITER-like divertor target for DEMO: Design study and fabrication test". In: *Fusion Engineering and Design* 124 (2017). Proceedings of the 29th Symposium on Fusion Technology (SOFT-29) Prague, Czech Republic, September 5-9, 2016, pp. 432 –436.

[20] Christian Theiler. "Basic Investigation of Turbulent Structures and Blobs of Relevance for Magnetic Fusion Plasmas". PhD thesis. Dec. 2011.

[21] Sabina Griffith. *Design review for tungsten divertor shows way ahead*. ITER. URL: https://www.iter.org/newsline/274/1639 (visited on 03/14/2020).

[22] C. Day et al. "Initial studies of the divertor dome effect on pumping efficiency in DEMO". In: *2015 IEEE 26th Symposium on Fusion Engineering (SOFE)*. 2015, pp. 1–4.

[23] Pat Brans. *What will the blanket teach us?* ITER. URL: https://www.iter.org/newsline/-/3323 (visited on 03/14/2020).

[24] Armand Pruijmboom et al. "VCSEL arrays expanding the range of high-power laser systems and applications". In: *International Congress on Applications of Lasers & Electro-Optics* 2015.1 (2015), pp. 1–8.

[25] *VCSEL Infrared Power Systems*. Trumpf. URL: https://www.trumpf.com/en_GB/products/vcsel-solutions-photodiodes/vcsel-heating-systems/vcsel-infrared-power-systems/ (visited on 03/14/2020).

[26] Fabio Maviglia et al. "Impact of the monoblock thickness in an ITER-like configuration of DEMO divertor". In: *Fusion Engineering and Design* 136 (2018). Special Issue: Proceedings of the 13th International Symposium on Fusion Nuclear Technology (ISFNT-13), pp. 1322 –1326.

[27] *History of Fusion*. EUROfusion. URL: https://www.euro-fusion.org/fusion/history-of-fusion/ (visited on 03/14/2020).

[28] *How much power is needed to start the reactor and to keep it working?* EUROfusion. URL: https://www.euro-fusion.org/faq/top-twenty-faq/how-much-power-is-needed-to-start-the-reactor-and-to-keep-it-working/ (visited on 03/14/2020).

[29] R.A. Pitts et al. “Physics basis for the first ITER tungsten divertor”. In: *Nuclear Materials and Energy* 20 (2019), p. 100696.

[30] “Use of tungsten material for the ITER divertor”. In: *Nuclear Materials and Energy* 9 (2016), pp. 616 –622.

[31] *Our high quality wholesale price tungsten monoblocks*. Changsha Mingguan Metal Technology Co., LTD. URL: http://www.tungstenmoly.com/index.php?m=content&c=index&a=show&catid=24&id=42 (visited on 03/14/2020).

[32] J.H. You et al. “European DEMO divertor target: Operational requirements and material-design interface”. In: *Nuclear Materials and Energy* 9 (2016), pp. 171 –176.

[33] Flavio Dobran. “Fusion energy conversion in magnetically confined plasma reactors”. In: *Progress in Nuclear Energy* 60 (2012), pp. 89 –116.

[34] “Numerical studies on helium cooled divertor finger mock up with sectorial extended surfaces”. In: *Fusion Engineering and Design* 89.11 (2014), pp. 2647 –2658.

[35] Phani Domalapally and Slavomir Entler. “Comparison of schemes for cooling high heat flux components in fusion reactors”. In: *Acta Polytechnica* 55 (Apr. 2015).

[36] JH Rosenfeld et al. “Cooling of plasma facing components using helium-cooled porous metal heat exchangers”. In: *Fusion technology* 1 (1994), pp. 255–258.

[37] C.P.C Wong et al. “Helium-cooled refractory alloys first wall and blanket evaluation”. In: *Fusion Engineering and Design* 49-50 (2000), pp. 709 –717.

[38] D.L. Youchison et al. “High heat flux testing of a helium-cooled tungsten tube with porous foam”. In: *Fusion Engineering and Design* 82.15 (2007). Proceedings of the 24th Symposium on Fusion Technology, pp. 1854 –1860.

[39] Dennis L Youchison et al. “Thermal performance and flow instabilities in a multi-channel, helium-cooled, porous metal divertor module”. In: *Fusion Engineering and Design* 49-50 (2000), pp. 407 –415.

[40] J.E. Pulsifer and A.R. Raffray. “Structured porous media for high heat flux fusion applications”. In: Feb. 2002, pp. 352 –355.

[41] C.B. Baxi and C.P.C. Wong. “Review of helium cooling for fusion reactor applications”. In: *Fusion Engineering and Design* 51-52 (2000), pp. 319 –324.

[42] E. Diegele et al. “Modular He-cooled divertor for power plant application”. In: *Fusion Engineering and Design - FUSION ENG DES* 66 (Sept. 2003), pp. 383–387.

[43] Colin Glynn et al. “Jet Impingement Cooling”. In: *Proceedings of the 9th UK National Heat Transfer Conference* (Jan. 2005).

[44] Luai Al-Hadhrami et al. “Jet Impingement Cooling in Gas Turbines for Improving Thermal Efficiency and Power Density”. In: Nov. 2011.

[45] Prachai Norajitra et al. “Status of development of the EU He-cooled divertor for DEMO”. In: (Jan. 2008).

[46] A.R. Raffray et al. “Optimizing the overall configuration of a He-cooled W-alloy divertor for a power plant”. In: *Fusion Engineering and Design* 84.7 (2009). Proceeding of the 25th Symposium on Fusion Technology, pp. 1553 –1557.

[47] Ph Chappuis et al. “Possible divertor solutions for a fusion reactor.: Part 2. Technical aspects of a possible divertor”. In: *Fusion Engineering and Design* 36.1 (1997), pp. 109 –117.

[48] Zinovy Gorbis et al. “High-heat-flux removal by phase-change fluid and particulate flow”. In: *Fusion Technology - FUSION TECHNOL* 23 (July 1993), pp. 435–441.

[49] J.H. Rosenfeld et al. “ADVANCES IN POROUS MEDIA HEAT EXCHANGERS FOR FUSION APPLICATIONS”. In: *Fusion Technology 1996*. Ed. by C. VARANDAS and F. SERRA. Oxford: Elsevier, 1997, pp. 487 –490.

[50] Satoshi Suzuki et al. “Development of the plasma facing components in Japan for ITER”. In: *Fusion Engineering and Design* 87.5 (2012). Tenth International Symposium on Fusion Nuclear Technology (ISFNT-10), pp. 845 –852.

[51] Zhongwei Wang et al. “Design of the hypervapotron module for the EAST device”. In: *Fusion Engineering and Design* 87.5 (2012). Tenth International Symposium on Fusion Nuclear Technology (ISFNT-10), pp. 868 –871.

[52] K. Ezato et al. “Critical heat flux testing on screw cooling tube made of RAFM-steel F82H for divertor application”. In: *Fusion Engineering and Design* 75-79 (2005). Proceedings of the 23rd Symposium of Fusion Technology, pp. 313 –318.

[53] A Inoue et al. “Studies on a cooling of high heat flux surface in fusion reactor by impinging planar jet flow”. In: *Fusion Engineering and Design* 51-52 (2000), pp. 781 –787.

[54] Jack Robert Nicholas et al. “Development of a high-heat flux cooling element with potential application in a near-term fusion power plant divertor”. In: *Fusion Engineering and Design* 96-97 (2015). Proceedings of the 28th Symposium On Fusion Technology (SOFT-28), pp. 136 –141.

[55] J. R. Nicholas et al. “Manufacture and Initial Thermo-Fluid Measurements on a Heat Sink Module for Potential Applications in a DEMO”. In: *Fusion Science and Technology* 72.4 (2017), pp. 566–573.

[56] Jack Nicholas. “Heat Transfer for Fusion Power Plant Divertors”. PhD thesis. University of Oxford, 2017.

[57] Francisco L Tabarés et al. “Reactor divertor designs based on liquid metal concepts”. In: *Eurofusion WPDTT2-PR (16)* 15478 (2016), p. 28.

[58] V A Evtikhin et al. “Lithium divertor concept and results of supporting experiments”. In: *Plasma Physics and Controlled Fusion* 44.6 (May 2002), pp. 955–977.

[59] D.N. Ruzic et al. “Lithium–metal infused trenches (LiMIT) for heat removal in fusion devices”. In: *Nuclear Fusion* 51.10 (Aug. 2011), p. 102002.

[60] *Laser Lenses, Optics, and Focus*. Laser Gods. URL: https://lasergods.com/laser-lenses-optics-and-focus/ (visited on 03/14/2020).

[61] *Technical Note: Focusing and Collimating*. MKS Instruments. URL: https://www.newport.com/n/focusing-and-collimating (visited on 03/14/2020).

[62] J. Chaves. *Introduction to Nonimaging Optics*. Optical Science and Engineering. CRC Press, 2008.

[63] Andrea Antonini et al. “Modelling of Compound Parabolic Concentrators for Photovoltaic Applications”. In: *International Journal of Optics and Applications* Vol 3 (Aug. 2013), In press.

[64] Damasen Ikwaba Paul. “Application of compound parabolic concentrators to solar photovoltaic conversion: A comprehensive review”. In: *International Journal of Energy Research* 43.9 (2019), pp. 4003–4050.

[65] Soteris A. Kalogirou. “Chapter 3 - Solar Energy Collectors”. In: *Solar Energy Engineering (Second Edition)*. Ed. by Soteris A. Kalogirou. Second Edition. Boston: Academic Press, 2014, pp. 125 –220.

[66] Akio Suzuki and Shigeo Kobayashi. “Absorber design for a compound parabolic concentrator collector without transmission loss”. In: *Appl. Opt.* 33.28 (Oct. 1994), pp. 6578–6581.

[67] Chigbo Mgbemene et al. “Electricity Generation From a Compound Parabolic Concentrator Coupled to a Thermoelectric Module”. In: *Journal of Solar Energy Engineering-transactions of The Asme - J SOL ENERGY ENG* 132 (Aug. 2010).

[68] Sunita Darbe. “Optics for High-Efficiency Full Spectrum Photovoltaics”. PhD thesis. California Institute of Technology, 2017.

[69] *3.4 Surface Scattering*. Japan Association of Remote Sensing. URL: http://wtlab.iis.u-tokyo.ac.jp/wataru/lecture/rsgis/rsnote/cp3/cp3-4.htm (visited on 03/14/2020).

[70] Inductiveload. *Lambert Cosine Law 1*. Wikimedia Commons. URL: https://commons.wikimedia.org/wiki/File:Lambert_Cosine_Law_1.svg (visited on 03/14/2020).

[71] *Reflectivity: More Complicated Than It Seems*. Edmund Optics. URL: https://www.edmundoptics.co.uk/knowledge-center/trending-in-optics/high-reflectivity-mirrors/ (visited on 03/14/2020).

[72] Hiroyuki Tan et al. “A new approach to measure the volume scattering function”. In: *Opt. Express* 21.16 (Aug. 2013), pp. 18697–18711.

[73] Thomas Cooper et al. “Performance of compound parabolic concentrators with polygonal apertures”. In: *Solar Energy* 95 (2013), pp. 308 –318.

[74] Narkis Shatz and John Bortz. “Inverse engineering perspective on nonimaging optical design”. In: *Proc. SPIE* 2538 (Aug. 1995).

[75] Antonio Parretta and Mario Tucci. “MODELS OF LIGHT COLLECTION OF 3D-CPC CONCENTRATORS UNDER COLLIMATED BEAMS”. In: Sept. 2014.

[76] Ari Rabl. “Optical and thermal properties of compound parabolic concentrators”. In: *Solar Energy* 18.6 (1976), pp. 497 –511.

[77] *Application note: Intensity Patterns of PPM412 Type VCSEL Laser Modules*. Philips.

[78] *Surface Roughness in Manufacturing*. ISO Finishing. URL: https://isofinishing.com/surface-roughness-chart-2/ (visited on 07/08/2020).

[79] *Surface Finish Charts*. L.J. Star Inc. URL: https://www.ljstar.com/resources/surface-finish-charts/ (visited on 07/08/2020).

[80] *Conversation with Light Tec Technical Support*. Light Tec, 2020.

[81] M. Kauffman and R. Neu. “Tungsten as first wall material in fusion devices”. In: *Fusion Engineering and Design* 82 (2007), pp. 521–527.

[82] Chai Ren et al. “Methods for improving ductility of tungsten - A review”. In: *International Journal of Refractory Metals and Hard Materials* 75 (2018), pp. 170 –183.

[83] *Structural Design Criteria for In-vessel Components (SDC-IC)*. Tech. rep.

[84] M Richou et al. “Development of a graded W/CuCrZr divertor for DEMO reactor”. In: 2016.

[85] Jeong-Ha You. “A review on two previous divertor target concepts for DEMO: Mutual impact between structural design requirements and materials performance”. In: *Nuclear Fusion* 55 (Sept. 2015), p. 113026.

[86] *Application Notes: Optical Modes in VCSELs*. Tech. rep.

[87] A. Börzsönyi et al. “Dispersion measurement of inert gases and gas mixtures at 800 nm”. In: *Appl. Opt.* 47.27 (Sept. 2008), pp. 4856–4863.

[88] *Description of Outgassing Data Report*. NASA. URL: https://outgassing.nasa.gov/og_desc.html (visited on 07/17/2020).

[89] *ASTM E595 - 15: Standard Test Method for Total Mass Loss and Collected Volatile Condensable Materials from Outgassing in a Vacuum Environment*. ASTM. URL: https://www.astm.org/Standards/E595.htm (visited on 07/17/2020).

[90] *Vantablack S-VIS Automotive Datasheet*. Surrey Nanosystems.

[91] *Acktar Black: World's Blackest Coatings*. Acktar Advanced Coatings. URL: https://www.acktar.com/wp-content/uploads/2017/10/Acktar_brochure.pdf (visited on 07/17/2020).

[92] *Singularity Black*. NanoLab. URL: https://www.nano-lab.com/optical-black-coatings.html (visited on 07/17/2020).

[93] Ruediger Brandt et al. "Emissivity reference paints for high temperature applications". In: *Measurement* 41.7 (2008), pp. 731 –736.

[94] *HIGH TEMPERATURE HIGH EMISSIVITY COATINGS, Technical Bulletin A5-S2*. Aremco. URL: https://www.aremco.com/wp-content/uploads/2018/05/A05_S2_18_Emissivity.pdf (visited on 07/17/2020).

[95] Manuel A. Quijada et al. "Hemispherical reflectance and emittance properties of carbon nanotubes coatings at infrared wavelengths". In: *Cryogenic Optical Systems and Instruments XIII*. Ed. by James B. Heaney and E. Todd Kvamme. Vol. 8150. International Society for Optics and Photonics. SPIE, 2011, pp. 11 –21.

[96] Eric Pop et al. "Thermal properties of graphene: Fundamentals and applications". In: *MRS Bulletin* 37.12 (Nov. 2012), 1273–1281.

[97] *Conversation with Trumpf Technical Support*. The TRUMPF Group, 2020.

[98] *THERMAL EMISSIVITY AND RADIATIVE HEAT TRANSFER*. Tech. rep. June 2018.

[99] *Table of Emissivity of Various Surfaces*. Mikron Instrument Company, Inc. URL: http://www-eng.lbl.gov/~dw/projects/DW4229_LHC_detector_analysis/calculations/emissivity2.pdf (visited on 07/02/2020).

[100] Seizi Sasaki et al. "Total hemispherical emissivity of glass sheets with different thicknesses measured by a transient calorimetric technique". In: *High Temperatures-high Pressures - HIGH TEMP-HIGH PRESS* 35-6 (Jan. 2003), pp. 303–312.

[101] *Convective Heat Transfer*. The Engineering Toolbox. URL: https://www.engineeringtoolbox.com/convective-heat-transfer-d_430.html (visited on 03/14/2020).

[102] *Estimating heat transfer coefficients*. Altasim Technologies. URL: https://www.altasimtechnologies.com/electronic-cooling/estimating-heat-transfer-coefficients/ (visited on 03/14/2020).

[103] *Full Materials Data Listing*. Granta Design. 2020. URL: https://grantadesign.com/industry/products/data/full-materials-data-listings/ (visited on 07/02/2020).

[104] Micheal W. Glass. "CHAPARRAL: A library for solving large enclosure radiation heat transfer problems". In: 1995.

[105] Michael F. Cohen and Donald P. Greenberg. "The hemi-cube: a radiosity solution for complex environments". In: *SIGGRAPH '85*. 1985.

[106] J.H. You et al. “European divertor target concepts for DEMO: Design rationales and high heat flux performance”. In: *Nuclear Materials and Energy* 16 (2018), pp. 1 –11.

[107] B Bayanov et al. “Neutron producing target for accelerator based neutron capture therapy”. In: *Journal of Physics: Conference Series* 41 (May 2006), pp. 460–465.

[108] S. D. Marshall et al. “Heat exchanger improvement via curved, angular and wavy microfluidic channels: A comparison of numerical and experimental results”. In: *2017 16th IEEE Intersociety Conference on Thermal and Thermomechanical Phenomena in Electronic Systems (ITherm)*. 2017, pp. 585–592.

[109] Yan Liu et al. “The Flow and Heat Transfer Characteristic of Curved Channel CPU Water-Cooled Heat Sinks”. In: *Applied Mechanics and Materials* 391 (Sept. 2013), pp. 213–216.

[110] Avijit Bhunia and C. L. Chen. “Thermal Characteristics in a Curved Rectangular Channel With Variable Cross-Sectional Area”. In: *Journal of Heat Transfer* 133.12 (Oct. 2011). 121901. eprint: https://asmedigitalcollection.asme.org/heattransfer/article-pdf/133/12/121901/5499304/121901_1.pdf.

[111] *Evaluation of Heat Transfer Performance of a Spiral Microfluidic Heatsink and Heat Exchanger Device*. Vol. ASME 2018 16th International Conference on Nanochannels, Microchannels, and Minichannels. International Conference on Nanochannels, Microchannels, and Minichannels. V001T07A002. June 2018. eprint: https://asmedigitalcollection.asme.org/ICNMM/proceedings-pdf/ICNMM2018/51197/V001T07A002/2792162/v001t07a002-icnmm2018-7804.pdf.

[112] Ihsan Ali Ghani et al. “Hydrothermal performance of microchannel heat sink: The effect of channel design”. In: *International Journal of Heat and Mass Transfer* 107 (2017), pp. 21 –44.

[113] W.R. Dean M.A. “XVI. Note on the motion of fluid in a curved pipe”. In: *The London, Edinburgh, and Dublin Philosophical Magazine and Journal of Science* 4.20 (1927), pp. 208–223. eprint: https://doi.org/10.1080/14786440708564324.

[114] W.R. Dean M.A. “LXXII. The stream-line motion of fluid in a curved pipe (Second paper)”. In: *The London, Edinburgh, and Dublin Philosophical Magazine and Journal of Science* 5.30 (1928), pp. 673–695. eprint: https://doi.org/10.1080/14786440408564513.

[115] R.L. Webb. *Principles of enhanced heat transfer*. Wiley-Interscience publication. John Wiley & Sons, 1994.

[116] Boussinesq. “Mémoire sur l’influence des frottements dans les mouvements réguliers des fluides.” fre. In: *Journal de Mathématiques Pures et Appliquées* (1868), pp. 377–424.

[117] G. I. Taylor. "The Criterion for Turbulence in Curved Pipes". In: *Proceedings of the Royal Society of London. Series A, Containing Papers of a Mathematical and Physical Character* 124.794 (1929), pp. 243–249.

[118] C. M. White and Edward Victor Appleton. "Streamline flow through curved pipes". In: *Proceedings of the Royal Society of London. Series A, Containing Papers of a Mathematical and Physical Character* 123.792 (1929), pp. 645–663. eprint: https://royalsocietypublishing.org/doi/pdf/10.1098/rspa.1929.0089.

[119] Athanasia Kalpakli Vester et al. "Turbulent Flows in Curved Pipes: Recent Advances in Experiments and Simulations". In: *Applied Mechanics Reviews* 68.5 (Sept. 2016). 050802. eprint: https://asmedigitalcollection.asme.org/appliedmechanicsreviews/article-pdf/68/5/050802/6075086/amr_068_05_050802.pdf.

[120] *Dean Flow*. Filtration Solutions, Inc. URL: https://www.filtsol.com/copy-of-hollow-fiber-membranes (visited on 07/06/2020).

[121] Mehdi Ghobadi and Yuri Stephan Muzychka. "A Review of Heat Transfer and Pressure Drop Correlations for Laminar Flow in Curved Circular Ducts". In: *Heat Transfer Engineering* 37.10 (2016), pp. 815–839. eprint: https://doi.org/10.1080/01457632.2015.1089735.

[122] F. Rütten et al. "Large-eddy simulation of low frequency oscillations of the Dean vortices in turbulent pipe bend flows". In: *Physics of Fluids* 17.3 (2005), p. 035107. eprint: https://doi.org/10.1063/1.1852573.

[123] Hiroyuki Takamura et al. "Flow Visualization and Frequency Characteristics of Velocity Fluctuations of Complex Turbulent Flow in a Short Elbow Piping Under High Reynolds Number Condition". In: *Journal of Fluids Engineering* 134 (Oct. 2012), p. 101201.

[124] A. Kalpakli et al. "Vortical patterns in turbulent flow downstream a 90 degrees curved pipe at high Womersley numbers". In: *International Journal of Heat and Fluid Flow* 44 (Dec. 2013).

[125] Mehdi Ghobadi and Y. Muzychka. "Heat Transfer in Spiral Channel Heat Sinks". In: vol. 1. Jan. 2011.

[126] Youmin Xi et al. "Single-phase flow and heat transfer in swirl microchannels". In: *Experimental Thermal and Fluid Science* 34.8 (2010), pp. 1309 –1315.

[127] P. Minton. "Designing spiral plate heat exchangers". In: *Chemical Engineering (Rughy, U.K.)* 77 (1970), pp. 103–112.

[128] Geun-jong Yoo et al. "Fluid flow and heat transfer characteristics of spiral coiled tube: Effects of Reynolds number and curvature ratio". In: *J. Cent. South Univ* 19 (Feb. 2012), pp. 471–476.

[129] Michael W. Egner and Louis C. Burmeister. "Heat transfer for laminar flow in spiral ducts of rectangular cross section". In: 2005.

[130] H. Kharvani et al. “An experimental investigation of heat transfer in a spiral-coil tube with pulsating turbulent water flow”. In: *Heat and Mass Transfer* 52 (Oct. 2015).

[131] Paisarn Naphon and Jamnean Suwagrai. “Effect of curvature ratios on the heat transfer and flow developments in the horizontal spirally coiled tubes”. In: *International Journal of Heat and Mass Transfer* 50.3 (2007), pp. 444 –451.

[132] Kanchan Chowdhury et al. “Analytical studies on the temperature distribution in spiral plate heat exchangers: Straightforward design formulae for efficiency and mean temperature difference”. In: *Chemical Engineering and Processing: Process Intensification* 19.4 (1985), pp. 183 –190.

[133] Jamshid Khorshidi and Salman Heidari. “Design and Construction of a Spiral Heat Exchanger”. In: *Advances in Chemical Engineering and Science* 06 (Jan. 2016), pp. 201–208.

[134] Louis C. Burmeister. “Effectiveness of a Spiral-Plate Heat Exchanger With Equal Capacitance Rates”. In: *Journal of Heat Transfer* 128.3 (Aug. 2005), pp. 295–301. eprint: https://asmedigitalcollection.asme.org/heattransfer/article-pdf/128/3/295/5665042/295_1.pdf.

[135] *Thermophysical Properties of Fluid Systems*. National Institute of Standards and Technology. URL: https://webbook.nist.gov/chemistry/fluid/ (visited on 04/27/2020).

[136] B.N. Singh et al. *Final report on in-reactor creep-fatigue deformation behaviour of a CuCrZr alloy: COFAT 1*. English. Riso-R R-1571(EN). Project code: 16166. 2007.

[137] B. Bazylev and R. Fetzer. *The quantification of the key physics parameters for the DEMO fusion power reactor and analysis of the reactor relevant physics issues (KIT Scientific Reports ; 7661)*. Tech. rep. 31.03.02; LK 01. Karlsruher Institut für Technologie (KIT), 2014. 129 pp.

[138] Muyuan Li and Jeong-Ha You. “Structural impact of creep in tungsten monoblock divertor target at 20 MW/m2”. In: *Nuclear Materials and Energy* 14 (2018), pp. 1 –7.

[139] E. Abbena et al. *Modern Differential Geometry of Curves and Surfaces with Mathematica, Third Edition*. Textbooks in Mathematics. Taylor & Francis, 2006.

[140] Andrea Cioncolini and Lorenzo Santini. “An experimental investigation regarding the laminar to turbulent flow transition in helically coiled pipes”. In: *Experimental Thermal and Fluid Science* 30.4 (2006), pp. 367 –380.

[141] *ESDU, Pressure Losses in Curved Ducts: Coils*. Tech. rep. 77092. London, 1977.

[142] Volker Gnielinski. “Neue Gleichungen für den Wärme- und den Stoffübergang in turbulent durchströmten Rohren und Kanälen”. In: *Forschung im Ingenieurwesen A* 41 (1975), pp. 8–16.

[143] R.A. Seban and E.F. McLaughlin. “Heat transfer in tube coils with laminar and turbulent flow”. In: *International Journal of Heat and Mass Transfer* 6.5 (1963), pp. 387 –395.

[144] Yasuo Mori and Wataru Nakayama. “Study of forced convective heat transfer in curved pipes (2nd report, turbulent region)”. In: *International Journal of Heat and Mass Transfer* 10.1 (1967), pp. 37 –59.

[145] *Ansys® CFX*, Release 19.2, Help System, CFX-Modeling Solver Guide, Ansys, Inc.

[146] David Apsley. *Friction Laws*. University of Manchester. 2009. URL: https://personalpages.manchester.ac.uk/staff/david.d.apsley/lectures/turbbl/friction.pdf (visited on 03/14/2020).

[147] S.A.W. van den Broek. “Towards flameless combustion in gas turbine engines”. In: 2017.

[148] *Eddy Viscosity*. American Meteorological Society. URL: http://glossary.ametsoc.org/wiki/Eddy_viscosity (visited on 05/28/2020).

[149] *Two Equation Turbulence Models*. CFD-Online. URL: https://www.cfd-online.com/Wiki/Two_equation_models (visited on 05/28/2020).

[150] *Ansys® Fluent*, Release 12.0, Help System, Fluent User Guide, Ansys, Inc.

[151] *Ansys® ICEM*, Release 17.0, ANSYS ICEM CFD Help Manual, Ansys, Inc.

[152] P Norajitra et al. “European development of He-cooled divertors for fusion power plants”. In: *Nuclear Fusion* 45.11 (Oct. 2005), pp. 1271–1276.

[153] Aldo Pizzuto et al. “HETS performances in He cooled power plant divertor”. In: *Fusion Engineering and Design* 75-79 (2005). Proceedings of the 23rd Symposium of Fusion Technology, pp. 481 –484.

[154] S. Abdel-Khalik et al. “Thermal-hydraulic studies in support of the ARIES-CS T-tube divertor design”. In: *Fusion Science and Technology* 54 (Oct. 2008).

[155] E. Visca et al. “Assessment of an ITER-like water-cooled divertor for DEMO”. In: *2013 IEEE 25th Symposium on Fusion Engineering (SOFE)*. 2013, pp. 1–6.